

Department of Materials Science and Engineering

**Three dimensional Morphology and Substructure of
Butterfly Martensite**

Robert G. J. Bobbink

Supervisor : Prof. dr. Maria Santofimia Navarro

Specialisation : Metals Science and Technology

Type of report : Master Thesis

Date : September 6, 2024

Three Dimensional Morphology and Substructure of Butterfly Martensite

by

Robert G. J. Bobbink

to obtain the degree of Master of Science
at the Delft University of Technology,
to be defended publicly on Tuesday September 24, 2024 at 1:00 PM.

Student number: 5181690
Project duration: January 4, 2024 – September 24, 2024
Thesis committee: Prof. dr. Maria Santofimia Navarro, TU Delft, supervisor
Prof. dr. ir. L. A. I. Kestens, UGent, TU Delft
Dr. H. Farahani, Tata Steel
Ing. C. Kwakernaak, TU Delft

Cover: Canadarm 2 Robotic Arm Grapples SpaceX Dragon by NASA
under CC BY-NC 2.0 (Modified)
Style: TU Delft Report Style, with modifications by Daan Zwaneveld

An electronic version of this thesis is available at <http://repository.tudelft.nl/>.

Acknowledgement

I express my deep gratitude to my esteemed supervisor, Prof. Dr. Maria Santofimia Navarro (TU Delft), for her steadfast guidance, patience, and wealth of knowledge and expertise throughout this undertaking. Additionally, I am sincerely thankful to Prof. dr. ir. Leo Kestens, Dr. Hussein Farahani and ing. Kees Kwakernaak for generously agreeing to serve on the defence committee.

I also extend my heartfelt appreciation to all the laboratory technicians whose assistance was indispensable during my experimental work. In particular, I wish to acknowledge Richard Huizenga for his contributions to XRD analysis and his support with the ThermoCalc software, Kees Kwakernaak for his expertise in (3D-)EBSD measurements, Nico Geerlofs for his invaluable support with the dilatometry experiments, and Durga Mainaly for his assistance with optical microscopy and sample preparation.

Last, but not least, I would like to express my gratitude to Konstantina Traka as without her knowledge and expertise in the field of computational materials science, the characteristic butterfly planes could not have been determined.

Abstract

This thesis aims to investigate both the two-dimensional and three-dimensional (sub)structure of the butterfly martensite (α'_{BF}) morphology. In order to do this, multiple different types of heat treatments were applied to a Fe-25Ni alloy to find the optimal morphology consisting of a low density of α'_{BF} that is surrounded by austenite(γ).

Two dimensional analyses were performed by applying a combination of optical microscopy, scanning electron microscopy and Electron Backscatter Diffraction (EBSD). The α'_{BF} morphology was found to nucleate and grow as the first martensite (α') morphology just below the martensite start temperature (M_s) within this 25Ni alloy. A decrease in austenisation time resulted in smaller γ grain sizes. This reduction in γ grain size resulted in a reduction of the M_s of the alloy which in its turn reduced the amount of undercooling applied to the material below M_s upon quenching towards room temperature, causing a decrease in the freshly formed α' fraction. Upon observation of the freshly formed α' it was found that the α'_{BF} seemed to prefer formation near the centre of γ grains instead of near γ grain boundaries. When α'_{BF} was formed near a γ grain boundaries, one wing tends to aligned itself with this boundary. Through trace analysis, it was found that the habit planes of α'_{BF} were close to $\{557\}_{\gamma}$, $\{225\}_{\gamma}$ and $\{3\ 10\ 15\}_{\gamma}$, which are characteristic habit planes of lath, butterfly and lenticular α' , respectively. The orientation relationship (OR) between the γ and α'_{BF} is found be a combination of both the Greninger-Troiano (G-T) and Nishiyama-Wasserman (N-W) OR.

Three dimensional analysis was performed using both serial sectioning and 3D-EBSD. Serial sectioning showed that α'_{BF} within this alloy was sensitive to formation upon mechanical polishing. 3D-EBSD gave insight on the three-dimensional morphology and substructure of the α'_{BF} grains. It was observed that the junction plane could be non-continuous. Moreover, it is shown that the apparent wing angle greatly depends on the angle that the α'_{BF} grain makes perpendicular to the sample surface and that the tail of the the α'_{BF} grain can run along the entire length of the grain.

Contents

1	Introduction	1
2	Background	2
2.1	Martensite crystallography	2
2.1.1	Habit plane	4
2.1.2	Orientation relations	5
2.2	Formation temperature and chemical composition	6
2.3	3D and 2D structures	6
2.4	2D substructures	8
2.5	Formation and growth	9
2.6	Catalytic formation	10
2.7	Wing angle	11
2.8	Effect of prior austenite grain size (PAGS)	12
2.9	Formed upon mechanical polishing	12
2.10	EBSD	13
2.10.1	Kikuchi patterns	13
2.10.2	Orientation maps	14
2.10.3	(inverse) pole figures	14
3	Materials and methods	16
3.1	Material and specimen preparation	16
3.2	Heat treatment	16
3.3	Microstructure characterisation	18
3.3.1	Sample preparation for light optical microscopy (LOM) and SEM/EBSD	18
3.3.2	LOM	19
3.3.3	SEM and EBSD	19
3.3.4	Serial sectioning	19
3.3.5	3D-EBSD	19
3.3.6	DREAM3D-NX: 3D reconstruction, cleanup and filtering	20
4	Results and Discussion	22
4.1	Investigation of the as-received material	22
4.2	Oven and liquid nitrogen quenching experiments	23
4.3	Analysis of dilatometry and microstructure	24
4.4	2D analysis of butterfly martensite	27
4.4.1	Morphologies & formation temperature	27
4.4.2	Butterfly morphology	29
4.4.3	Butterfly substructures	30
4.4.4	Formation sites	31
4.4.5	Catalytic formation	32
4.4.6	Butterfly martensite grain orientations	33
4.4.7	Orientation relationships	34
4.4.8	Butterfly martensite growth	35
4.5	3D analysis of butterfly martensite	36
4.5.1	Serial sectioning	36
4.5.2	3D EBSD	37
5	Conclusion	41
6	Recommendations	42
A	CCT diagram 25Ni	47
B	Phase diagram 25Ni	48
C	Austenite grain sizes at various t_A	49

D	Observing the martensite start temperature through dilatometry	55
E	Martensite fractions	56
F	Python code calculating plane angles by ChatGPT	59
G	3D butterfly grains	61

List of Figures

1	Martensite morphology features [1]	1
2	α' bct lattice, showing C atoms within the octahedral interstitial positions [2].	2
3	Fcc to bct lattice transformation showing Fe atoms (black) together with the carbon atoms (grey) [3]	2
4	(a) Bain correspondence (b) bct unit cell from the austenite phase (c) martensite with true c/a ratio after Bain strain [2].	3
5	Phenomenological theory of martensite crystallography: (a) the austenite lattice (b) structure with the correct shape and wrong structure after \mathbf{P}_1 (c) martensitic lattice with the wrong shape after $\mathbf{P}_1\mathbf{P}_2=\mathbf{RB}$ (bottom) final martensite with the correct structure and macroscopic shape [2].	4
6	Schematic representation of the habit plane [4]	5
7	Distribution map of orientation relationships along the γ/α' interface together with the outcome of trace analysis to determine the habit plane of the γ/α' interface . [1]	5
8	The morphologies of martensite that can form in Fe-Ni-C and Fe-Cr-C alloys as a functions of temperature and alloying content. [5]	6
9	(a) A three dimensional representation of the butterfly martensite grain [6], (b) two dimensional butterfly morphologies acquired from slicing the three dimensional grain along the longitudinal direction at sections A, B and C.	7
10	Schematic representation of the substructures that are found within butterfly martensite [7]	8
11	(a) Schematic representation of the formation of butterfly with tails [6], (b) Schematic representation of the formation of butterfly without tails [6]	9
12	(a) Butterfly grain nucleation along the austenite grain boundary, (b) lath martensite nucleation at the austenite grain boundary and growing parallel to the first formed butterfly grain, (c) complete transformation of the prior austenite grain to lath martensite together with some small butterfly grains. [8]	10
13	Isostress lines of $\tau_{\bar{1}10}(111)$ [9]	11
14	(a) Butterfly martensite grains formed at the convexity of first formed butterfly grains, (b) Butterfly martensite grains formed at the concavity of first formed butterfly grains. [9]	11
15	Electron micrograph of strain-induced butterfly martensite formed through mechanical polishing of the surface at room temperature. [10]	12
16	Figure 16 generation depth of back-scattered diffracted electrons [11]	13
17	Kikuchi patten acquired by EBSD [12]	13
18	Schematic representation of the scattering of an incoming electron beam which satisfies Bragg's diffraction creating Kikuchi bands, made by C. Kwakernaak [13]	13
19	Processing order of obtaining a kikuchi pattern using a Hough transformation [14]	14
20	Pole figure formation [15]	15
21	(a) Pole figure (b) stereographic triangle [15]	15
22	Schematic representation of the thermal treatments used during (a) oven and liquid nitrogen quenching experiments, (b) oven and air cooling experiments and (c) dilatometry experiments	16
23	Graph showing the discrepancy between the applied temperature program (yellow line) and the actual temperature profile within the heating chamber of the oven during the O.AC.TC experiment (blue line)	18
24	(a) Surface of the As-received sample showing the butterfly morphology, (b) Pt layer applied over a single α'_{BF} grain which is selected for FIB-3D-EBSD, (c) FIB-Milling of trenches around the selected α'_{BF} grain leaving a small bridge attached for stability, (d) undercutting the selected volume at 45° in order to remove the volume after cutting the bridge, (e) attaching a micromanipulator to the volume and removing the bridge and (f) removal of the volume	20
25	The (visual) filters that are applied in order to observe a single α'_{BF} grain. (a) original volume, (b) volume after slice alignment and noise filtering, (c) removal of the γ phase, (d) cropping of the volume to single out a single α'_{BF} grain, (e) filtering out the remaining surrounding α' through among others IPF colour and FeatureIds, (f) list of filters applied within Dream3D-NX in order to obtain a 3D image of a butterfly grain	21
26	Cross section view of the dilatometry sample of the as-received material obtained by LOM	22

27	(a) SEM image of sample O_N300s showing both the butterfly and lenticular martensite morphologies ,(b) Optical microscopy image of sample O_NAC_N1 showing a microstructure comprised of austenite and butterfly martensite	23
28	(a) Full dilatometry curves of specimens held for varying durations (1, 4, 6, 8, 10, and 12 hours), (b) length change rate upon heating	24
29	(a) LOM image of the surface of an As-received specimen heated up to 898 K (before Region 2) and cooled down to RT, (b) LOM image of the surface of an As-received specimen heated up to 1123 K (after Region 2) and cooled down to RT	25
30	Graph showing the relation between PAGES and M_s	26
31	Graph showing the increase in γ grain size, M_s and α' fraction formed upon quenching as a function of the t_A	26
32	(a) Graph showing the relation between the degree of undercooling below M_s and the amount of α' that is formed upon cooling, (b) a graph showing the fraction of newly transformed α' as the temperature is decreased [16]	27
33	(a) Lath martensite forming near the edges of the D_10hAus sample , (b) small lenticular α' plates surrounding large α'_{BF} grains formed within the O_N200s sample	28
34	Order of α' morphology formation based on their formation temperature within the 25Ni alloy, based on image 1 by Sato et al. [1]	28
35	LOM image of the O_AC.1 sample showing three different two-dimensional α' subtypes	29
36	SEM images of the D_8hAus sample showing (a) Habit plane trace analysis of a large α_{BF} grain with a midrib structure in its left wing, (b) Habit plane trace analysis of a small and thin α_{BF} grain	30
37	Schematic representation of a grain boundary trace at the surface of a sample in between two crystals and the angle that this boundary plane can have below the surface (angle β). [17]	31
38	SEM image quality map of the D_8hAus sample	32
39	Butterfly grains that has aligned with the γ grain boundary of the D_8hAus sample, resulting in an irregular shape	32
40	LOM image of the O_AC.1 sample showing catalytic α'_{BF} formation	32
41	IPF map of the D_8hAus sample parallel to [001] or the direction normal to the sample surface (ND)	33
42	OR maps of the As-received sample where (a) and (b) show the various ORs that are present at the γ/α' interfaces	34
43	Local orientation deviation map of a large α'_{BF} within the D_8hAus sample	35
44	Images of serial sectioning of the As-received sample showing (a) SEM image of the initial surface before serial sectioning, (b)-(e) IPF maps of the surface after removal of approximately 1-3 μ m with respect to the previous section.	36
45	(a) Three dimensional IPF surface image of the entire 3D-EBSD volume showing the α'_{BF}^1 found at the surface of the original sample going in and out of the sample at an angle of 45°, (b)-(e) the α'_{BF}^1 grain with the γ removed at various angles.	38
46	Three dimensional view of the boundary cells, of the α'_{BF}^1 grain within the volume, between the γ and α' as well as boundaries within the α'_{BF}^1 grain itself.	38
47	A slice taken of the α'_{BF}^1 grain at 45° in such a way that the slice is perpendicular to the opening axis.	38
48	Images (a)-(d) showing the three dimensional morphology of the α'_{BF}^2 grain at various angles.	39
49	Two dimensional slices of the α'_{BF}^2 grain together with their dimensions taken at (a) $z=0$ μ m, (b) $z=3.5$ μ m, (c) $z=7.5$ μ m and (d) $z=8.1$ μ m	40
50	Three dimensional figures the α' phase showing: (a) α'_{BF}^2 , which has been given the number 1 surrounded by two other α' grains named 2, which is also α'_{BF} and 3, (b) the same volume without the α'_{BF}^2 grain and (c) a top view of all three α' grains	40
51	(a) A front view of the boundary cells of α'_{BF}^2 and (b) a top view of the boundary cell within α'_{BF}^2	40

List of Tables

1	Orientation relationships during martensitic transformation	5
---	---	---

2	2D butterfly martensite sub-types and their morphology/substructure according to Umemoto et al. [10]	7
3	2D butterfly martensite sub-types and their morphology/substructure according to Gong et al. [6, 18]	7
4	Chemical composition 25Ni alloy	16
5	Samples and heat treatment	17
6	Axis-angle pairs corresponding to various γ/α' orientation relationships	19
7	Experimental results showing the average martensite fraction, martensite start temperature, prior austenite grain size and the observed martensite morphologies of the dilatometry specimens	25
8	Results from habit plane trace analysis	30
9	γ and α' crystallographic grain orientations	33
10	Double tailed grain dimensions	38
11	Single tailed grain dimensions	40

2 Background

2.1 Martensite crystallography

The rate at which the α' phase grows is known to approach the speed of sound in steel. A α' crystal can form within 10^{-7} s [19]. These fast growth rates of 10^4 - 10^5 cms^{-1} [20], that are associated with the martensitic transformation, do not allow atoms to diffuse within such a short time-span resulting in a diffusionless transformation. Because of the diffusionless nature of the martensitic transformation, the composition of the transformed α' will be identical of that of the parent γ [2, 21].

During the martensitic transformation, the austenitic parent phase, which has a face-centered cubic (fcc) structure is transformed to a body-centered tetragonal structure (bct). This type of abrupt phase change is referred to as a first order phase transformation. The tetragonality of the martensite is measured as the ratio between lattice parameters c and a as can be seen in Figure 2. This c/a ratio is linearly dependent on the carbon content as denoted in Equation 1 [2, 20, 22].

$$c/a = 1 + (0.046 \pm 0.001) \cdot \text{wt}\%C \quad (1)$$

As can be seen from this equation, at zero carbon content, the α' crystal structure would be bcc as $c/a = 1$ implies a cubic structure.

Figure 2 shows the bct α' lattice. As can be seen, the carbon atoms occupy the 'z' octahedral interstitials. These octahedral interstitial positions are situated between the Fe atoms parallel to $[001]$ (z-axis), this is also known as the third sublattice of octahedral interstitial sites [2, 22]. During the diffusionless $\gamma \rightarrow \alpha'$ transformation, the carbon atoms that are situated within the fcc octahedrals have no time to move. Hence, the carbon atoms will, after the transformation, occupy one of the bcc sublattices, causing the bcc lattice to get expanded in an asymmetrical way that gives rise to the tetragonality that is observed within the martensitic bct lattice as can be observed in Figure 3. α' martensite is often found in ferrous alloys like Fe-C and Fe-Ni.

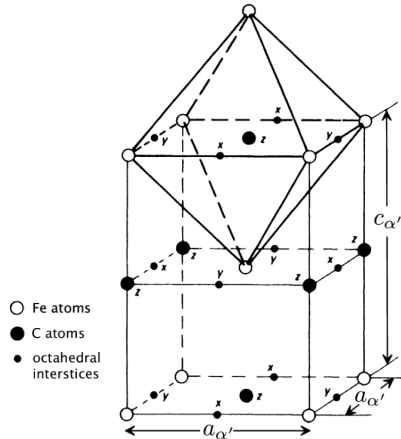


Figure 2: α' bct lattice, showing C atoms within the octahedral interstitial positions [2].

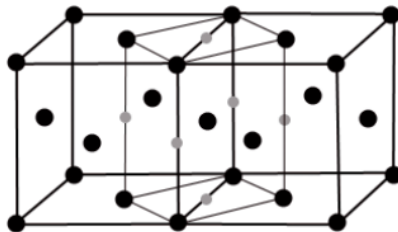


Figure 3: Fcc to bct lattice transformation showing Fe atoms (black) together with the carbon atoms (grey) [3]

In 1924 E.C. Bain proposed a mechanism to be able to accompany the homogeneous deformation of the γ lattice that occurs during the martensitic transformation. Observing Figure 4(a), the following orientation relationships, called the Bain correspondence, are required to obtain the product phase α' from the austenitic parent phase [2, 23–26]:

$$[001]_{\gamma} \parallel [001]_{\alpha'}$$

$$[1\bar{1}0]_{\gamma} \parallel [100]_{\alpha'}$$

$$[110]_{\gamma} \parallel [010]_{\alpha'}$$

As seen in Figures 4(b) and 4(c), to acquire the correct sized α' lattice, the unit cell is contracted about 17% along $[001]_{\alpha'}$ and expanded for about 12% along both $[100]_{\alpha'}$ and $[010]_{\alpha'}$, known as Bain strain [2, 23, 24]. The Bain strain can be written as shown by Equations 2-4:

$$\hat{\varepsilon}_0 = \begin{pmatrix} \varepsilon_0 & 0 & 0 \\ 0 & \varepsilon_0 & 0 \\ 0 & 0 & -\varepsilon'_0 \end{pmatrix} \quad (2)$$

$$\varepsilon_0 = \frac{\sqrt{2}a_{\alpha} - a_{\gamma}}{a_{\gamma}} \quad (3)$$

$$-\varepsilon'_0 = \frac{a_{\alpha} - a_{\gamma}}{a_{\gamma}} \quad (4)$$

Where a_{α} and a_{γ} are the lattice parameters of the fcc and bcc phase, respectively [20].

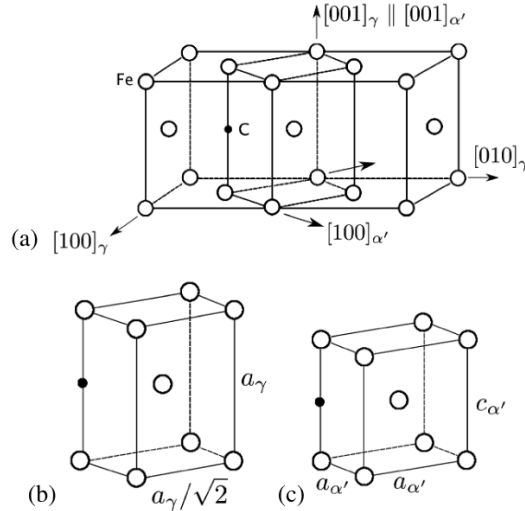


Figure 4: (a) Bain correspondence (b) bct unit cell from the austenite phase (c) martensite with true c/a ratio after Bain strain [2].

The Bain strain (**B**) alone is not sufficient enough to completely deform the lattice. After the Bain strain, no line is left undistorted/unrotated. A high degree of coherency is required resulting in the need of a invariant-line strain (ILS). A rigid body rotation is applied (**R**) such that **RB** will result in an ILS and will thus acquire the correct lattice structure. However, this is still inconsistent with the observed invariant-plane strain (IPS). In 1953, Bowles and Mackenzie [27] proposed the phenomenological theory of martensite crystallography (PTMC). This theory explains how the parent austenite lattice transforms into the final, observed, martensitic lattice and can be seen schematically in Figure 5 .

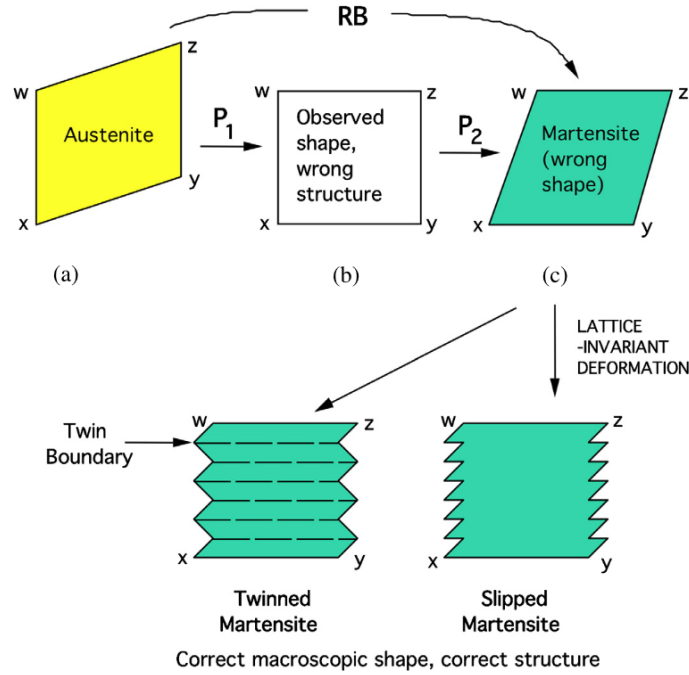


Figure 5: *Phenomenological theory of martensite crystallography: (a) the austenite lattice (b) structure with the correct shape and wrong structure after \mathbf{P}_1 (c) martensitic lattice with the wrong shape after $\mathbf{P}_1\mathbf{P}_2=\mathbf{RB}$ (bottom) final martensite with the correct structure and macroscopic shape [2].*

Before martensitic transformation, the material has a fully austenitic crystal structure shown in Figure 5(a). During martensitic transformation, the lattice shown in Figure 5(a) is deformed by IPS \mathbf{P}_1 into the correct shape (Figure 5(b)). This structure however, does not have the right lattice structure. To create the correct martensitic lattice structure another homogeneous shear transformation, \mathbf{P}_2 , is combined with the first shear transformation \mathbf{P}_1 to create the necessary ILS to transform the austenitic lattice to a ferritic lattice shown in Figure 5(c). Now, the right lattice structure is acquired with the incorrect shape as written in Equation 5:

$$\mathbf{P}_1\mathbf{P}_2 = \mathbf{RB} \quad (5)$$

This relation can also be seen in Figures 5(a-c). The combination of the correct shape and structure is obtained by implementing a lattice-invariant deformation that can either be accommodated by slip or twinning, schematically shown in the bottom of Figure 5. This type of deformation does not change the crystal structure but corrects the shape of the crystal by IPS and results in a reduction of the strain energy compared to the ILS seen in Figure 5(c). [2]

2.1.1 Habit plane

The habit plane can be defined in multiple ways as stated by Klostermann et al. [4] as: "(a) the plane of the plate of a plate-shaped crystal, (b) a semi-coherent plane glissile interface, (c) the plane boundary of a plate shaped product. If the boundaries of the plate deviate from the overall orientation of the plate, a midrib is often chosen for the habit plane." These various interpretations of the habit plane can result in different determinations of the habit plane within the same crystal. Within this thesis, the habit plane will either be defined as a plane boundary of a plate shaped product, which is situated at the γ/α' interface [28], or by the midrib as can be observed in Figure 6.

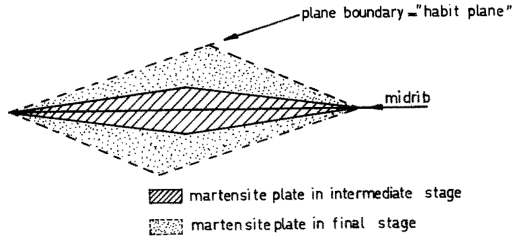


Figure 6: Schematic representation of the habit plane [4]

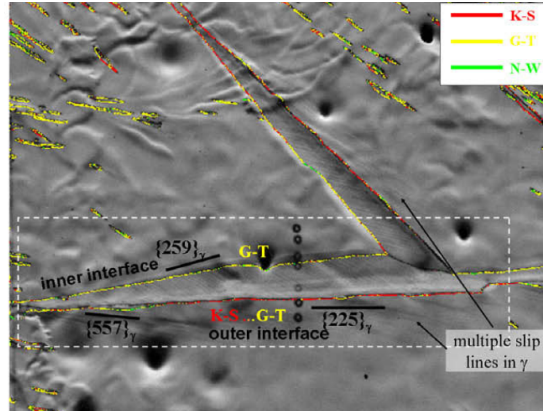


Figure 7: Distribution map of orientation relationships along the γ/α' interface together with the outcome of trace analysis to determine the habit plane of the γ/α' interface . [1]

The coherent habit plane is thought to coincide with the invariant lattice plane (ILP) (produced through PTMC). This ILP is shared between the γ and α' lattice resulting in this plane not inducing any strain or defects at the γ/α' interface which minimise the energy of the system. [28,29]

The characteristic habit plane of the butterfly wings are composed of $\{225\}_\gamma$ pair variants as shown in Figure 1, such as, for example $(225)_\gamma$ for one wing and $(\bar{2}52)_\gamma$ for the other [5,7,8,10,30–32]. These characteristic $\{225\}_\gamma$ α'_{BF} habit planes are however not always found at all of the γ/α' interfaces as shown in Figure 7. This orientation map shows that the outer interface contains characteristic $\{225\}_\gamma$ α'_{BF} habit plane whilst the inner interface of the butterfly wings contain a habit plane close to $\{259\}_\gamma$, which corresponds the characteristic habit plane of lenticular α' [1,32,33]. It can thus be stated that thermally transformed α'_{BF} nucleated with a butterfly defining $\{225\}_\gamma$ habit plane [7,34] which changes upon further cooling and growth towards $\{259\}_\gamma$ and can be attributed to accommodation dislocations [32]. During this growth stage at decreasing temperatures the accommodation mechanism changes from multiple slip to single or double slip [32] resulting in the change in habit plane from $\{225\}_\gamma$ towards $\{259\}_\gamma$.

It was found by Taisuke et al. [8] that α'_{BF} has a preference to be located in proximity of prior γ grain boundaries which is in agreement with findings by van Bohemen et al. [35] who found that γ grain boundaries are the initial and preferred nucleation zones for α' . Butterfly grains formed at these γ boundaries tend to align themselves with the neighbouring boundaries.

2.1.2 Orientation relations

The most common orientation relationships, which are relationships between specific crystallographic planes and directions that arise during the diffusionless γ (fcc) \rightarrow α' (bct) transformation, and their number of variants can be found in Table 1. However, due to its simplicity, the Bain OR is never observed in steels and is only used as a rough approximation when investigating γ (fcc) \rightarrow α' (bct) transformation [36]. As can be seen in Table 1, the N-W and Pitsch OR's are almost identical with Pitsch being the inverse of N-W. Hence, the Pitsch OR is sometimes also referred to as inverse N-W in literature [36].

Table 1: Orientation relationships during martensitic transformation

Orientation relationship	Parallel planes and directions	Number of variants
Bain [2, 23–26, 36, 37]	$\{010\}_\gamma \parallel \{010\}_{\alpha'}, \langle 001 \rangle_\gamma \parallel \langle 101 \rangle_{\alpha'}$	3
Kurdjumov–Sachs (K–S) [19, 36–38]	$\{111\}_\gamma \parallel \{110\}_{\alpha'}, \langle 110 \rangle_\gamma \parallel \langle 111 \rangle_{\alpha'}$	24
Nishiyama–Wasserman (N–W) [36–38]	$\{111\}_\gamma \parallel \{110\}_{\alpha'}, \langle 112 \rangle_\gamma \parallel \langle 110 \rangle_{\alpha'}$	12
Pitsch [36, 37, 39]	$\{110\}_\gamma \parallel \{112\}_{\alpha'}, \langle 110 \rangle_\gamma \parallel \langle 111 \rangle_{\alpha'}$	12
Greninger–Troiano (G–T) [1, 36, 40]	$\{111\}_\gamma \parallel \{110\}_{\alpha'}, \langle 123 \rangle_\gamma \parallel \langle 133 \rangle_{\alpha'}$	24

The orientation relationship between the parent γ and the α'_{BF} is described by several distinct orientation relationships like K-S OR [1, 7, 30, 34, 41], N-W OR [1, 41] and G-T OR [1, 41]. The outer interface

of the butterfly grain consists mainly of the K-S OR in combination with some G-T and the inner interface is almost purely G-T. This change in OR from K-S towards G-T can be attributed to the growth mechanism of the α'_{BF} . The wings grow firstly in the longitudinal direction and secondly in its width. During this width growth, the surrounding austenite lattice will deform notably, producing dislocations that will eventually be taken up (inherited) into the α'_{BF} grain, which conserves the G-T OR, resulting in an orientation change into the α' . This dislocation inheritance mechanism thus results in an orientation gradient that is observed within the α'_{BF} perpendicular to the γ/α' interface and explains the OR change from K-S towards G-T. Width growth probably continues until the surrounding γ is strain hardened to such a degree that further straining is not achievable. [1, 40].

2.2 Formation temperature and chemical composition

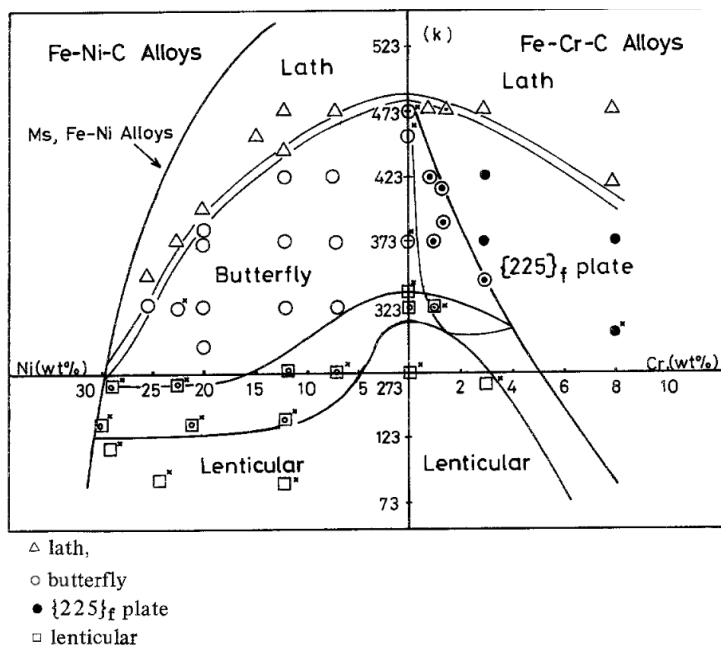


Figure 8: The morphologies of martensite that can form in Fe-Ni-C and Fe-Cr-C alloys as a functions of temperature and alloying content. [5]

Figure 8 shows the α' morphologies and their relation to composition (wt% Nickel and Chromium) and formation temperature. As can be observed from this figure, the formation temperature of α'_{BF} ranges between approximately 150-473 K, depending on the chemical composition of the alloy. In the case for Fe-Ni-C alloys that are subjected to quenching, lath α' formed prior to the formation of α'_{BF} . Increasing the nickel content will have the effect of lowering the Martensite start temperature (M_s) and formation temperature of α'_{BF} . As a result, the transition temperature from lath to butterfly-like morphology is also lowered, resulting in a morphology change from butterfly towards lath α' . [5]

The effects of the chemical composition on the formation of α'_{BF} in industrial steels (tool and bearing steel) was also investigated by Gong et al. [18]. It was found that α'_{BF} formed in alloys containing a minimum of 0.8 wt.% C which are austenised at high temperatures. The amount of alloying elements in low alloy and bearing steels are found to have little effect on the α' formation as the morphologies and quantities of α'_{BF} . Alloys with increasing carbon contents appeared to have an increased fraction of α'_{BF} . [18]

2.3 3D and 2D structures

Existing 3D descriptions of α'_{BF} are based on 2D observations. One of these 3D descriptions is shown in Figure 9a, displaying that the position of the sectioning plane along the longitudinal direction determines the two-dimensional butterfly sub-types mentioned in various research papers over the years [6, 10, 18].

The conclusion is that all of the observed two dimensional morphologies are part of the same three dimensional structure.

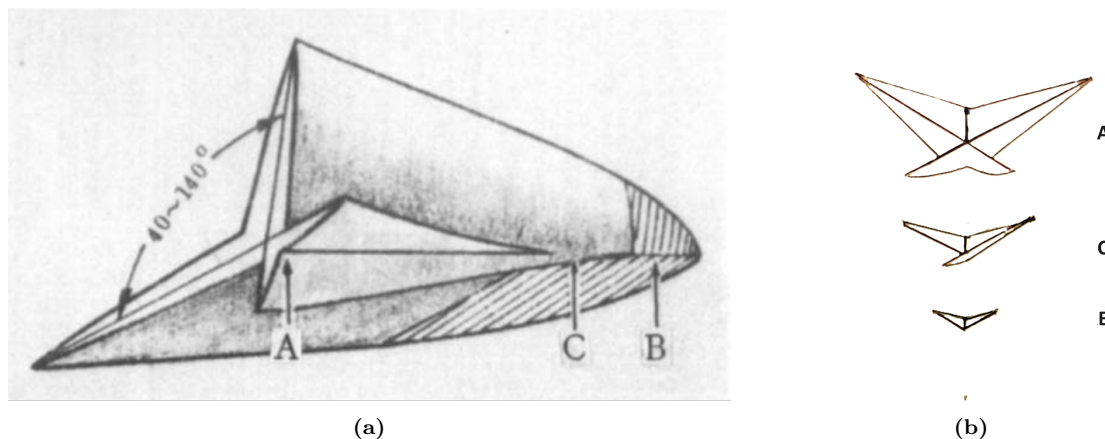


Figure 9: (a) A three dimensional representation of the butterfly martensite grain [6], (b) two dimensional butterfly morphologies acquired from slicing the three dimensional grain along the longitudinal direction at sections A, B and C.

The α'_{BF} can be subdivided in various sub-types based on the observed substructures within these sectioning planes along the length of the 3D structure. Umemoto et al. [10] subdivided the sub-types into two distinct categories base on the presence of a midrib called Type A and Type B which are described in Table 2.

Table 2: 2D butterfly martensite sub-types and their morphology/substructure according to Umemoto et al. [10]

2D butterfly martensite sub-types Umemoto [10]		
	Type A	Type B
γ/α' interface	straight	curved
Midrib	no	yes
Twinning site	outer interface pointing upward	along midrib pointing up and down towards both interfaces
Nucleations site	outer interface	midrib
Thickness	1-3 μm	10 μm
Segment in figure 9a	B	A

Gong et al. [6,18] took a different approach and subdivided the α'_{BF} morphology based on the amount of tails that were observed in the two dimensional sliced sections which can range between zero and two tails, these butterfly types based on tails are described in Table 3.

Table 3: 2D butterfly martensite sub-types and their morphology/substructure according to Gong et al. [6, 18]

2D butterfly martensite sub-types Gong [6, 18]			
	Tailless	Double tails	Single tail
γ/α' interface	straight	curved	straight and curved
Midrib	no	yes	one wing
Twinning site	outer interface pointing upward	along midrib pointing up and down towards both interfaces	one wing outer interface pointing upward and the other wing along midrib pointing up and down towards both interfaces
Nucleations site	outer interface	midrib	one wing the outer interface and the other wing along the midrib
Segment in figure 9a	B	A	C

Figure 9b shows the cross-sectional slices of the 3D α'_{BF} structure that correspond to sections A, B and C in Figure 9a. After comparing this to the various 2D α'_{BF} types described by both Umemoto et al. [10] and Gong et al. [6, 18], it can be seen that they describe the same 3D structure using different criteria. Cross-section A of the 3D description given both in Figures 9a and 9b corresponds to both Type B and Double tailed α'_{BF} as both wings contain a well defined midrib together with curved γ/α' interface. Both type A and tailless α'_{BF} describe cross-section B. As along this section of the 3D structure, shown in Figure 9b, no midribs can be observed and the γ/α' interface are straight. Cross-section C, which is also schematically drawn in Figure 9b, corresponds to single tail α'_{BF} . This type seems to be a transition between Type A and type B α'_{BF} as one wing contains a midrib structure and curved γ/α' interfaces whereas the other wing contains straight γ/α' interfaces with the absence of the midrib structure.

Moving within the three dimensional α'_{BF} structure depicted in Figure 9a from section A towards B, part of the wings below the midrib structure expected to become thinner and gradually disappear [6, 18]. This results in the midrib becoming the outer interface of the butterfly grain, first in one wing (creating cross-section C) and further towards the tip in both wings (creating cross-section B). This indicates that the nucleation site for all the previously mentioned butterfly sub-types and thus the entire three dimensional α'_{BF} grain is the twinned midrib structure. This further implies that both Gong et al. and Umemoto et al. describe the same two dimensional cross-sections of the three dimensional butterfly morphology.

2.4 2D substructures

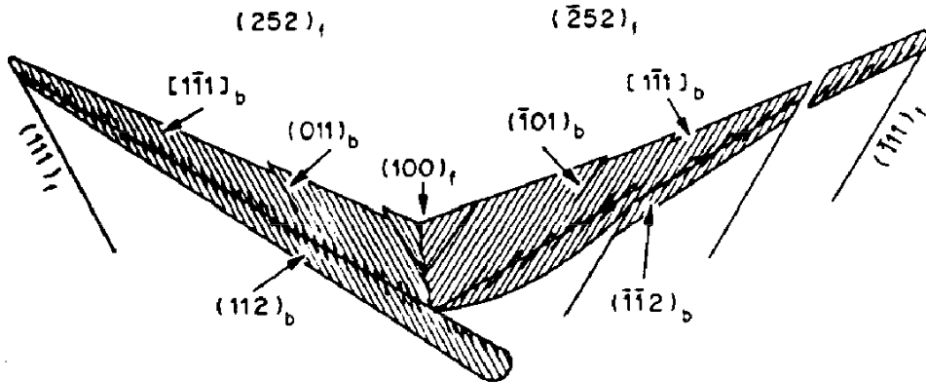


Figure 10: Schematic representation of the substructures that are found within butterfly martensite [7]

Figure 10 shows a schematic representation of the substructures that can be found within the α'_{BF} grain. A fully twinned midrib can be observed along the entire length of the wings close to parallel to the $\{225\}_{\gamma}$ plane. The midrib structure cannot always be observed and is thus not a defining feature on which α'_{BF} can be characterised. The uniformity and thus low angle boundary density within the butterfly wings are a more sufficient way to characterise α'_{BF} [8]. The internal boundary density is small within α'_{BF} compared to, for example, lath α' [8].

Outside of the twinned area, the substructure will be mainly comprised of dislocations. The high density of dislocations found surrounding the twinned region is a result of the accommodation process of lattice distortions from the transformation of γ into α' as the α' phase grows [42].

As can be seen in Figure 10, the two butterfly wings are adjoined to each other through a smooth and straight interface called the junction plane, which is situated along the $\{100\}_{\gamma}$ plane [5, 7, 8, 10, 30, 31]. However, this interface can be quite irregular. The concentrations of defects in α'_{BF} on the junction plane is significantly lower compared to the density of defects along the midrib as well as the γ/α' interface [18]. Hence, it was concluded that the junction plane is comparable to a twinning plane together with the fact that the butterfly wings show mirror symmetry with respect to the junction plane [18].

2.5 Formation and growth

During formation, the fully twinned region or midrib is the first structure to nucleate (with K-S OR [1,41]) due to the mechanism of self-accommodation, which lowers the strain energy of the system [6,33]. This self-accommodation happens at relatively high temperature ranging between 333 K and 473 K because the E-modulus is lower at elevated temperatures. However, at these elevated temperatures, the slip shear stress is also lower resulting in limited growth of the thin plate width as the rise in slip shear strain energy causes slip shearing. Thus it can be concluded that the main mechanism of α'_{BF} growth is through slip shearing which results in an increase in dislocations. The surrounding parent γ will also see an increase in dislocations during the growth of α'_{BF} due to accommodation deformation through slip. [6]

The formation of tailed/Type B α'_{BF} is assumed to follow the following steps that can occur either separately or at once depending on many factors and can be seen in Figure 11a: [6]

1. Formation of the twinned thin plates (midribs)
2. Thickening takes place along the upper side of the midribs
3. Growth of the bottom side of one wing combined with the formation of the tail(s)
4. Growth of the bottom side of the other wing

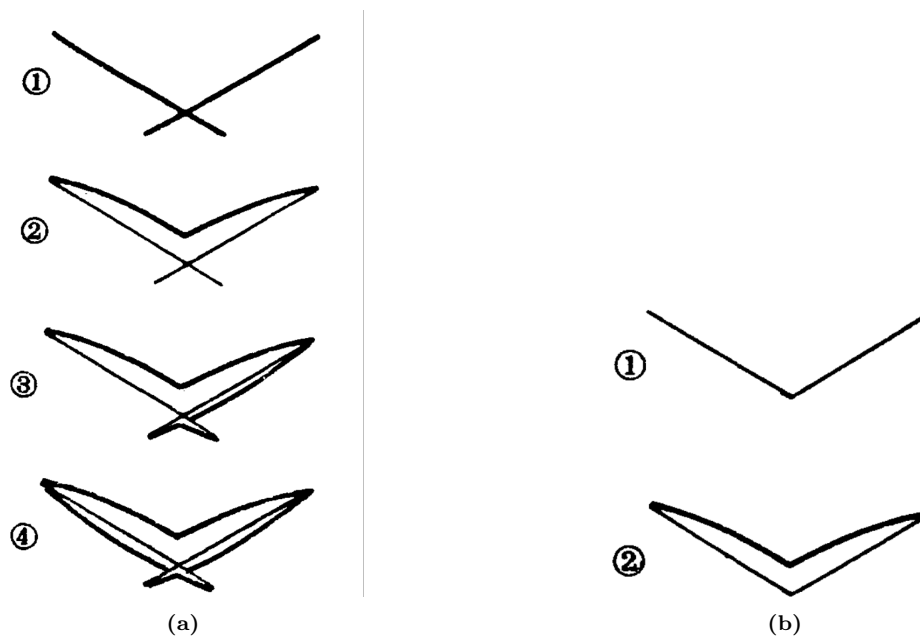


Figure 11: (a) Schematic representation of the formation of butterfly with tails [6], (b) Schematic representation of the formation of butterfly without tails [6]

Tailless or Type A α'_{BF} , on the other hand forms due to the formation of two kinked thin- α' plates which are then thickened on the upper side only as seen in Figure 11b. As the α'_{BF} growth of the tailless sub-type is restricted to the upper side of the wings, a large transformation stress field will be present at the upper side that will be large enough to inhibit further α' formation and causes bands of retained γ to appear. [6]

It is deduced that the growth of the upper region of both of the wings, shown in Figures 11a.2 and 11b.2, must grow in unison as otherwise the dislocation density within the junction plane, which is the intersection plane between both wings, must be higher [18].

In addition to being α' nucleation zones, γ grain boundaries also act as obstacles for α' growth. α'_{BF} nucleation near a γ grain boundary can result in a change in morphology in a way that the butterfly grain does not always contain the characteristic paired wing plates. As one wing grows into the γ grain, the growth of the other pair variant is restricted by the γ grain boundary, resulting in a α'_{BF} block

morphology that is schematically drawn in Figure 12, where their shape is irregular and only one of the two wing pair variants can be observed. [8]

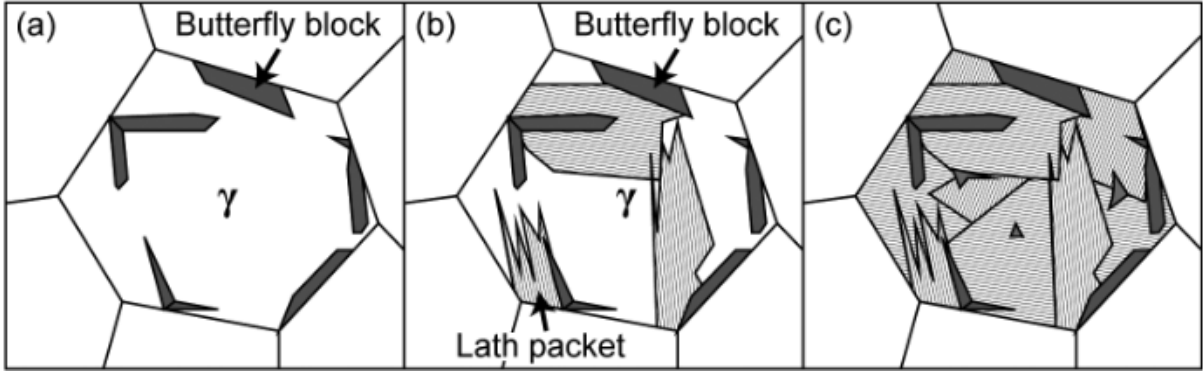


Figure 12: (a) Butterfly grain nucleation along the austenite grain boundary, (b) lath martensite nucleation at the austenite grain boundary and growing parallel to the first formed butterfly grain, (c) complete transformation of the prior austenite grain to lath martensite together with some small butterfly grains. [8]

2.6 Catalytic formation

Auto-catalytic formation is assumed to be associated with dislocation formation into the surrounding γ during $\gamma \rightarrow \alpha'$ transformation which first assist the formation of α' by acting as nucleation points [9,43–46]. When the first α'_{BF} grain has formed, it will deform the surrounding γ matrix and create stress fields near the concavity and convexity of the first formed α' . These stresses can cause dislocations to pile up within these high stress region and cause new α' nuclei to form when enough driving force is available to drive this phase change. Dislocations within the γ will pile up to form a nucleus when the driving stress is equal or larger than the combination of lattice drag and the repelling forces related to other previously formed dislocation pile ups which is formulated in Equation 6.

$$\tau_{[\bar{1}10]} \geq \tau_s + \tau_p \quad (6)$$

Where $\tau_{[\bar{1}10]}$ is the driving stress, τ_s is the lattice friction and τ_p is the repelling stress.

Secondary formed α'_{BF} nuclei are formed near stress field situated at the concavity and convexity of the first formed α' . Due to the existence of compressive stresses near the concavity, α'_{BF} is more likely to nucleate near the convexity where there is a tensile stress field. The isostress lines of $\tau_{[\bar{1}10]}$ show large stresses near the concavity, convexity and the wing tips. These isostresses can be seen in figure 13. However, new α'_{BF} is not likely to form near the butterfly wing tips, as the tensile stress field around the tip is relatively low due to its usually branched and blunt shape in contrast to the sharp tip model that was used to calculate the isostress. Secondary formed α'_{BF} will most probably nucleate within $2 \mu\text{m}$ from the convexity (Figure 13) which is in agreement with microscopical observations. This can cause a catalytic reaction resulting in a string of α'_{BF} that forms during the early stage of the transformation as can be observed in Figure 14a. This string of butterflies will resemble a single, fat α'_{BF} grain. As stated above, the region near the convexity is the most likely region for α'_{BF} to nucleate. However, α'_{BF} can also nucleate near the more unfavourable concavity region. If the compressive stress is large enough resulting in dislocation pile-ups combined with enough thermal energy to counter the strain energy, small butterfly grains can be formed, shown in Figure 14b. It is observed that α'_{BF} near the concavity is smaller compared to α'_{BF} formed near the convexity. [9]

However, when the strain that is introduced by the dislocations within the surrounding austenite reaches a critical point, mechanical stabilisation will occur, preventing further α' formation as the dislocations prevent movement of the glissile interfaces, preventing growth [44–46]. This might explain why these stacked α'_{BF} grain do not extend across the entire length of the parent γ grain.

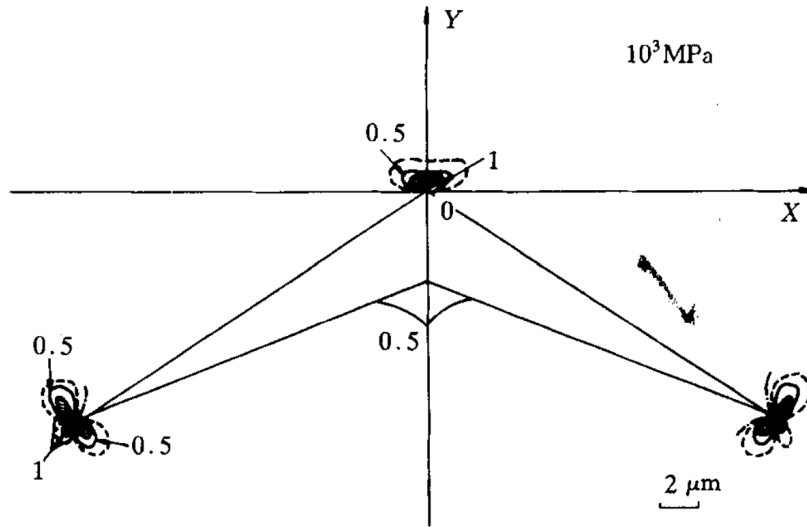


Figure 13: Isostress lines of $\tau_{[110](111)}$ [9]

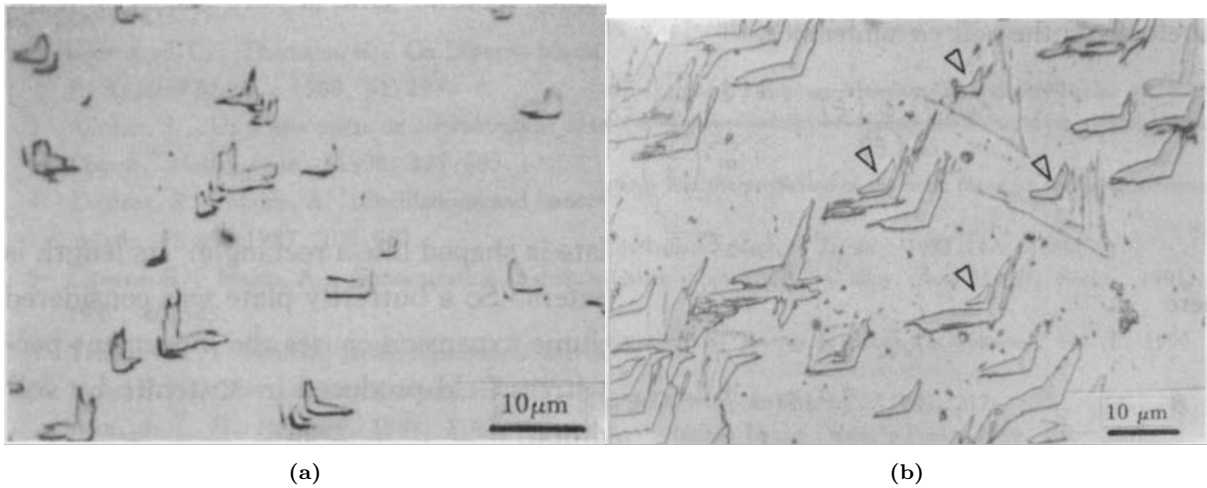


Figure 14: (a) Butterfly martensite grains formed at the convexity of first formed butterfly grains, (b) Butterfly martensite grains formed at the concavity of first formed butterfly grains. [9]

2.7 Wing angle

Determining a true wing angle based on serial sectioning is difficult as the sectioning must be perfectly perpendicular to the opening axis of the butterfly grain [1]. The wing angle found by microscopical observation of these sections is called the apparent wing angle. This apparent wing angle can be determined when the configurations of the twins are known together with the orientation of the surface that has been observed [33].

Estimating the true wing angle is more complex and can be approximated in four steps. Firstly, one needs to determine the crystal orientation of both the α'_{BF} wings and the plane that is being observed. Secondly, the habit planes and twin plane will need to be calculated by the phenomenological theory of martensite crystallography (PTMC), depending on the type of pattern, after which apparent wing angles can be calculated and lastly compared to the observed apparent wing angles. The true wing angle is thus dependent upon the substructure of the α'_{BF} wing plates. [33]

Niho et al. [33] identified the most common wing angles to be ranging between 90-110° in a medium carbon steel. Other research found different wing angles through calculation and experimental observation through serial sectioning of tool and bearing steel. Here, the most common angles were observed to

be situated between 120° and 140° [7, 10, 18]. Acute angles were rarely observed [7, 10, 18, 33]. It can be concluded that the bulk of the butterfly wing angles are indeed obtuse and lie within a range between 90° - 140° .

2.8 Effect of prior austenite grain size (PAGS)

α'_{BF} forms mainly upon high austenisation temperatures (T_A) ($1273\text{ K} \leq T_A \leq 1573\text{ K}$) [18, 34]. Increasing the T_A resulted in an increase of the M_s as the γ grains became larger [34]. These bigger PAGS will have larger degree of homogenisation within the γ grains resulting in a more perfect crystal which causes a reduction in the energy needed to initiate α' growth resulting in an increase in the M_s and larger α' structures [31, 42]. Large PAGS and therefore high T_A thus seem favourable in the formation of α'_{BF} [18]. The T_A and time which the alloy spends at T_A (t_A) both have a large effect on the PAGS and thus the M_s [31, 34]. Over-austenising the material may inhibit the formation of α'_{BF} . If the thermal holding process at T_A is too long, the PAGS will become larger, increasing the M_s and thus increasing the amount of undercooling below M_s at the same quenching process, resulting in a morphology combined of lath and lenticular α' instead the butterfly morphology [31]. The choice in T_A and t_A is thus a balancing act to create the correct PAGS to be able to obtain the optimal α'_{BF} formation temperature.

2.9 Formed upon mechanical polishing

α'_{BF} can also be induced by the mechanical polishing. This results in a special type of strain induced α'_{BF} which is situated only at the surface of the polished sample at depths of around $5\text{-}50\ \mu\text{m}$ as mechanical polishing induces surface strain only. This type of butterfly grain is characterised by wing that are stout, meaning that they are thick and short in nature together with an irregular γ/α' interface. An interesting observation that can be made from the electron micrograph in Figure 15 is that even the outer γ/α' interface, which is the nucleation side, contains irregular and sharp tips. In other types of α'_{BF} , this outer interface is usually smooth and planar. [10]

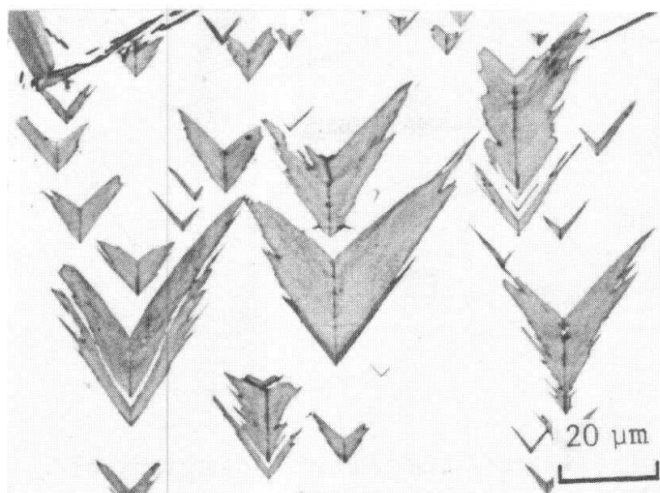


Figure 15: Electron micrograph of strain-induced butterfly martensite formed through mechanical polishing of the surface at room temperature. [10]

This strain induced transformation occurs in alloys with M_s close to room temperature or cooled just below room temperature. The habit plane of strain induced α'_{BF} that is formed upon polishing is not known, however, it is thought to be identical to previously mentioned Type A and Type B α'_{BF} that is formed thermally. The junction plane is also identical to all previously mentioned α'_{BF} at $\{100\}_\gamma$. As seen in Figure 15, no midrib is observed in these short and stout butterfly grains, which is similar to the Type B α'_{BF} . [10]

The thick and stubby shape of the α'_{BF} shown in Figure 15 could however also be caused by the angle of the butterfly grain with respect to the observation surface. If the observation surface is at a large angle to the opening axis of the butterfly grain, the shape of the butterfly grain can become distorted in a similar manner as seen in this micrograph.

2.10 EBSD

EBSD is a characterisation technique employed in conjunction with a scanning electron microscope (SEM). This method finds widespread application in determining crystal orientations, textures, and phases present on the surface of material samples. The spatial and depth resolutions of EBSD are contingent upon factors such as the angle of the sample relative to the incoming electron beam, the specimen's density, and the acceleration voltage utilised for the electron beam. To mitigate backscatter electron noise from Kikuchi patterns, specimens are often tilted by approximately 70° with respect to the horizontal plane.

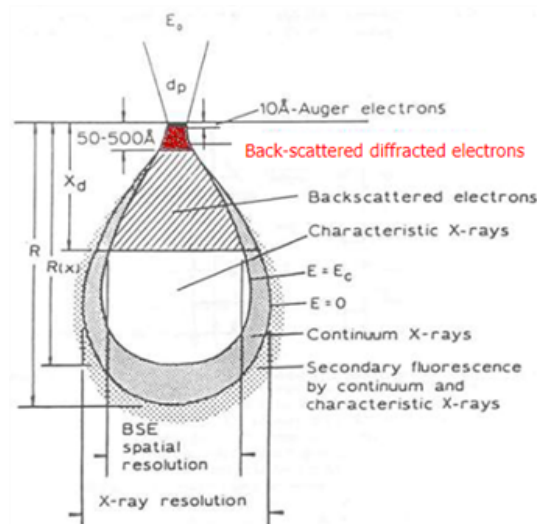


Figure 16: *Figure 16 generation depth of back-scatered diffracted electrons [11]*

For electrons to reach the detector, they must undergo diffraction upon entering the material. This diffraction process adheres to Bragg's law (Eq. 7). The backscattered, diffracted electrons utilised in EBSD analysis originate from depths ranging between 50 and 500 Angstroms within the material sample, as depicted in Figure 16.

$$n\lambda = 2d_{hkl} \cdot \sin(\Theta) \quad (7)$$

2.10.1 Kikuchi patterns

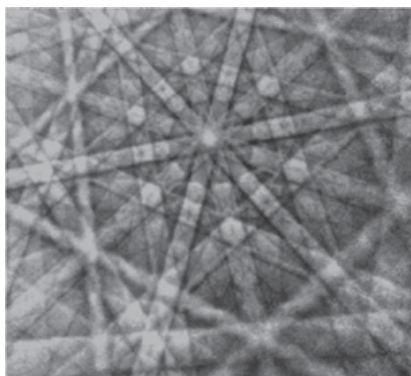


Figure 17: *Kikuchi patter acquired by EBSD [12]*

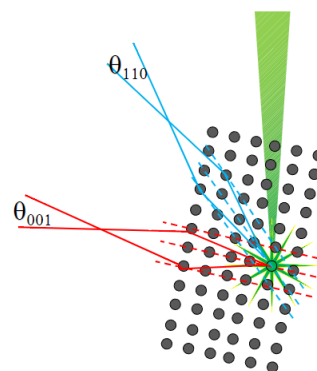


Figure 18: *Schematic representation of the scattering of an incoming electron beam which satisfies Bragg's diffraction creating Kikuchi bands, made by C. Kwakernaak [13]*

When backscattered electrons are captured by a phosphor screen detector, they form Kikuchi patterns, as illustrated in Figure 17.

Despite electrons being scattered in all directions, the EBSD detector discerns a structured pattern arising from the backscattered electrons. This phenomenon is attributed to the selective channelling of electrons satisfying Bragg's condition between specific crystallographic planes, as depicted in Figure 18. Consequently, Kikuchi patterns are material, orientation, and phase-specific due to variations in the material's interplanar spacing (Kikuchi band width) and interplanar angles (angles between Kikuchi bands) [12]. These patterns serve as pivotal indicators of crystal phase and orientation. Notably, the observation of Kikuchi patterns necessitates localisation to a small area. Attempting to analyse larger regions may yield a uniformly bright image due to the overwhelming number of overlapping Kikuchi patterns.

2.10.2 Orientation maps

To index Kikuchi patterns computationally, a Hough transformation is executed. During this transformation, individual pixels are mapped onto a sinusoidal curve in Hough space, representing all possible lines that can go through these individual pixels with high-intensity sinusoidal curves representing pixels of high intensity. The accumulation of these sinusoidal curves allows for the identification of co-linear pixels in Hough space. Intersections of these accumulated lines result in a spot that has an intensity that is equal to the sum intensities found along the lines of the image which manifest as so called "butterfly peaks" in the resultant image. [12]

Subsequently, upon completion of the Hough transformation, the Kikuchi bands corresponding to these peaks are discerned, facilitating the indexing of the diffraction pattern. This process is iteratively performed for each pixel and associated Kikuchi pattern within the original image, enabling the generation of phase and orientation maps. An illustrative example of a Hough transformation is depicted in Figure 19.

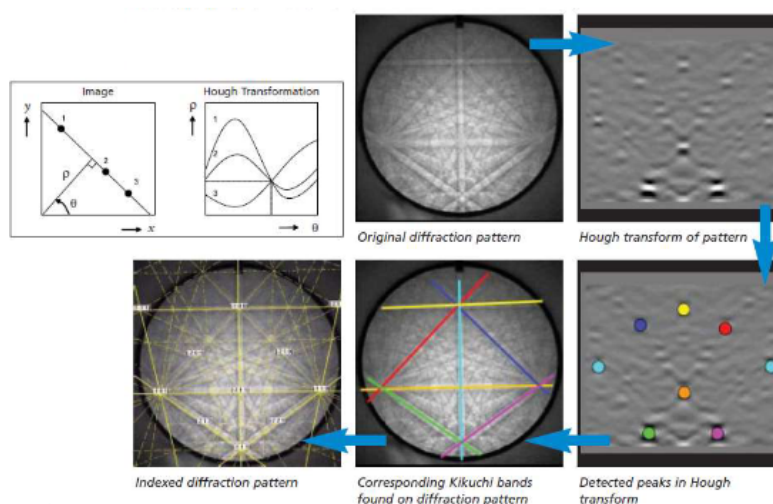


Figure 19: *Processing order of obtaining a kikuchi pattern using a Hough transformation [14]*

2.10.3 (inverse) pole figures

Pole figures serve as a conventional means of depicting the distribution of crystallographic grain orientations or texture within a material, with the sample's reference directions (ND, TD, or RD) aligned with specific crystallographic poles [12]. Essentially, a pole figure provides a two-dimensional stereographic representation of a three-dimensional crystal, as illustrated in Figure 20.

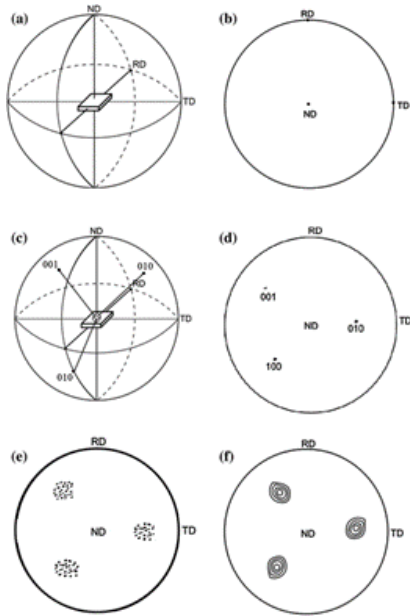


Figure 20: Pole figure formation [15]

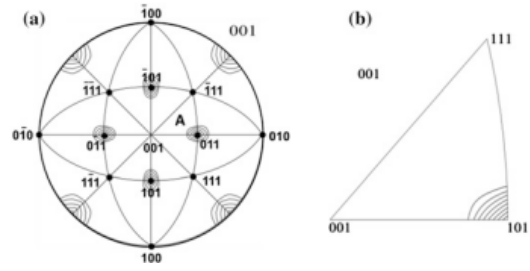


Figure 21: (a) Pole figure (b) stereographic triangle [15]

Conversely, an inverse pole figure serves to delineate crystallographic poles aligned with particular sample directions. Inverse pole figures, as opposed to pole figures, exhibit a stereographic representation of crystallographic poles corresponding to specific sample directions [12]. For materials possessing cubic symmetry, a full inverse pole figure presents a 24-fold redundancy. Consequently, it can be condensed into a single stereographic triangle, exemplified in Figure 21. This triangular representation signifies that the sample, exhibiting a cubic texture, exhibits a preferred crystallographic orientation aligned along the 001 direction.

3 Materials and methods

3.1 Material and specimen preparation

It order to choose a suitable alloy a search was done through pre-existing literature to determine in what kind of alloys α'_{BF} is most likely to form. Through this literature review it was found that most α'_{BF} formed in steel alloys with a high nickel content ranging between 10.3-40.2 wt.% [1, 7, 10, 30, 31, 34, 40-42, 47-54]. Thus, the choice was made to select a high nickel steel alloy, called 25Ni, for this thesis with composition shown in Table 4. The role of nickel as an austenite stabiliser extends the stability of austenite across a broader temperature spectrum. The M_s is thus expected to decrease as the nickel content is increased. This 25Ni alloy lies precisely in the middle of the given nickel weight fraction at which α'_{BF} is thought to most likely form and is hence thought to be a suitable candidate for α'_{BF} research. The choice for this alloy is further solidified as it was previously used by Breukelman et al. [55, 56] showing the butterfly martensite morphology. The alloy was vacuum cast in an 80 mm x 80 mm x 400 mm billet that was subsequently forged to a 50 mm x 50 mm x 1000 mm billet and homogenised at 1273 K for 12h. Cylindrical dilatometry specimens, 4 mm in diameter and 10 mm long, were produced by means of Electrical Discharge Machining (EDM) from the homogenised billets.

Table 4: Chemical composition 25Ni alloy

Alloy	C wt%	Ni wt%	Mn wt%	Al wt%	S wt%	P wt%	Cr wt%	Si wt%	Mo wt%
25Ni	0.20	24.90	0.02	0.005	0.002	0.003	0.02	<0.01	<0.01

3.2 Heat treatment

During this research, three different types of heat treatments are used in order to obtain a mixed morphology containing γ and α'_{BF} . Schematic representations can be seen in Figure 22. During the first experiments a combination of oven heating/cooling and liquid nitrogen (LN) quenching was employed. The temperature profile of this treatment is shown in Figure 22a. This thermal treatment was chosen as the starting treatment as previous research [55, 56] found α'_{BF} using this treatment in combination with the 25Ni alloy. As it was found that this heat treatment applied too much undercooling to the sample, the choice was made to eliminate the LN quenching treatment, leading to the heat treatment found in Figure 22b. In order to obtain more reliable results from this treatment, as the cooling step within the oven was non-linear and deviated from the applied (linear) temperature program (shown in Figure 23), the choice was made to employ the use of a dilatometer. During the dilatometry experiments, a thermocouple is applied to the sample itself. This results in the possibility to be able to better control the thermal treatment (heating rate, cooling rate and cooling temperature), obtain more consistent and qualitative data on the M_s of the material and gain insight into the $\gamma \rightarrow \alpha'$ transformation progression. The heat treatment used within the dilatometer can be observed in Figure 22c. The material samples that were processed using these various thermal treatments can be found in Table 5.

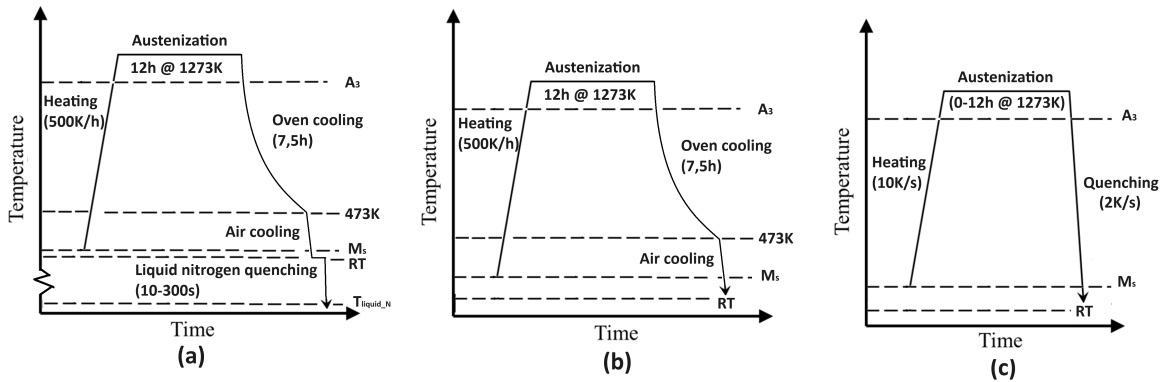


Figure 22: Schematic representation of the thermal treatments used during (a) oven and liquid nitrogen quenching experiments, (b) oven and air cooling experiments and (c) dilatometry experiments

Table 5: *Samples and heat treatment*

Samples and heat treatment							
Treatment	Sample name	T _{Aus} (K)	t _{Aus} (h)	T _{Quench} (K)	time submerged in liquid N (s)	Quenching medium	Cooling rate (K/s)
Oven+liquid N							
	O_N300s	1273	12	77	300	LN	Unknown (≈ 55 ¹)
	O_N200s	1273	12	77	200	LN	
	O_N100s	1273	12	77	100	LN	
	O_N50s	1273	12	77	50	LN	
	O_N10s	1273	12	77	10	LN	
Oven+Air cool							
	O_AC_1	1273	12	RT		Ambient air /aluminium plate	Unknown (≈ 3.5 ²)
	O_AC_TC	1273	12	RT			
Dilatometry							
	D_0hAus_c	1273	0	243		LN	2
	D_1hAus	1273	1	RT		Helium gas	2
	D_1hAus_c	1273	1	243		LN	2
	D_2hAus	1273	2	RT		Helium gas	2
	D_4hAus	1273	4	RT		Helium gas	2
	D_6hAus	1273	6	RT		Helium gas	2
	D_8hAus	1273	8	RT		Helium gas	2
	D_10hAus	1273	10	RT		Helium gas	2
	D_12hAus	1273	12	RT		Helium gas	2
As-received							
	As-received	x	x	x	x	x	x

Oven treatment: The oven heat treatments were performed inside a Nabertherm LT15/14 furnace equipped with a C550 controller and limiter which heated the samples up to 1273 K at a heating rate of approximately 500 K/h where it is held for 12 hours after which the sample is supposed to be cooled back to room temperature (RT) within 4 hours. This applied temperature program can be observed by the yellow line in Figure 23. However, the oven did not follow this cooling rate, shown by the blue line in Figure 23 which shows the actual temperature within the heating chamber of the oven measured by a thermocouple touching the sample. As the actual cooling rate was much slower than the set cooling rate (taking ± 7.5 hours to cool the sample from 1273 K down to 473 K), the choice was made to take the sample out of the furnace and cool it further to RT by placing in onto a aluminium plate.

LN quenching experiments were conducted by fully immersing the specimens in a LN bath following the oven treatment. Specifics regarding these LN quenching experiments can be observed in Table 5

¹Estimated using Newton's law of cooling

²Estimated using Fourier's law of conduction

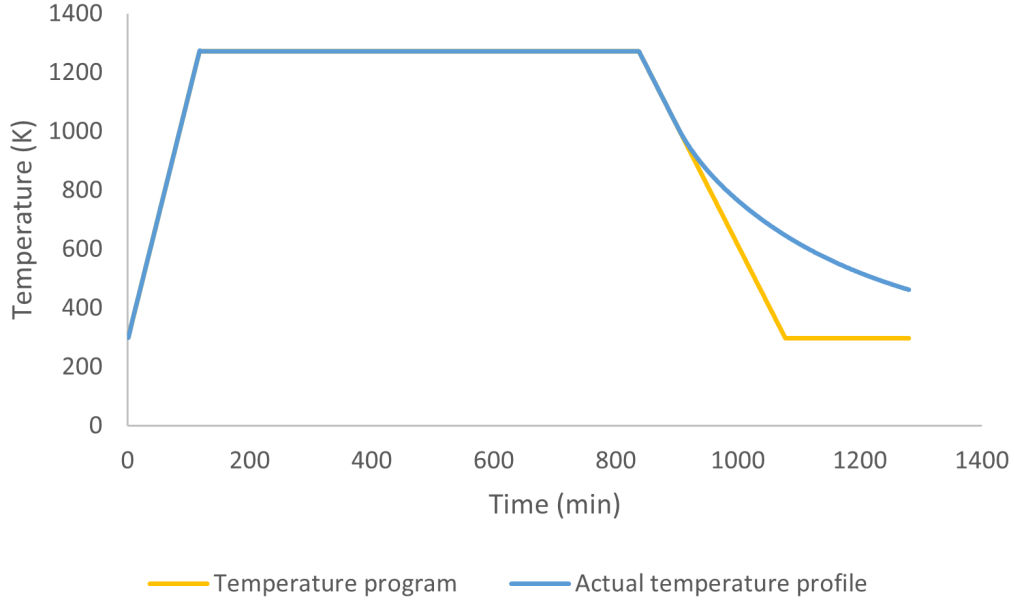


Figure 23: Graph showing the discrepancy between the applied temperature program (yellow line) and the actual temperature profile within the heating chamber of the oven during the *O-AC-TC* experiment (blue line)

Dilatometry: To be able to obtain the butterfly martensite microstructure in a more controlled manner, quenching heat treatments were performed using the Bähr DIL 805A/D dilatometer. Dilatometry specimens were heated up to 1273 K at a heating rate of 10 K/s to obtain a fully austenitic microstructure. Specimens were subjected to an isothermal holding at this temperature for various amounts of time ranging from 1 up to 12 hours to increase the austenite grain size after which they were quenched, below M_s , to RT at a cooling rate of 2 K/s to induce the martensite transformation. During both heating and cooling a vacuum was maintained of $2 \cdot 10^{-4}$ mbar. Below 473 K, helium gas was used to complete the cooling towards RT.

Cryogenic dilatometry experiments were also conducted using similar experimental procedures as the conventional dilatometry experiments mentioned above. However, during cooling stage the sample is cooled with LN down to 243 K under atmospheric pressure.

Dilatometry was also employed to investigate the formation of carbides within the material. The material was heated to both 898 K and 1123 K at a heating rate of 10 K/s. As these temperatures were reached, the samples were immediately cooled back to RT at a cooling rate of 2 K/s.

3.3 Microstructure characterisation

3.3.1 Sample preparation for light optical microscopy (LOM) and SEM/EBSD

Samples were prepared for both optical and electron microscopy by cutting them in half using Struers Accutom-100 precision saw on the lowest force setting at 0.1 mm/s and 3000 rpm to reduce the amount of surface stress applied whilst cutting. To reveal the martensitic microstructure, electropolishing was applied by Struers Lectropol 5 using Struers A2 electrolyte at 295 K with a flow rate of 7 instead of mechanical post-processing in order to inhibit mechanical stresses and strains onto the observation surface as α'_{BF} can form on the surface of the specimen upon mechanical polishing at room temperature [10].

To observe the austenite grain size and, specimens were etched using Kalling's #2 reagent (5g CuCl_2 + 100ml of HCl at 33% + 100ml Ethylalcohol) instead of being electropolished as Kalling's #2 reagent gives a better contrast between the γ and α' phases.

3.3.2 LOM

LOM was performed using the Keyence VHX-7000N digital microscope with mixed lighting setting and a stage angle of 0° . In order to observe the complete cross-sectional surface area and determine the α' phase fraction, a serial recording is made consisting of five images (top, bottom, left, right and centre of the sample cross-section) taken at X100 magnification. These images were then stitched together in dark mode in order to create one large image of the sample cross-section.

3.3.3 SEM and EBSD

A SEM was used to obtain detailed images of the α'_{BF} grains. Both backscatter and secondary electron images were taken using the JEOL JSM-6500F SEM with a work distance of 10 mm together with an acceleration voltage of 15-20kV.

The JEOL JSM-6500F SEM was also used to obtain a more detailed microstructural characterisation using EBSD. EBSD data was analysed using EDAX OIM software version 8.

To determine the habit planes, the following method was employed: Traces of well-known martensite habit planes were superimposed on electron micrographs. The habit plane whose trace closest to parallel with the observed interface trace of the α'_{BF} grain was assumed as the habit plane. [1, 5, 7, 30, 40, 49]

OR determined by comparing the axis-angle pairs calculated by EDAX OIM software shown in Table 6 with experimentally obtained axis-angle results using a tolerance of 1.5° .

Table 6: *Axis-angle pairs corresponding to various γ/α' orientation relationships*

OR	Axis-angle
Kurdjumov-Sachs	$42.85\langle 11\ 2\ 2\rangle$
Nishiyama-Wasserman	$45.98\langle 14\ 1\ 3\rangle$
Greninger-Troiano	$44.23\langle 15\ 3\ 2\rangle$

3.3.4 Serial sectioning

Serial sectioning of a butterfly grain was performed by removing material from the sample surface by polishing first with a $1\ \mu\text{m}$ solution for 1-2 minutes and secondly with an oxide polishing suspension (OPS) for 10-12 minutes to ensure the removal of between 1-3 μm of material from the sample surface and a smooth observation surface on which microstructural features are visible with LOM. Manual polishing using OPS was chosen for this technique over electropolishing in order to inhibit the shadowing effect created by electropolishing as α' is etched away at a faster rate compared to γ , resulting in a height difference leading to shadows on the surface. This height difference and the shadowing will result in a bad indexation of the interface and surrounding area. After polishing EBSD was performed using the Helios G4 SEM. EBSD data was collected from each slice using an acceleration voltage of 15 kV and a beam current of 13 nA.

3.3.5 3D-EBSD

Lastly, 3D-EBSD was performed. A volume of approximately $31.65 \times 35.25 \times 25.6\ \mu\text{m}^3$ was extracted for serial sectioning using a dual-beam FEI Helios G4 Xe^+ PFIB. A Pt layer was first deposited onto the surface of the 25Ni sample on top of the chosen α'_{BF} grain after which trenches were dug around this area in order to lift the volume out. This volume was lifted out with a micromanipulator within the microscope chamber and then attached to a Si substrate using Pt deposition. The Si substrate was subsequently mounted on a specially designed pre-tilted holder for 3D-EBSD experiments (Micro-to-Nano EBSD 3D sample folder for FEI/thermo dual beam system) with a sample pre-tilt of 54° . The sample holder was further tilted by an additional 16° such that the sample can be rotated by 180° for the ion milling and EBSD stages which are performed at angles of 38° and 70° , respectively. Sectioning and EBSD scans were managed by the FEI Auto-slice-and-view software. The slice thickness was set to $0.1\ \mu\text{m}$, and EBSD data were collected every other slice, resulting in a final z-resolution of $0.2\ \mu\text{m}$. A

beam current of 15 nA was used for slicing the block, with each slice taking approximately 2 minutes. A 5° rocking mill was employed to prevent curtaining effects. EBSD was collected on each slice at a work distance of 3.85 mm, acceleration voltage of 15 kV with a current of 13 nA using an EDAX Hikari Gen3c detector and the EDAX APEX control software. Each EBSD map covered the entire sample face with a 0.15 μm step size in approximately 15 minutes. The final dataset comprised 178 individual slices and required approximately 58 hours to collect. Reconstruction steps, including importing the raw data, thresholding, alignment, clean-up, and segmentation, were performed using DREAM3D-NX software.

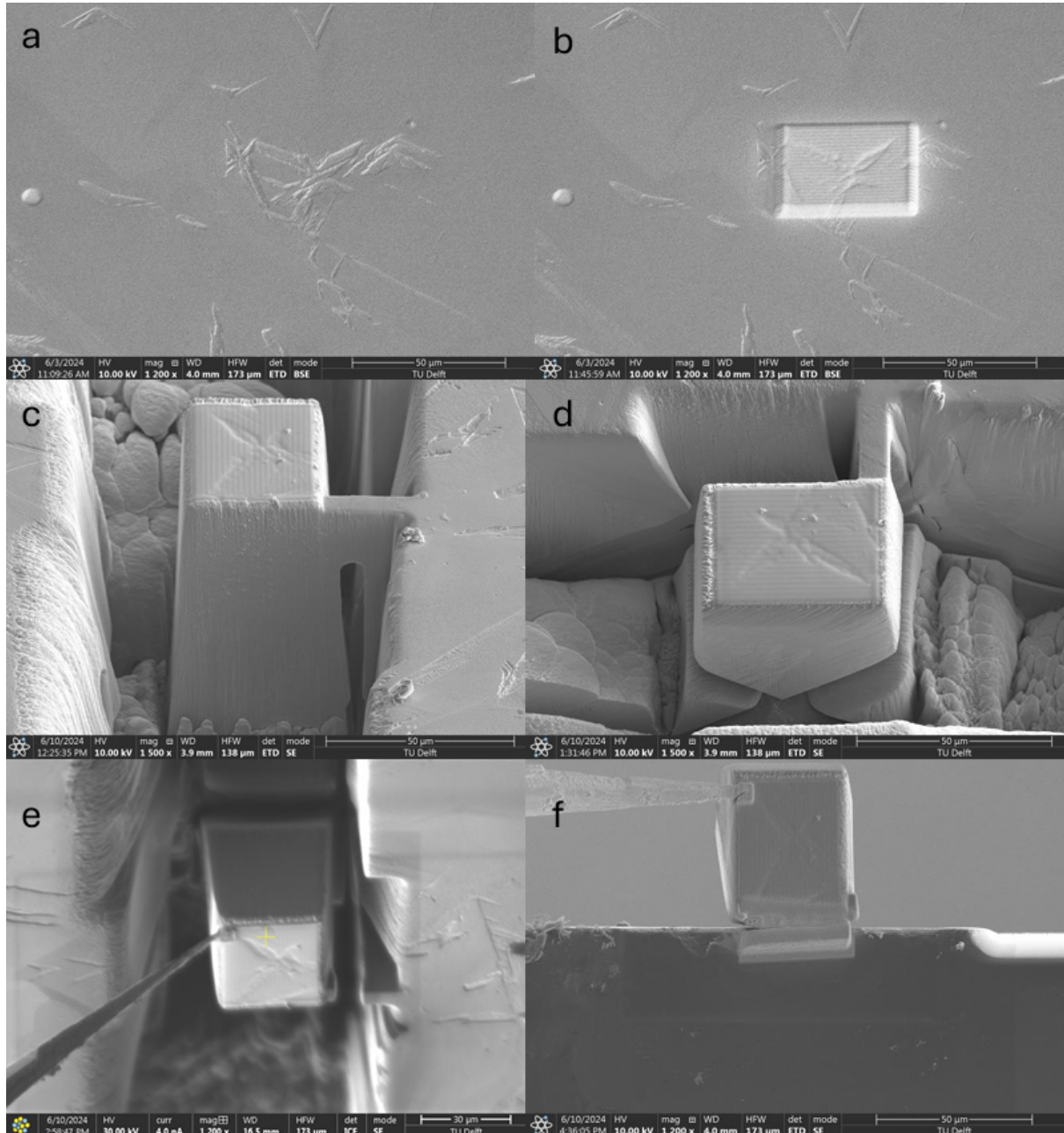


Figure 24: (a) Surface of the As-received sample showing the butterfly morphology, (b) Pt layer applied over a single α'_{BF} grain which is selected for FIB-3D-EBSD, (c) FIB-Milling of trenches around the selected α'_{BF} grain leaving a small bridge attached for stability, (d) undercutting the selected volume at 45° in order to remove the volume after cutting the bridge, (e) attaching a micromanipulator to the volume and removing the bridge and (f) removal of the volume

3.3.6 DREAM3D-NX: 3D reconstruction, cleanup and filtering

After 3D-EBSD is completed, the raw data was saved as an .edaxh5 file. This type of file could not be processed by the DREAM3D-NX software. The raw 3D-EBSD data is converted to .ang files [57] and the EDAX hexagonal grid is transformed into a square grid in order to be processed with the software

by using the build in function within the EDAX OIM software. By using the DREAM3D-NX filter "import orientation file(s) to H5EBSD" these .ang files are converted to the .h5ebbsd format needed for DREAM3D-NX processing. Next, the filter "READ h5EBSD" can be applied in order for the program to load in the acquired 3D-EBSD data. In order to make a clear 3D model of α'_{BF} grains, all of the slices must first be aligned which can be done by using the "Align sections (Misorientation)" filter. An image before and after section alignment can be seen in Figures 25.a and 25.b, respectively. Data cleanup is performed by using the filter "Replace Element Attributes With Neighbor (Threshold)". This cleanup step removes any badly indexed pixels. The "Crop Geometry (Image)" filter can be used to crop the volume to a size which can be better used to observe a single 3D grain (Figure 25.d). Various other filters can be applied in order to obtain the required data information and views as can be seen in Figure 25.f. Next, visual threshold filters can be applied in order to obtain the optimal 3D view of an individual α'_{BF} grain (Figures 25.c and 25.e).

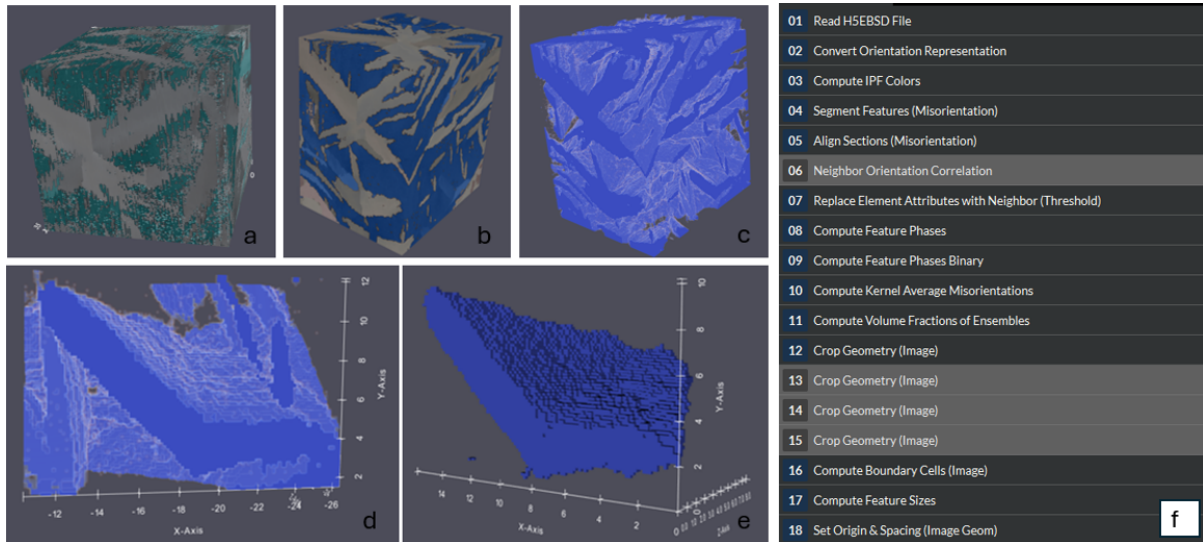


Figure 25: The (visual) filters that are applied in order to observe a single α'_{BF} grain. (a) original volume, (b) volume after slice alignment and noise filtering, (c) removal of the γ phase, (d) cropping of the volume to single out a single α'_{BF} grain, (e) filtering out the remaining surrounding α' through among others IPF colour and FeatureIds, (f) list of filters applied within Dream3D-NX in order to obtain a 3D image of a butterfly grain

4 Results and Discussion

4.1 Investigation of the as-received material

The as-received material contained a mixed morphology of both γ with a mean grain size of $89 \pm 5 \mu\text{m}$ and α'_{BF} . Phase fraction measurements performed with LOM, as shown in figure 26, shows that the sample contained $11\% \pm 1\%$ α'_{BF} . As can be seen in this figure, these α'_{BF} grains were not homogeneously distributed across the surface as dense clusters were observed which could indicate catalytic formation of the butterfly grains as mentioned by Chen et al. [9] where new α'_{BF} grains nucleate and grow due to stress fields at both the convexity and concavity of the prior formed α'_{BF} grain. Appendix A shows a continuous cooling transformation (CCT) diagram that was calculated using ThermoCalc where the M_s is calculated to be 350 K. Experimental results by means of dilatometry showed that the M_s of the as-received material is 290 K, which is significantly lower compared to the ThermoCalc calculations. The presence of α'_{BF} in the as-received material indicates that this morphology is the first α' morphology to form upon cooling as it is entirely surrounded by γ and its formation temperature must either be at or above RT as no (cryogenic) cooling step is applied after homogenisation. This also indicates that this phase can form upon ambient air cooling i.e. at relatively low cooling rates.

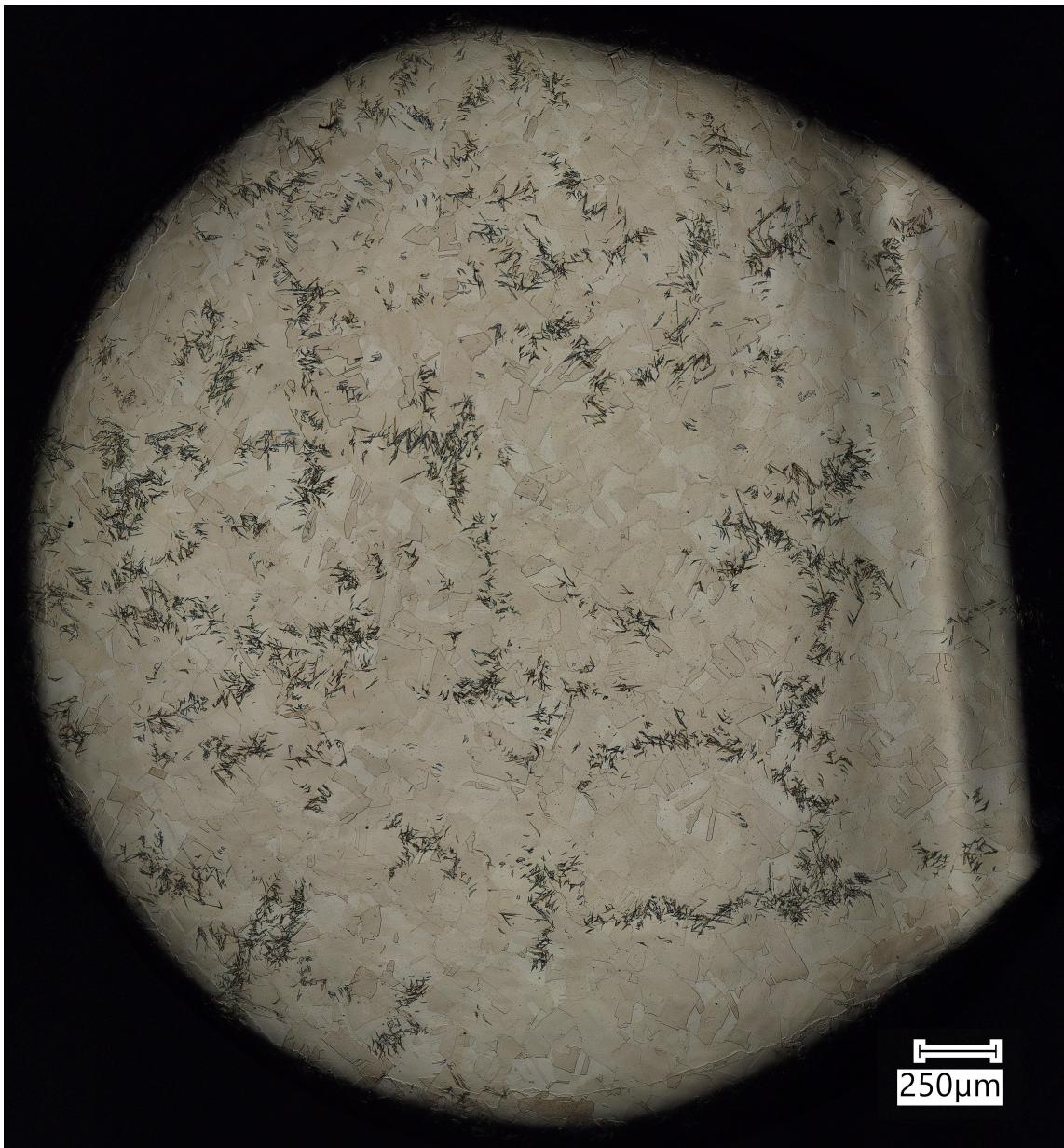


Figure 26: Cross section view of the dilatometry sample of the as-received material obtained by LOM

4.2 Oven and liquid nitrogen quenching experiments

As the 25Ni specimens were identical to those used by Breukelman et al. [55,56], initial experiments followed their established procedures. Samples were heated to 1273 K in an oven and subsequently quenched in LN for 300 seconds (which correspond to sample O_N300s and the temperature profile of Figure 22b). This treatment resulted in the presence of α'_{BF} within the material, as anticipated. However, it was observed that the γ phase had fully transformed into α' , with the morphology comprising both α'_{BF} and lenticular α' (Figure 27a). The smaller size of the lenticular α' compared to α'_{BF} indicated that the extent of undercooling was excessive, as lenticular α' forms at lower temperatures than α'_{BF} , as shown in Figure 1.

To investigate the morphology and substructure of α'_{BF} exclusively, a mixture of retained γ and α'_{BF} is desirable. This necessitates reducing the undercooling. Initially, the LN quenching time was reduced, but this did not result in observable changes in morphology. These observations led to the conclusion that LN quenching cooled the 25Ni sample down too far and too rapidly, preventing the exclusive formation of α'_{BF} .

Therefore, the LN quenching step was eliminated, and the microstructure was examined directly after removal from the oven. SEM and LOM observations revealed a mixed morphology of both γ and α'_{BF} (shown in Figure 27b), indicating that α'_{BF} formed before the quenching step upon ambient air cooling to RT. This suggests that α'_{BF} has a relatively high formation temperature above room temperature and can form at relatively low cooling rates.

Comparing these results with the α' morphology diagram by Umemoto et al. [5] (Figure 8), it can be inferred that the formation temperature of α'_{BF} is between approximately 300-373 K. If this is correct, cooling rates similar to air cooling would suffice to induce the $\gamma \rightarrow \alpha'_{BF}$ transformation.

It was found that, upon cooling, the heating elements were turned off and the oven did not apply any active cooling. As the oven was well insulated, this meant that the cooling rate was much lower and non-linear. As can be seen in Figure 23, the oven took between 7-8 hours to reach a temperature of approximately 473 K instead of the 4 hours that was applied within the oven settings to reach RT. The oven alone could thus not follow the required cooling rate in order to form α' and the sample was thus taken out of the oven to cool upon an aluminium plate. It was also not possible to in-situ observe the sample temperature during the oven experiments. Thus, dilatometry was considered instead of oven heating/cooling combined with ambient air cooling.

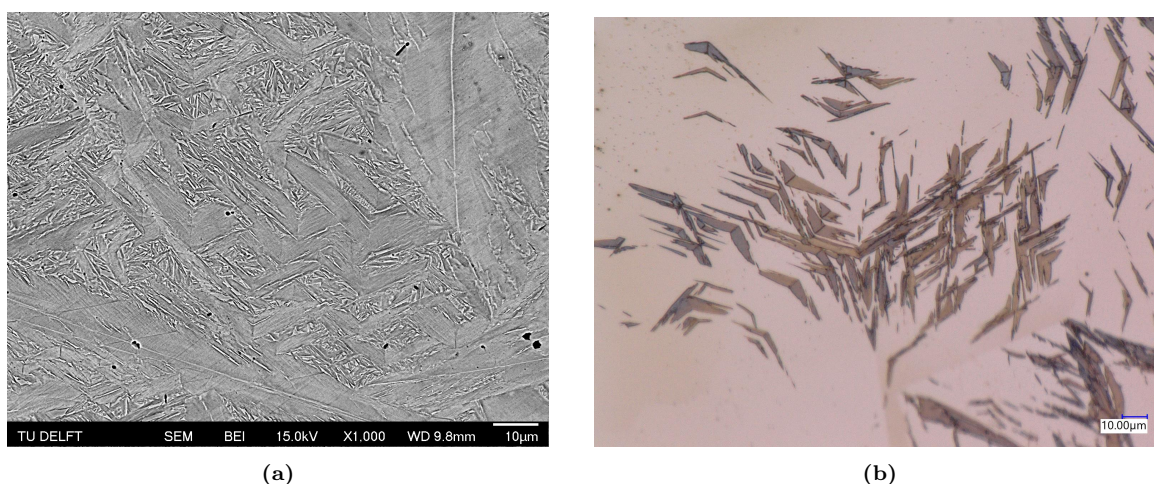
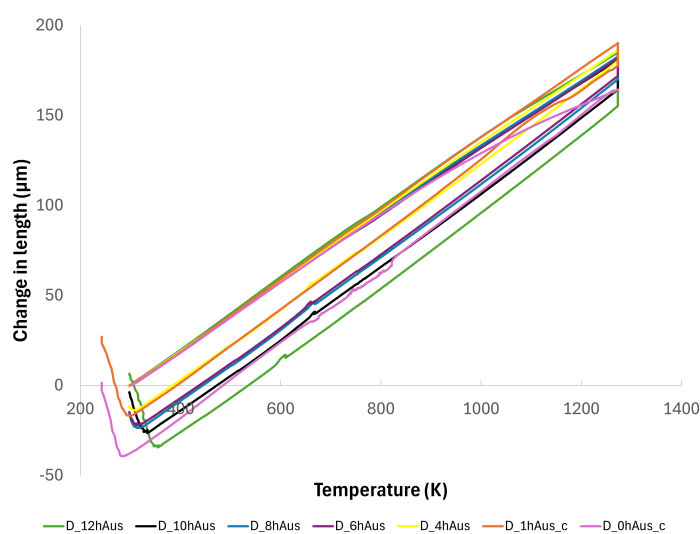


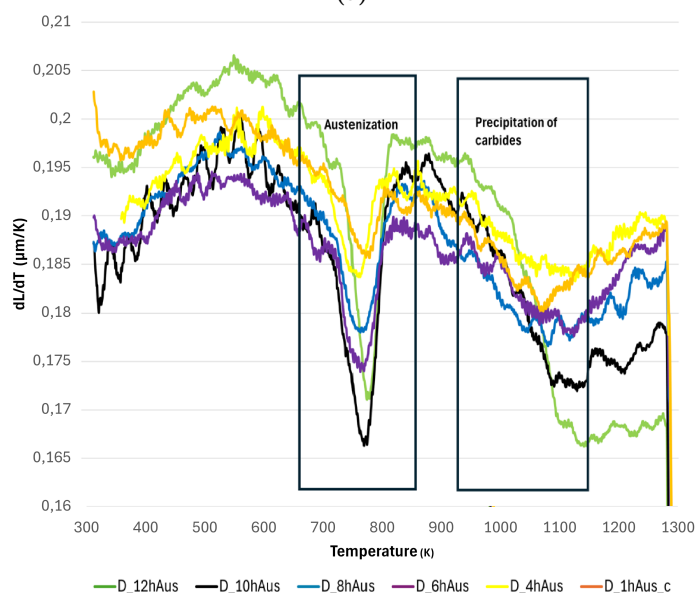
Figure 27: (a) SEM image of sample O_N300s showing both the butterfly and lenticular martensite morphologies, (b) Optical microscopy image of sample O_NAC.N1 showing a microstructure comprised of austenite and butterfly martensite

4.3 Analysis of dilatometry and microstructure

The dilatometry curves from the quenching treatment, presented in Figure 28a, illustrate the behaviour of specimens held isothermally at 1273 K for varying durations (1, 4, 6, 8, 10, and 12 hours). The as-received material, a composite of γ and α' phases, would typically show the A_1 and A_3 transformation points clearly in the heating curve. However, the curve appears almost linear, obscuring these transformation temperatures. By differentiating the length changes measured during the dilatometry experiment with respect to temperature, the expansion rate per Kelvin can be plotted against temperature, as depicted in Figure 28b. This figure reveals two distinct changes in expansion rate: one occurring between approximately 673 K and 803 K (Region 1) and the second one occurring between approximately 923 K and 1083 K (Region 2). As shown in the phase diagram computed by ThermoCalc (Appendix B), the phases that are present at lower temperatures (like ferrite and cementite) start to transform to γ just above 673 K, and all phases are expected to dissolve into the austenite matrix above roughly 803 K, which aligns with the experimental observations of Region 1. Therefore, the A_1 and A_3 temperatures are identified at 673 K and 803 K, respectively. The change in expansion rate within Region 1 upon heating can thus be attributed to the phase transformation from α' to γ , which is consistent with the expected phase change within this temperature range.



(a)



(b)

Figure 28: (a) Full dilatometry curves of specimens held for varying durations (1, 4, 6, 8, 10, and 12 hours), (b) length change rate upon heating

The change in expansion rate observed in Region 2 during heating is primarily attributed to the precipitation of carbides, as evidenced by comparing Figures 29a and 29b, which represent the material state at the beginning and end of this temperature region, respectively. Carbide precipitates along the grain boundaries are clearly visible in Figure 29b whereas they are absent in Figure 29a. Energy-dispersive X-ray spectroscopy (EDS) measurements (which can not be used to accurately quantify carbon concentrations) indicated that these particles contained a relatively higher carbon content compared to the bulk, indicating the presence of carbides. This retardation in thermal expansion due to carbide precipitation is consistent with behaviour observed in other high-nickel alloys, such as Inconel, within the same temperature range [58].

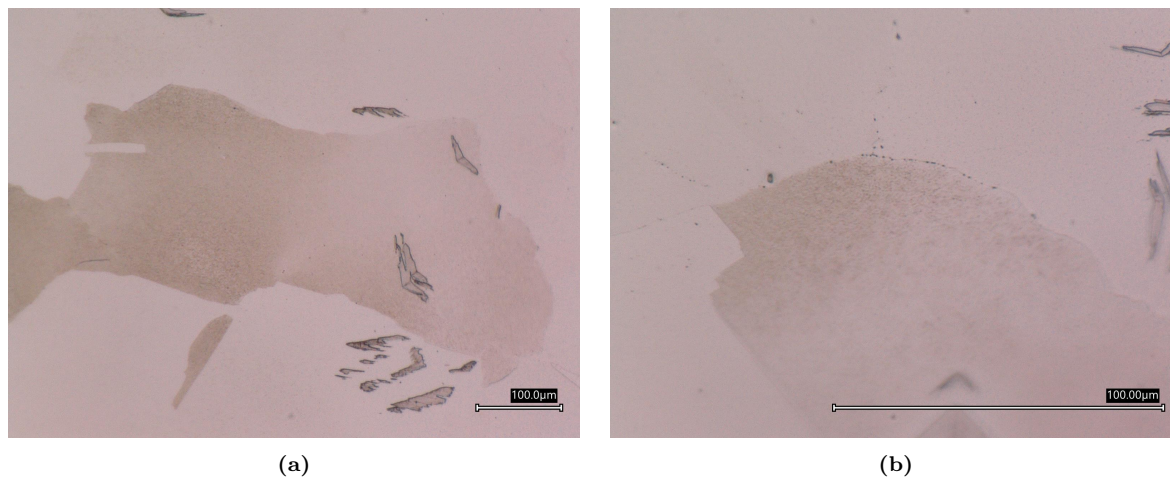


Figure 29: (a) LOM image of the surface of an As-received specimen heated up to 898 K (before Region 2) and cooled down to RT, (b) LOM image of the surface of an As-received specimen heated up to 1123 K (after Region 2) and cooled down to RT

During the isothermal holding period at t_A , the sample undergoes homogenisation and the growth of austenite grains is initiated. The mean grain sizes of specimens subjected to varying durations (1, 4, 6, 8, 10, and 12 hours) are presented in Table 7 for observation.

Table 7: Experimental results showing the average martensite fraction, martensite start temperature, prior austenite grain size and the observed martensite morphologies of the dilatometry specimens

Experimental results				
Sample name	average $f_{\alpha'}$ (area fraction in %)	M_s (K)	PAGS (μm)	α' morphologies
As-received	11 ± 2	293	89 ± 5	BF
D_0hAus_c	10 ± 2	299	96 ± 5	BF
D_4hAus	30 ± 2	311	99 ± 5	BF
D_6hAus	35 ± 2	317	107 ± 5	BF
D_8hAus	44 ± 2	323	117 ± 5	BF + lath
D_10hAus	49 ± 2	335	120 ± 5	BF + lath
D_12hAus	85 ± 2	358	unknown	BF + lath

Maki et al. [34] reported that M_s increases with prolonged austenising holding times, a phenomenon known as thermal stabilisation. Longer isothermal holding times result in an increase in PAGS (γ grain size measurements can be observed in Appendix C), which consequently increases the M_s of the alloy. This relationship is supported by the experimental data in Figure 30, where M_s is plotted against PAGS, showing a clear linear correlation within the observed grain size range. This linearity is however not expected to hold up for all grain sizes. As shown by Celada-Casero et al. [59], at very small PAGS (below $25 \mu\text{m}$) there is a significantly larger increase in M_s as a result of the increase in PAGS. Larger PAGS are thus more susceptible to the $\gamma \rightarrow \alpha'$ transformation. This higher susceptibility to the $\gamma \rightarrow \alpha'$ transformation of larger grains may be attributed to higher transformation strain accommodation in larger grains,

facilitated by a lower yield strength as described by the Hall-Petch strengthening mechanism [60].

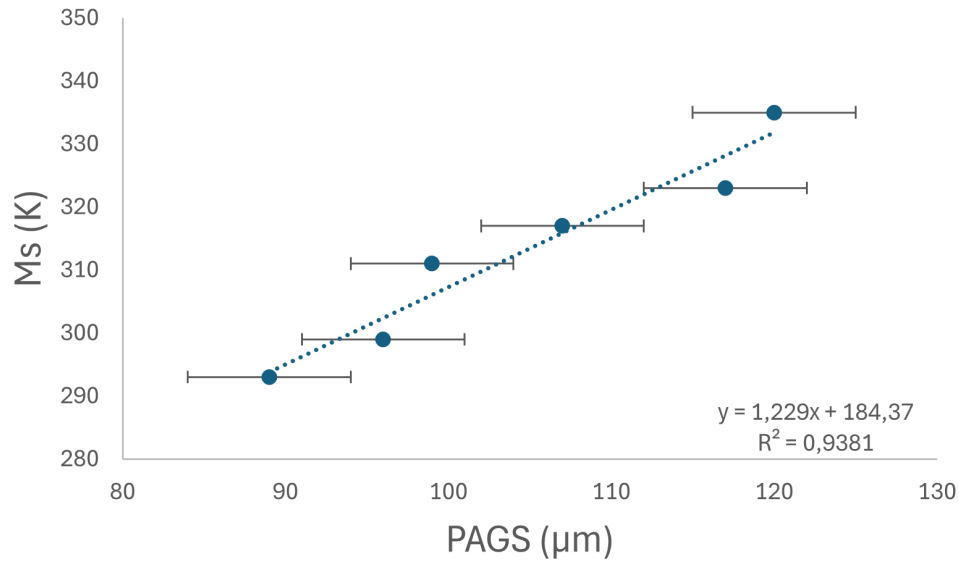


Figure 30: Graph showing the relation between PAGES and M_s

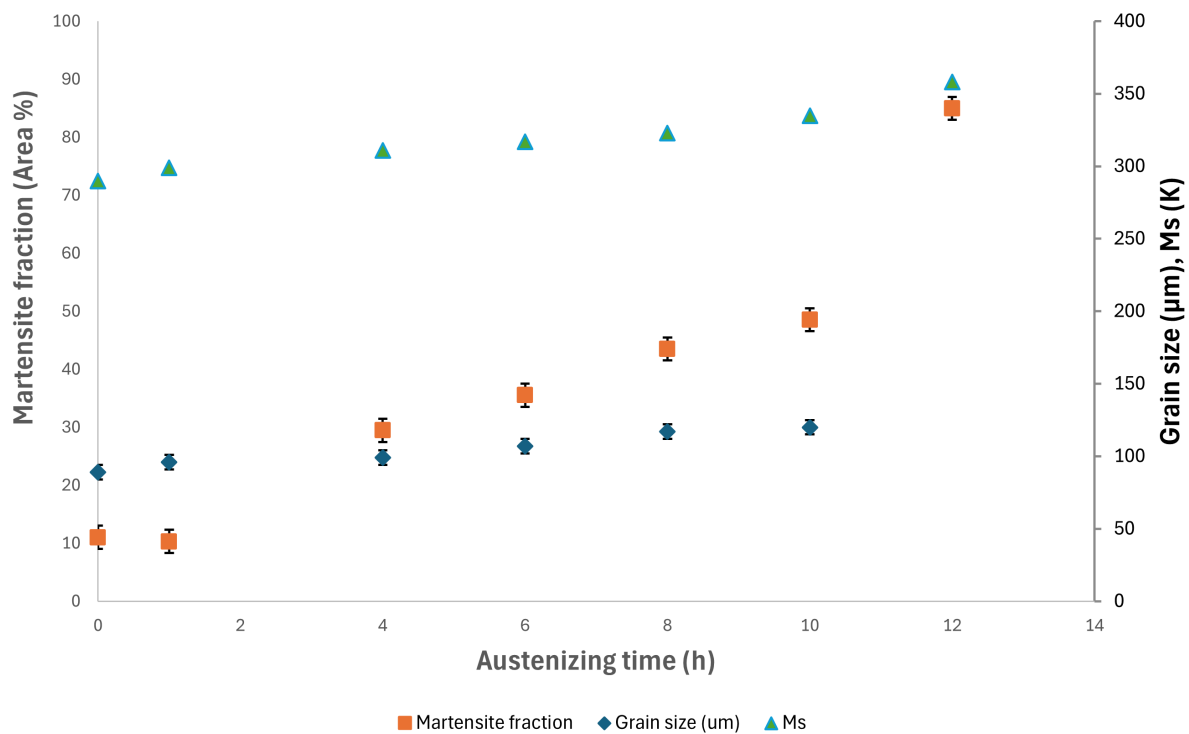


Figure 31: Graph showing the increase in γ grain size, M_s and α' fraction formed upon quenching as a function of the t_A

Following quenching, extended isothermal holding periods at t_A significantly influenced the transformation dynamics of the alloy. Experimental data shown in Table 7 and Figures 31 reveals an increase in M_s , PAGES and α' fraction ($f_{\alpha'}$) with increasing isothermal holding time at t_A . All curves (M_s , PAGES and $f_{\alpha'}$) display a similar trend, suggesting a close interrelationship. The experimental measurements used to calculate the M_s and $f_{\alpha'}$ can be found in Appendices D and E, respectively.

An increase in M_s involves an increase undercooling, thereby intensifying the driving force for martensitic transformation upon cooling to RT. This heightened driving force facilitates a greater degree of α' formed during the $\gamma \rightarrow \alpha'$ transformation. Indeed, examination of experimental data in Table 7 and

Figure 31 reveals an increase in both $f_{\alpha'}$ and M_s with increasing isothermal holding time at t_A . The increase in $f_{\alpha'}$ with increasing t_A is in good agreement with the findings from Gong et al. [18].

The $f_{\alpha'}$ formed upon quenching was found to be linearly proportional to the degree of undercooling below M_s as can be observed in Figure 32a. This linear relationship between undercooling and $f_{\alpha'}$ is commonly observed up to a transformation fraction of approximately 70-90% [61–63]. Beyond this point, the gradient decreases due to the increased driving force required to further increase the $f_{\alpha'}$ [63]. This linear behaviour between undercooling and $f_{\alpha'}$ shown in Figure 32a is in aligns well with findings of van Bohemen et al. [16] who used the koistinen-Marburger (KM) equation [64] with an added rate parameter (α_m) in order to predict $f_{\alpha'}$ formed in low alloy steel, shown in Equation 8.

$$f_{\alpha'} = 1 - \exp\{-\alpha_m(T_{KM} - T)\} \quad (8)$$

Where $f_{\alpha'}$ is the volume fraction α' and T_{KM} is the theoretical M_s .

Figure 32b shows the $f_{\alpha'}$ formed upon cooling of an alloy containing 14.9% Ni, 0.42% C and 0.7% Cr, calculated by the KM-equation (solid line) and experimental results (triangles). We observe that the $f_{\alpha'}$ is near-linear up to $\pm 65\%$ α' . The fact that the 25Ni alloy, used during this thesis, remains linear over a broader temperature range might be due to the increase in grain size which makes the $\gamma \rightarrow \alpha'$ transformation easier to occur.

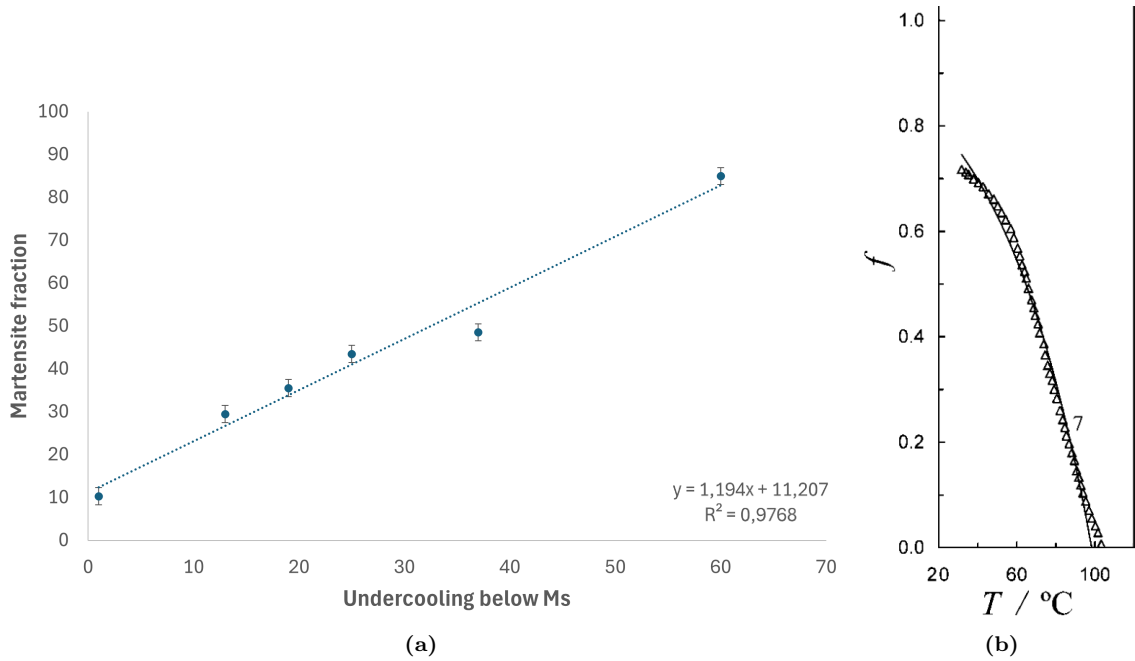


Figure 32: (a) Graph showing the relation between the degree of undercooling below M_s and the amount of α' that is formed upon cooling, (b) a graph showing the fraction of newly transformed α' as the temperature is decreased [16]

4.4 2D analysis of butterfly martensite

4.4.1 Morphologies & formation temperature

LOM images of the entire cross-section of the dilatometry samples (detailed in Appendix E) show that with t_A up to of 8 hours, the samples are comprised of a composite structure existing of γ and α'_{BF} phases. Subsequent increases in t_A (between 8-12 hours) induced the formation of lath-shaped α' morphology at the sample surface, as depicted in Figure 33a . These findings can also be seen in Table 7.

Over-austenisation of the material can inhibit the formation of α'_{BF} and cause lath-type α' to be the preferred morphology to form upon cooling to RT. If the thermal holding process at T_A is too long, the PAGS will become larger, increasing the M_s and thus increasing the amount of undercooling below M_s when cooled to RT, resulting in a morphology combined of lath and α'_{BF} instead purely butterfly morphology [31]. However, PAGS around the outer interface of the sample does not seem to be larger

compared to PAGES in the centre of the sample when comparing grain size measurements obtained through EBSD, found in Appendix C. Hence, this phenomenon is likely not the sole cause of the appearance of lath martensite near the outer interfaces. As if over-austenitisation was the sole cause of the transition from α'_{BF} to lath-shaped α' , the lath-shaped α' is expected to form homogeneously within the entire sample.

Empirical investigations conducted by Pak et al. [65] demonstrate that the $\gamma \rightarrow \alpha'$ transformation occurs at smaller undercooling near a free surface, attributable to reduced strain energy and hydrostatic pressure. Notably, the M_s increases by approximately $114 \text{ K} \pm 14 \text{ K}$ in an Fe-Ni alloy under such conditions. This phenomenon can explain the observed increase in the α' fraction near the sample's free surface and suggests that lath-shaped α' morphology exhibits a lower formation temperature within this alloy compared to the α'_{BF} morphology, which forms first below M_s .

It is most probable that the transition from α'_{BF} to lath-shaped α' at the outer edge of the sample is caused by a combination of a higher M_s due to an increase in PAGES at longer t_A and the increase in M_s at the outer edge of the sample due to the reduced strain energy and hydrostatic pressure resulting from the free surface effects.

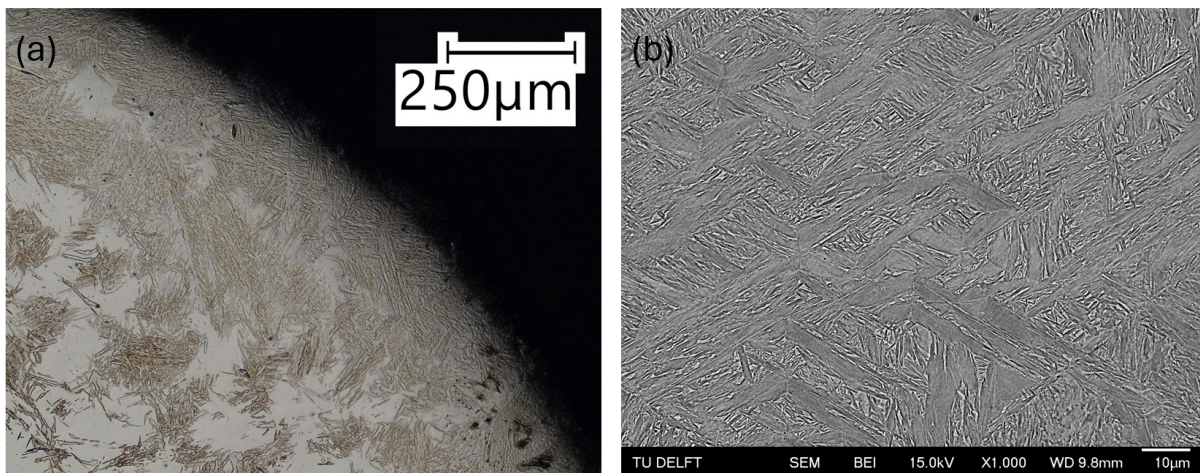


Figure 33: (a) Lath martensite forming near the edges of the $D_{10h}Aus$ sample, (b) small lenticular α' plates surrounding large α'_{BF} grains formed within the O_{N200s} sample

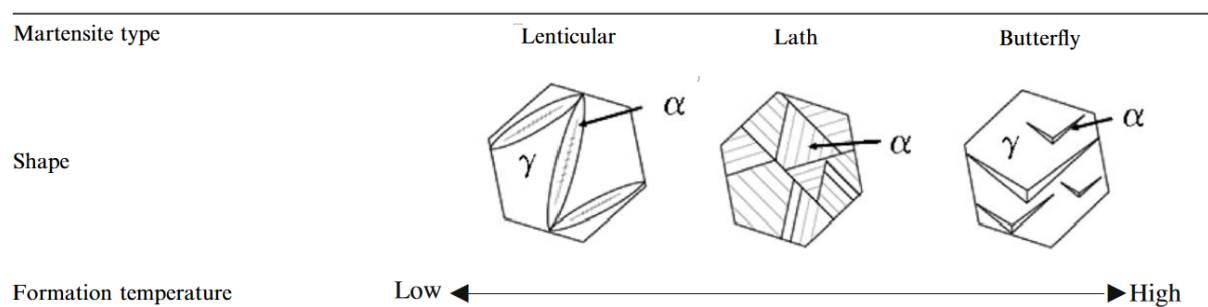


Figure 34: Order of α' morphology formation based on their formation temperature within the $25Ni$ alloy, based on image 1 by Sato et al. [1]

Upon subjecting the sample to further undercooling via full immersion in a bath of LN, the formation of lenticular α' morphology becomes apparent, as depicted in Figure 33b. Owing to the pre-existing presence of α'_{BF} within the sample, the laths are relatively small, their size constrained by the surrounding α'_{BF} grains.

Therefore, it is evident that, in this specific alloy, the α'_{BF} morphology initiates its formation below just M_s with the highest formation temperatures, succeeded by the emergence of lath-shaped α' upon subsequent cooling. Subsequently, at even lower formation temperatures, the formation of lenticular α' morphology ensues. Conventionally, a different formation order is expected as shown in Figure 1. Here lath α' has a higher formation temperature compared to α'_{BF} [1, 3, 5, 10, 40, 66, 67]. It is proposed that, for this specific 25Ni alloy coupled with the thermal treatment found in Figure 22c, α'_{BF} forms before lath α' . The schematic representation of the α' morphologies and their corresponding formation temperatures within the 25Ni alloy is schematically depicted in Figure 34. These findings are in good agreement with Hayashi et al. [8] who also found α'_{BF} to form prior lath α' . However, the first α' morphology morphology to form just below M_s is still not yet fully understood [8].

4.4.2 Butterfly morphology

Upon examination of Figure 35, it becomes apparent that all the various subtypes of α'_{BF} described by Umemoto et al. [10] (α'_{BF} grains with and without the presence of the midrib structure) and Gong et al. [6, 18] (α'_{BF} grains with one, two or without tails) are observable. A comparison between these two-dimensional α'_{BF} subtypes and the three-dimensional representation of α'_{BF} grains, depicted in Figure 9a, suggests the construction of a similar structure based on experimentally formed α'_{BF} grains. This is supported by the inclusion of slices A, B, and C from Figure 9a onto Figure 35. Consequently, these observations imply that all aforementioned subtypes form under identical conditions and may indeed constitute components of the same three-dimensional α'_{BF} structure.

The angle between the fully twinned midrib region of both wings is found to be $\pm 134^\circ$. This is in good agreement with literature, as the most common angles were observed to be situated between 120° and 140° [7, 10, 18].

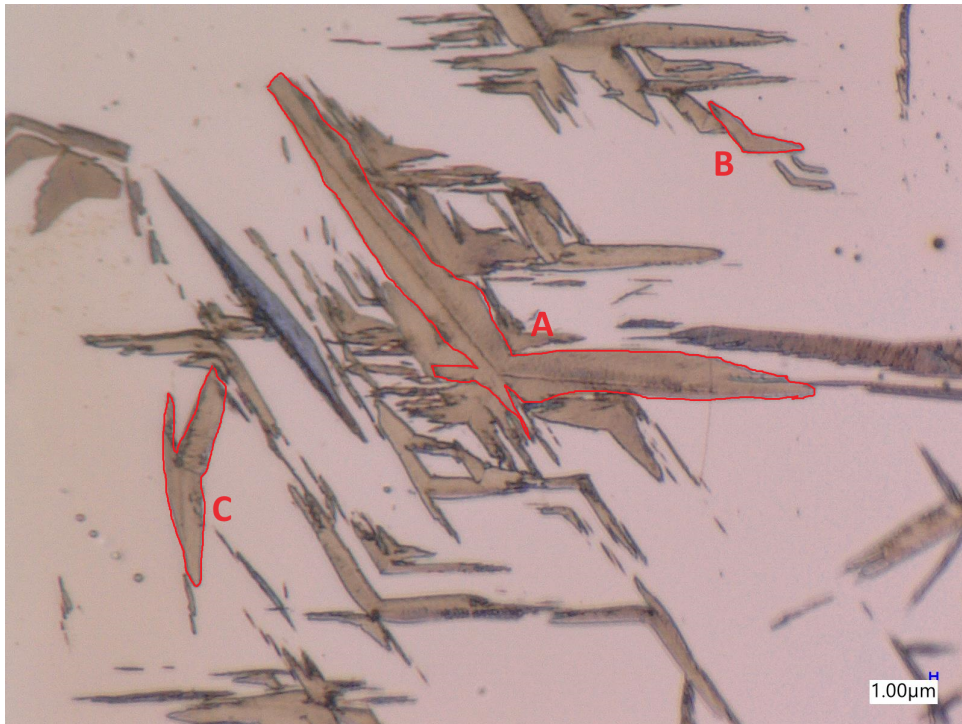


Figure 35: LOM image of the O-AC-1 sample showing three different two-dimensional α' subtypes

4.4.3 Butterfly substructures

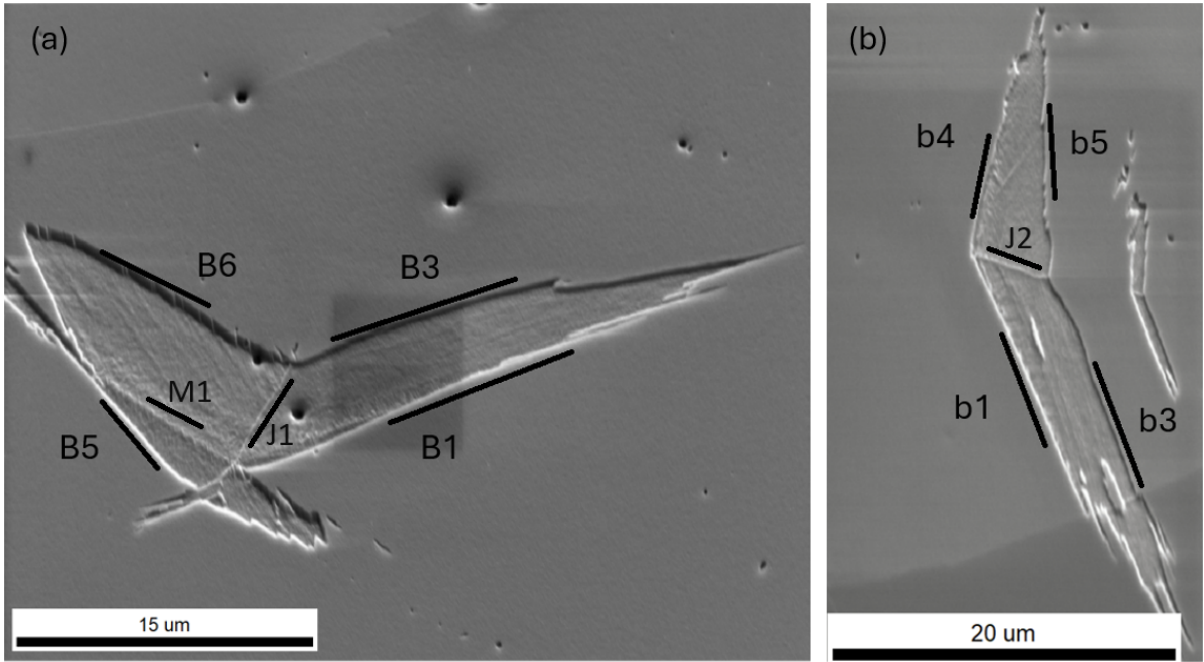


Figure 36: SEM images of the *D_8hAus* sample showing (a) Habit plane trace analysis of a large α_{BF} grain with a midrib structure in its left wing, (b) Habit plane trace analysis of a small and thin α_{BF} grain

Table 8: Results from habit plane trace analysis

Grain interface section	Habit planes			
	Calculated habit plane	Characteristic α' habit plane trace close parallel with the interface	Angle between observed and characteristic habit plane traces	Angle between observed and characteristic habit planes
B1	$(-5\ 7\ 11)_{\gamma}$	$(-3\ 10\ 15)_{\gamma}$	1°	11,59°
B3	$(-6\ 5\ 8)_{\gamma}$	$\{-5\ 5\ 7\}_{\gamma}$	1°	3,79°
B5	$(-2\ 9\ 2)_{\gamma}$	$(-2\ 5\ 2)_{\gamma}$	2°	12,05°
B6	$(5\ -14\ 1)_{\gamma}$	$(10\ -15\ 3)_{\gamma}$	3°	15,02°
b1	$(11\ 7\ -5)_{\gamma}$	$(5\ 2\ -2)_{\gamma}$	3°	10,00°
b3	$(1\ 3\ 2)_{\gamma}$	$(2\ 5\ 2)_{\gamma}$	1°	12,31°
b4	$(13\ 21\ 1)_{\gamma}$	$(2\ 5\ 2)_{\gamma}$	2°	20,50°
b5	$(-10\ -9\ -4)_{\gamma}$	$(-7\ -5\ -5)_{\gamma}$	1°	14,83°

The habit plane was initially determined using OIM software, which calculated the planes at which the γ/α'_{BF} boundaries are situated. These calculated habit planes are presented in the second column of Table 8. Consequently, it was concluded that the habit planes of the observed α'_{BF} grains correspond to these calculated habit planes, assuming planar interfaces and lattice periodicity.

Subsequently, the phase boundaries and substructures of multiple α'_{BF} grains were analysed through trace analysis. Well-known α' habit plane traces were projected onto the EBSD surface (as shown by the black lines in Figures 36a and 36b), resulting in plane traces that were close to parallel to the γ/α'_{BF} boundary traces that could be observed. The characteristic α' habit plane traces that closely matched the calculated habit traces, along with their deviations, are shown in columns 3 and 4 of Table 8. Characteristic habit planes corresponding to lenticular ($\{3\ 10\ 15\}_{\gamma}$), butterfly ($\{225\}_{\gamma}$), and lath ($\{557\}_{\gamma}$) α' were identified at the γ/α'_{BF} interface. The locations of these characteristic habit planes along the γ/α'_{BF} interfaces are depicted in Figures 36a and 36b. Table 8 indicates that all of these well-known

α' habit plane traces deviated by a maximum of 3° from the calculated habit plane trace on the sample surfaces, thereby confirming their close parallelism. Given this near parallelism of the habit plane traces, it is reasonable to assume that the habit planes lie close to these characteristic habit planes according to trace analysis.

However, this method of determining the characteristic habit plane is potentially inaccurate, as it relies on two-dimensional observations to infer three-dimensional structures. As shown in Table 8, while the habit traces of the observed and characteristic α' habit planes appear close to parallel, the planes themselves can deviate by up to 20.50° from each other (calculations can be found in Appendix F). This suggests that parallel plane traces do not necessarily imply near-parallel planes. Therefore, the assumption made during trace analysis, that parallel plane traces indicate parallel planes, cannot be validated.

To accurately determine the character of the habit plane, five degrees of freedom must be identified: three related to the misorientation between the two crystals (Δg) and two related to the habit plane normal (n), where $|\vec{n}|=1$. Conventional two-dimensional EBSD (2D-EBSD) can accurately obtain 4 out of these 5 degrees of freedom, as it only observes the trace of the habit plane on the sample surface, lacking depth resolution. As a result, the angle that the habit plane makes with the surface into the sample (β in Figure 37) cannot be determined. To more accurately ascertain the habit plane character of α'_{BF} , characterisation methods with higher depth resolution, such as Transmission Electron Microscopy (TEM), Transmission Kikuchi Diffraction (TKD), or 3D-EBSD, could be employed.

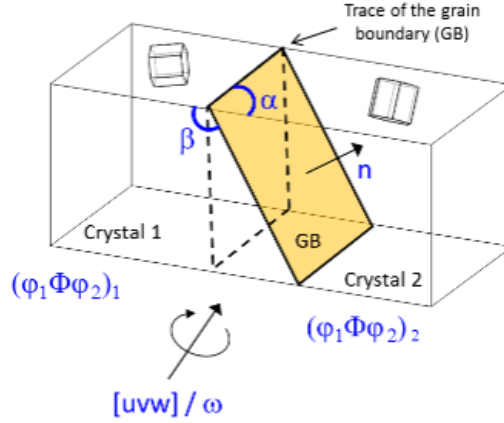


Figure 37: Schematic representation of a grain boundary trace at the surface of a sample in between two crystals and the angle that this boundary plane can have below the surface (angle β). [17]

Using the same trace analysis methodology, the midrib structure (M1 in 36a) was determined to be close to parallel to the $\{225\}_\gamma$ trace, while the junction planes (J1 and J2 in Figures 36a and 36b, respectively) were found to be close to parallel with the $\{100\}_\gamma$ trace. These findings are consistent with previous research.

4.4.4 Formation sites

The optical micrograph in Figure 38 reveals that the majority of α'_{BF} grains are located away from the grain boundaries, predominantly near the centre of the parent γ grain. This observation aligns well with the Ansell model, which is based on the Hall-Petch strengthening mechanism. According to this model, the interior of γ grains is softer compared to the grain boundary regions. Consequently, the γ grain exhibits greater strength near the boundaries, resulting in higher resistance to plastic deformation and increased strain energy associated with the $\gamma \rightarrow \alpha'$ transformation. As a result, the initial formation of α' predominantly occurs near the centre of the γ grain where the initial $\gamma \rightarrow \alpha'$ transformation is more energetically favourable. [68]

The inner region of the γ grain is not the only formation site for α'_{BF} as Figure 38 also shows some α'_{BF} formation at the γ grain boundary. Figure 39, which is a zoomed in image of the lower highlighted γ grain boundary of Figure 38, shows α'_{BF} grains that have nucleated near this γ grain boundary. As

a result of the proximity to this grain boundary, one of the wings has aligned itself to this boundary whereas the other wing grew into the γ grain. It can also be observed that the wing that grew into the γ is much shorter compared to the wing that is aligned with the γ grain boundary. This observation coincide well with previous findings of Hayashi et al. [8], who schematically drew the formation of α'_{BF} near γ grain boundaries which can be seen in Figure 12a. Formation of α'_{BF} near γ grain boundaries was observed less frequently compared to the inner regions of the γ grain. Hence, γ grain boundaries are not thought to be preferred formation sites for α'_{BF} . It is however interesting that the local density of α'_{BF} near γ grain boundaries is very high. As can be observed in Figure 39, many small α'_{BF} are packed close together with one wing aligning with the grain boundary whilst the other growth into the γ . It is not yet known why the wing growing into the γ can be so short or why the density of α'_{BF} is locally so high near γ grain boundaries. More research is thus required in order to get more insight about the nucleation and growth of α'_{BF} wings near these γ grain boundaries. Determining a habit plane from the inner interface of this grain was not possible as the interfaces of the aligned wing is curved and irregular, meaning that the interface is not located on a single plane. Upon observation of Figures 38 and 39 the statement made by Hayashi et al. [8] that α'_{BF} formed near γ grain boundaries are more irregular compared tot α'_{BF} formed within the bulk of the γ grain seems to be accurate.

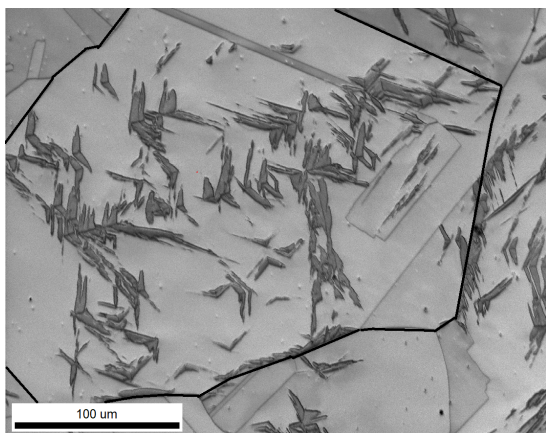


Figure 38: SEM image quality map of the D-8hAus sample

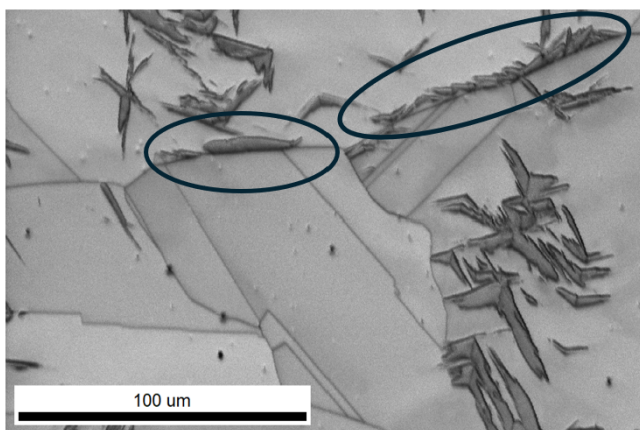


Figure 39: Butterfly grains that has aligned with the γ grain boundary of the D-8hAus sample, resulting in an irregular shape

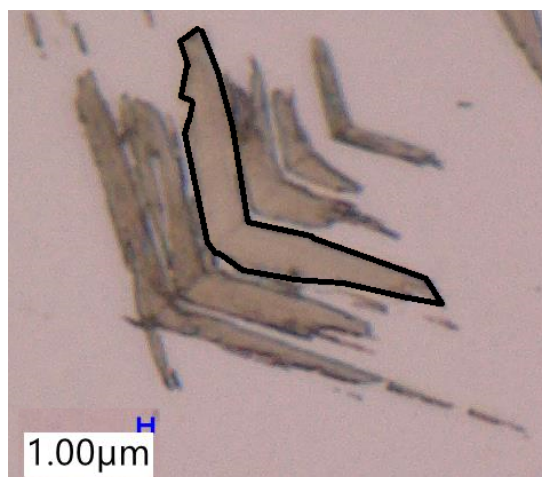


Figure 40: LOM image of the O-AC-1 sample showing catalytic α'_{BF} formation

4.4.5 Catalytic formation

Upon examining the sample surface, it was frequently observed that α'_{BF} grains formed in close proximity to each other, often aligning in straight columns, as illustrated in Figure 40. This pattern of α'_{BF} is thought to be caused by catalytic formation, with the grains typically situated within $2 \mu\text{m}$ of the concave and convex regions of adjacent α'_{BF} grains which is consistent with the findings of Chen et al. [9].

In Figure 40, the grain outlined by black lines is presumed to be the earliest formed α'_{BF} grain, based on its relatively straight and planar interfaces compared to the surrounding α'_{BF} grains. The absence of significant irregularities and the comparatively larger size of this grain suggest that it did not form under strain-induced conditions. This aligns with previous studies showing that increased strain leads to a rise in interface irregularities at the γ/α'_{BF} boundaries [47, 50, 69], as well as finer grain sizes [70, 71].

Assuming this highlighted grain represents the initial α'_{BF} grain, further observations indicate that secondary formed α'_{BF} grains at the concavity regions of the primary grain are smaller than those forming at its convexity which is also in agreement with the findings reported by Chen et al. [9].

4.4.6 Butterfly martensite grain orientations

Figure 41 shows an EBSD inverse pole figure (IPF) map. The colours correspond to a specific crystallographic orientation parallel to the normal direction (ND) of the sample surface. Multiple γ grains (numbered 1-5 withing Figure 41) can be observed which all contain multiple α'_{BF} grain within them. The crystallographic directions of all the α'_{BF} grains within γ grains 1-5 can be observed in Table 9. From both the IPF image and table it can be observed that the α'_{BF} grains have a preferred orientation, as only a few crystallographic variants are observed within each γ grain. The relationship between the crystallographic orientations of the two α'_{BF} wings is not yet known.

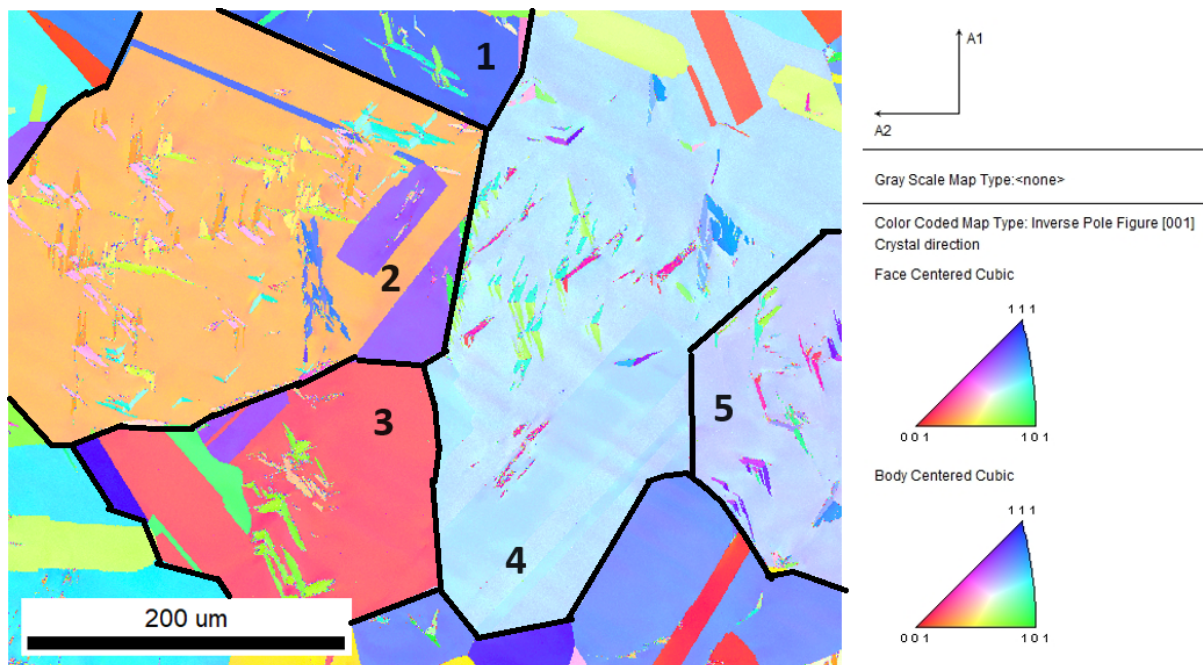


Figure 41: IPF map of the *D_8hAus* sample parallel to $[001]$ or the direction normal to the sample surface (ND)

Table 9: γ and α' crystallographic grain orientations

γ grain	γ orientation ($//$ ND)	α' orientation ($//$ ND)
1	$[9\ 7\ 11]$ (dark blue)	$[6\ 1\ 9]$ (green) & $[3\ 1\ 3]$ (blue)
2	$[4\ 1\ 11]$ (light orange)	$[6\ 1\ 22]$ (orange) & $[2\ 1\ 4]$ (pink) $[5\ 1\ 11]$ (light orange) & $[1\ 0\ 2]$ (yellow) $[3\ 1\ 3]$ (blue) & $[7\ 3\ 9]$ (light blue)
3	$[2\ 1\ 9]$ (red)	$[6\ 1\ 9]$ (green) & $[13\ 1\ 18]$ (dark green)
4	$[7\ 3\ 9]$ (light blue)	$[3\ 1\ 3]$ (blue) & $[6\ 1\ 9]$ (green) $[7\ 6\ 17]$ (magenta) & $[2\ 2\ 3]$ (purple) $[2\ 1\ 1]$ (light orange) & $[1\ 1\ 4]$ (pink)
5	$[2\ 1\ 3]$ (blue-grey)	$[2\ 1\ 1]$ (light orange) & $[1\ 1\ 4]$ (pink) $[7\ 6\ 1]$ (magenta) & $[2\ 2\ 3]$ (purple) $[3\ 1\ 3]$ (blue) & $[6\ 1\ 9]$ (green)

4.4.7 Orientation relationships

In order to determine the ORs that are present at the γ/α' interfaces, an OR map is made based on the axis-angle pairs. Within this map magenta, green and yellow lines indicate the OR at the γ/α' interfaces with K-S, N-W and G-T, respectively. Examination of Figures 42a and 42b reveals that the γ/α' interfaces exhibit a combination of N-W and G-T ORs. However, the locations of these various ORs are inconsistent across the observed α'_{BF} grains.

In Figure 42a, four grains are highlighted. Grain 1 shows both the inner and outer interfaces exhibiting a combination of N-W and G-T ORs. Grain 2 has an outer interface displaying a pure G-T OR, while the inner interface consists purely of N-W OR. Both interfaces of grain 3 exhibit G-T OR. The α'_{BF} grains within circle 4 show inner interfaces with a combination of G-T and N-W ORs, whereas the outer interface presents a combination of G-T and K-S ORs. The ORs between the left and right α'_{BF} wings in Figure 42a appear nearly identical, which is not always the case as illustrated in Figure 42b. In this figure, the left wing primarily exhibits G-T OR, while the right wing contains mainly N-W OR at the inner interface and a combination of N-W and G-T ORs at the outer interface.

Notably, grains 2, 3, 4 in Figure 42a and the grain in Figure 42b indicate that the outer interfaces, which are considered to be the nucleation sides of the α'_{BF} morphology without midrib structures or tails, predominantly exhibit G-T OR. Conversely, the inner interfaces of these grains, along with both interfaces present in grain 1, contain a mix of G-T and N-W ORs, suggesting a transition towards N-W upon growth. This transition could be attributed to the deformation of the surrounding γ and the inheritance of dislocations from the surrounding γ into the α' [1,40].

The above mentioned findings contrast with those of Sato et al. [1] and Jafarian et al. [41]. Both found the G-T OR exclusively at the inner interface, while the outer interfaces were found to be solely K-S OR and a combination of K-S and G-T ORs by Jafarian et al. and Sato et al., respectively.

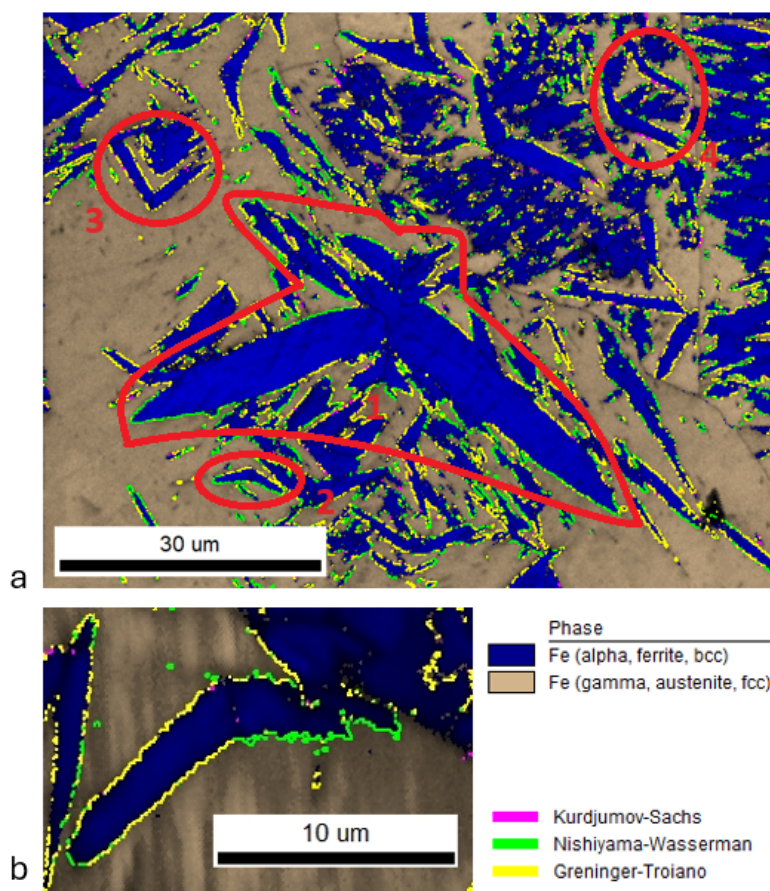


Figure 42: OR maps of the As-received sample where (a) and (b) show the various ORs that are present at the γ/α' interfaces

4.4.8 Butterfly martensite growth

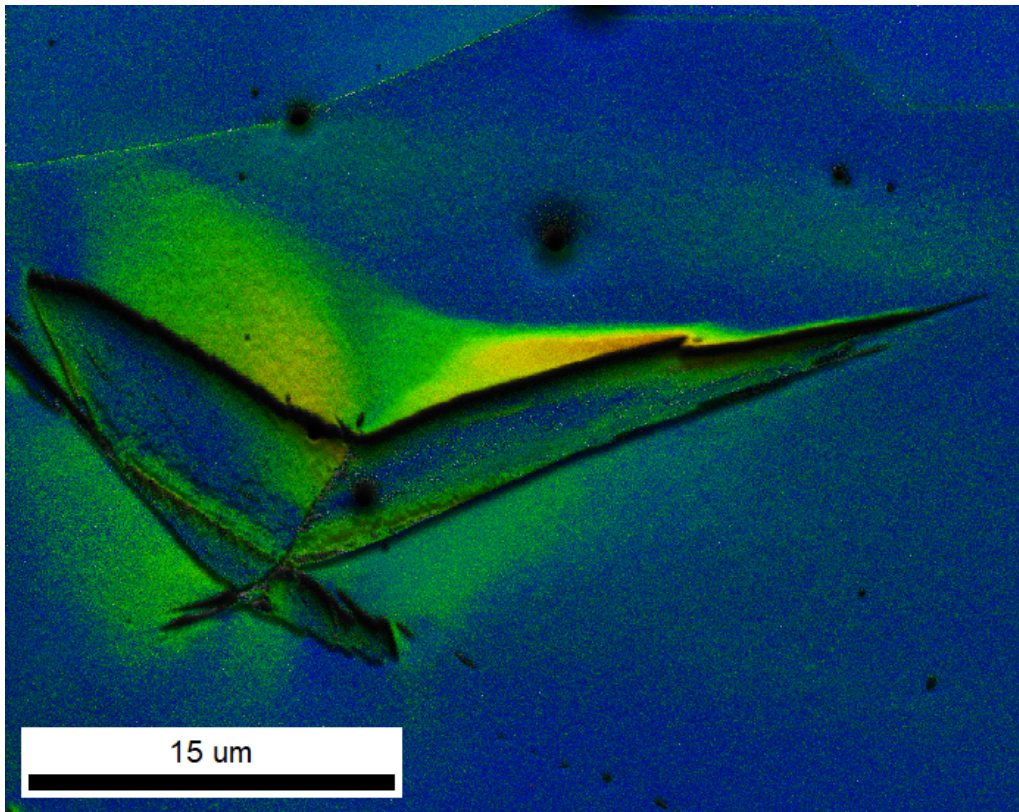


Figure 43: *Local orientation deviation map of a large α'_{BF} within the $D_{8h}Aus$ sample*

Figure 43 portrays a orientation deviation map of a α'_{BF} grain. As can be seen, the largest amount of deviation can be found on the upper side of the wings. This agrees well with the α'_{BF} growth theory of Gong et al. [6], which stated that the α'_{BF} grain initiates at a transformation twin (which in this case is the midrib within the left wing and the outer interface of the right hand wing), followed by unidirectional growth upwards of this structure and lastly growing at the lower part of the transformation twin. The growth of a α'_{BF} grain is schematically represented in Figure 11a. As α'_{BF} grows in its width direction, the surrounding γ is deformed [1, 6] resulting in deformation along the inner γ/α' interface of the α'_{BF} grain. If the growth theory of Gong et al. is assumed to be correct, the deformation should be located mainly at the inner interface. The outer interface is also expected to contain some deformation as there is small growth below the transformation twin. This orientation deviation map indeed confirms this and it can thus be concluded that the growth theory of Gong et al. is presumed to be correct as growth initiates first in upwards of the transformation twins and secondary below it. However, more research is still required into the growth kinetics of α'_{BF} in order to map its three dimensional growth and get insight in why this α' morphology stops growing in both its length and width direction, giving it its characteristic shape.

4.5 3D analysis of butterfly martensite

All three dimensional analyses were performed using the As-received material. These types of samples were chosen for this purpose as they contained the lowest fraction of α' , meaning that these samples had the highest possibility of observing a fully formed α'_{BF} grain that grew without restriction from other α' plates and is surrounded by γ .

4.5.1 Serial sectioning

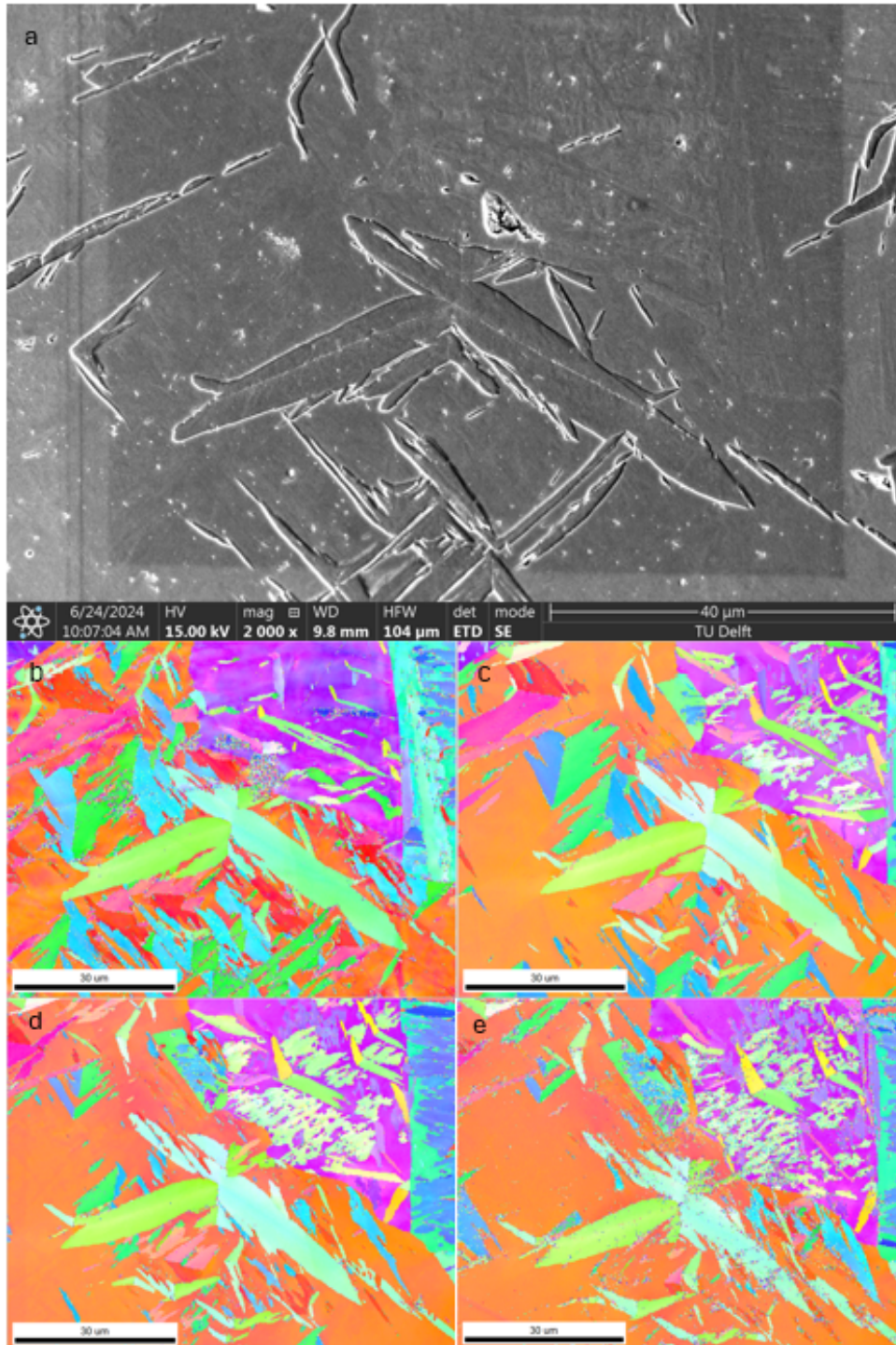


Figure 44: Images of serial sectioning of the As-received sample showing (a) SEM image of the initial surface before serial sectioning, (b)-(e) IPF maps of the surface after removal of approximately 1-3 μ m with respect to the previous section.

Figure 44 shows α'_{BF} grains surrounded by retained γ and the morphology change that occurs upon serial sectioning (44b-e). Figure 44.a shows the initial morphology before mechanical polishing. However, after the first polishing step (Figure 44b), thick and irregular α'_{BF} grains emerge that were not present initially. As additional slices are produced through mechanical polishing, these thick grains tend to disappear after the third slice and a lenticular α' morphology appears. Given that each slice is approximately 1-3 μm thick, these butterfly grains only penetrate a few micrometers into the sample surface. It is plausible that these irregular butterfly grains are formed due to stress/strain induced by mechanical polishing, which can affect the surface up to 5-50 μm deep [10]. Comparing this newly formed irregular α'_{BF} morphology to that of α'_{BF} formed upon mechanical polishing observed by Umemoto et al. (Figure 15), it is evident that they are identical, both exhibiting irregular inner and outer interfaces, lacking a twinned midrib structure, and having a thickness of around 10 μm . Therefore, it can be reasonable to assume that these newly formed α'_{BF} grains are strain-induced by the mechanical polishing of the sample surface. It is rare to observe a steel alloy that is so sensitive to strain induced α' formation. The high nickel concentration within the 25Ni alloy could be responsible for this behaviour, this is however not known for sure as Ryoo et al. [72] observed that the fraction of strain induced α' that formed upon cooling to RT decreased with increasing Ni content. More research is required on the topic of α'_{BF} formed upon mechanical polishing and why multiple α morphologies (butterfly and lenticular) form under these strain condition.

4.5.2 3D EBSD

The 3D-EBSD volume that was extracted from the surface of the initial 25Ni sample (shown in Figure 45a) was chosen as the surface morphology of the α'_{BF} that could be observed showed a double tailed morphology with the midrib structure that was present in both wings at the surface if this region, as can be seen in Figure 24a. This morphology indicated that this two-dimensional slice of the three-dimensional α'_{BF} structure was of one of the extremities. Thus there was a good chance that, if this grain was situated at an angle perpendicular to the sample surface, that a 3D image could be made of an entire α'_{BF} grain.

Four distinct α'_{BF} grains were found within the extracted volume, two of which (called α'_{BF}^1 and α'_{BF}^2) will be highlighted and discussed separately below. 3D images of the other α'_{BF} grains (called α'_{BF}^3 and α'_{BF}^4) can be found in Appendix G.

Analysis of grain α'_{BF}^1 :

The α'_{BF} grain that was observed at the surface of the As-received 25Ni sample, named α'_{BF}^1 , was however not situated at an angle perpendicular to the sample surface, as upon 3D analysis it was found that this grain was at an angle of approximately 45° with respect to the sample surface. Because of this, this large α'_{BF} grain emerged out of the side of the observed volume, as shown in Figure 45a and only a fraction of the α'_{BF} grain could be analysed. A 3D reconstruction of this grain can be seen in Figures 45b-e. When observing the boundary cells of this grain, which are shown in Figure 46, it can be seen that the junction plane, which is situated along the $\{100\}_\gamma$ plane, is completely straight and planar. The same can be concluded about both in inner and outer interfaces of this grain. The junction plane does however not seem to be completely continuous as the junction plane in between the tails is shifted towards the side, resulting in two distinct junction planes within the grain as can be seen highlighted by the arrows in Figure 46. It can thus be concluded that the junction plane does not per definition have to be one continuous feature as initially thought.

To be able to determine the actual dimensions of the butterfly wing within the angled grain, a slice has been made perpendicular to the opening axis, shown in Figure 47. The actual length of the wings could not be determined as only part of the wings are situated within the observed volume. The wing thickness and tail dimensions could be determined and the dimensions can be found in Table 10.

Upon examination of Figures 45a and 47a comparison can be made between the apparent and true wing angle if this α'_{BF} grain. The apparent wing angle is the wing angle that is observed at the surface of a sample and does not account for the angle that this grain make with respect to the observation surface. The true wing angle is found when the observation surface is perpendicular to the opening axis of the grain as in Figure 47. The apparent wing angle is found to be 105° whereas, as the observation plane is tilted by 45° , the true wing angle is found to be 125° . The angle that the α'_{BF} grain makes within the sample with respect to the surface of the sample thus results in a large discrepancy between

the apparent and true wing of the α'_{BF} grain.

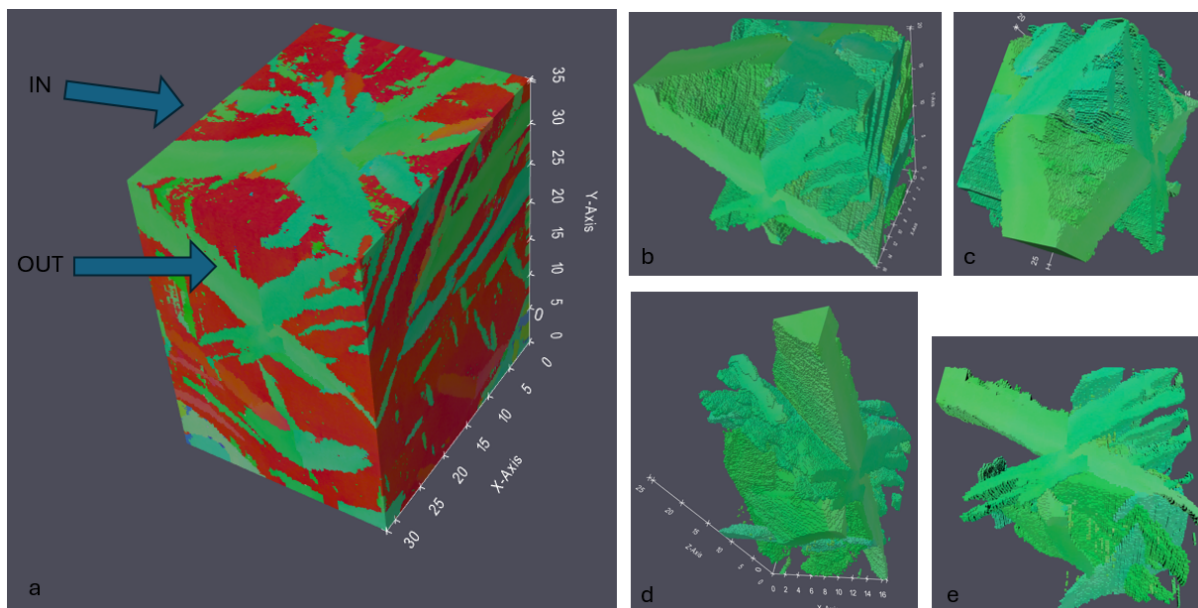


Figure 45: (a) Three dimensional IPF surface image of the entire 3D-EBSD volume showing the α'_{BF}^1 found at the surface of the original sample going in and out of the sample at an angle of 45° , (b)-(e) the α'_{BF}^1 grain with the γ removed at various angles.

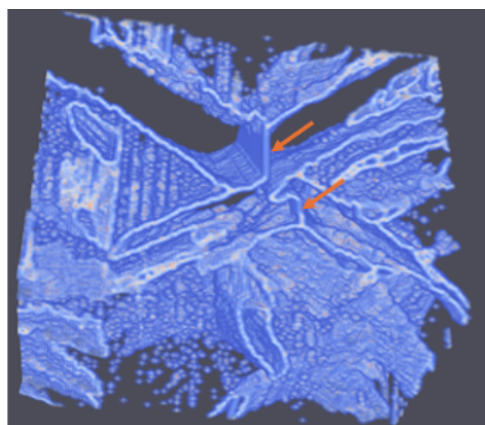


Figure 46: Three dimensional view of the boundary cells, of the α'_{BF}^1 grain within the volume, between the γ and α' as well as boundaries within the α'_{BF}^1 grain itself.

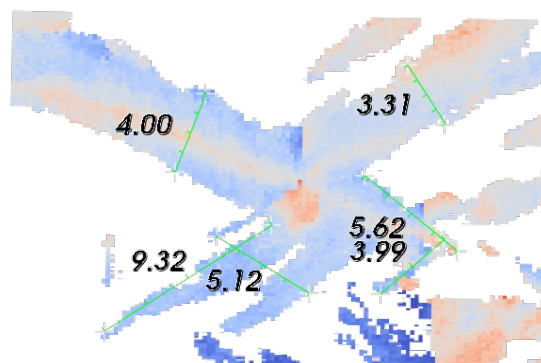


Figure 47: A slice taken of the α'_{BF}^1 grain at 45° in such a way that the slice is perpendicular to the opening axis.

Table 10: Double tailed grain dimensions

α' grain	Wing length (L/R)	Wing thickness (L/R)	Tail length (L/R)	Tail thickness (L/R)
Double tailed at 45° angle	unknown	$4.0 \mu\text{m}/3.3 \mu\text{m}$	$9.3 \mu\text{m}/5.6 \mu\text{m}$	$5.1 \mu\text{m}/4.0 \mu\text{m}$

Analysis of grain α'_{BF}^2 :

A second α'_{BF} grain, named α'_{BF}^2 , was found on the surface of the xy-plane in Figure 45a. Once the surrounding phases and grain were filtered out a clear butterfly shape appeared as can be observed in Figures 48a-d. This reconstructed α'_{BF} grain is thought to be part of the tip of the full three-dimensional α'_{BF} grain structure as only a single tail can be observed. This tail can be seen spanning along the entire length of the α'_{BF} grain. The tail is quite irregular as the length can be seen fluctuating along the length of the grain in Figure 48d. The fact that the tail extends all the way towards the tip goes against

three-dimensional descriptions of α'_{BF} made by Gong et al. [6] and Umemoto et al. [10] who both state that the tails disappear near the tip of the grain. As only one grain has been observed with 3D-EBSD that shows the tip of a α'_{BF} grain, it cannot be concluded that the tail will always span the entire length of the α'_{BF} grain. What can be concluded is that the tails do not have to completely disappear near the tip of the grain as previously thought. More research is required into the three-dimensional evolution of the butterfly tails along the longitudinal direction of the grain to be able to tell if the observations made here were a rare occurrence or if this occurs more frequently. Doing so could change the perception of the three-dimensional morphology of α'_{BF} as we know it today.

Table 11 shows the dimensions of the α'_{BF}^2 grain slices shown in Figure 49a-d. It can be seen that at slice $z=0 \mu\text{m}$, the length of the right wing is shorter compared to the left wing. However, going further towards the tip ($z=7.5 \mu\text{m}$), the right wing is larger compared to the left wing. The left wing shortens at an angle of 45° parallel to the surface whilst the length of the right wing shrinks at an angle of approximately 56° . Figure 50 shows the α'_{BF}^2 together with the surrounding α' grains within the volume (γ is filtered out). The non-symmetric wings of α'_{BF}^2 could be caused by impingement during growth from grains 2 and 3 shown in Figures 50a-c. These grains could either have formed prior or simultaneously with respect to α'_{BF}^2 . Grain 2, found in Figure 50 is also α'_{BF} , whereas no conclusions can be made about the α' morphology of grain 3 as it is cut off by the observed volume. There is a good chance that this grain 3 is also a α'_{BF} grain as it follows a similar shape as can be observed in Figure 50c and the volume should only contain a mixed morphology of both γ and α'_{BF} (ignoring strain assisted α' formed upon polishing which could possibly also form during the FIB milling procedure). Figure 50c also shows that the tips of both α'_{BF}^2 and grain 2 (and possibly grain 3) are located at the same point, which is highlighted by a circle surrounding this area. This can indicate that this point was an α' nucleation point and that one α'_{BF} nucleation point can result in multiple α'_{BF} grains growing in multiple directions outward from this point.

The apparent wing angle of this grain is identical to the true wing angle of this grain at 140° as this grain is angled perpendicular to its opening axis with respect to the observation surface. The true wing angles of both α'_{BF}^1 and α'_{BF}^2 are in good agreement with Umemoto et al. [7, 10] and Gong et al. [18] as they lie within the range of the most commonly observed α'_{BF} wing angles (120° - 140°).

All the γ/α' interfaces as well as the junction plane appear to be straight and planar on observing the boundary maps in Figures 51a-b. This indicates that this grain grew freely without being inhibited by the surrounding α' or large precipitates and that the surrounding γ was undeformed.

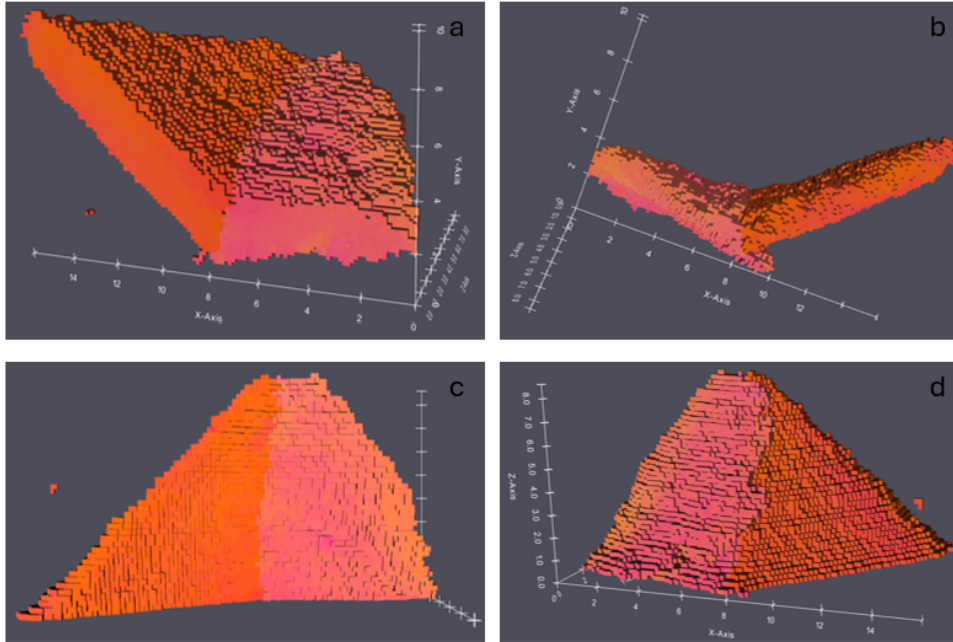


Figure 48: Images (a)-(d) showing the three dimensional morphology of the α'_{BF}^2 grain at various angles.

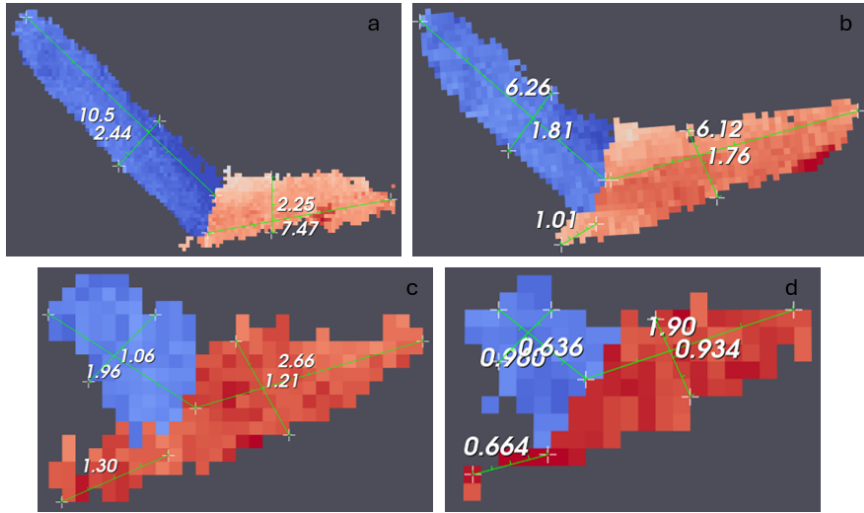


Figure 49: Two dimensional slices of the α'_{BF^2} grain together with their dimensions taken at (a) $z=0 \mu\text{m}$, (b) $z=3.5 \mu\text{m}$, (c) $z=7.5 \mu\text{m}$ and (d) $z=8.1 \mu\text{m}$

Table 11: Single tailed grain dimensions

α' grain	Wing length (L/R)	Wing thickness (L/R)	Tail length	Tail thickness
Slice 1 ($z=0 \mu\text{m}$) (Figure 49a)	10.5 μm /7.5 μm	2.4 μm /2.3 μm	no tail	no tail
Slice 2 ($z=3.5 \mu\text{m}$) (Figure 49b)	6.3 μm /6.1 μm	1.8 μm /1.8 μm	1.0 μm	0.8 μm
Slice 3 ($z=7.5 \mu\text{m}$) (Figure 49c)	2.0 μm /2.7 μm	1.1 μm /1.2 μm	1.3 μm	0.75 μm
Slice 4 ($z=8.1 \mu\text{m}$) (Figure 49d)	1.0 μm /1.9 μm	0.6 μm /0.9 μm	0.7 μm	0.25 μm

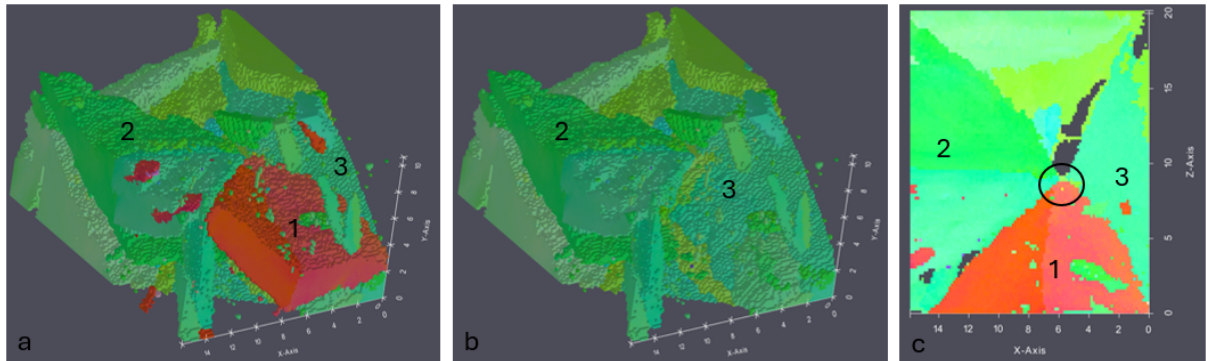


Figure 50: Three dimensional figures the α' phase showing: (a) α'_{BF^2} , which has been given the number 1 surrounded by two other α' grains named 2, which is also α'_{BF} and 3, (b) the same volume without the α'_{BF^2} grain and (c) a top view of all three α' grains

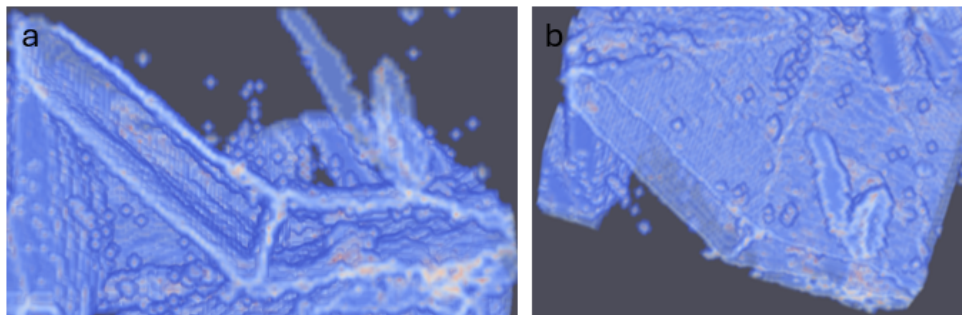


Figure 51: (a) A front view of the boundary cells of α'_{BF^2} and (b) a top view of the boundary cell within α'_{BF^2}

5 Conclusion

Through the experimental observations of the 25Ni alloy within this master thesis, the following can be concluded regarding the morphology of α'_{BF} :

- $\{3\ 10\ 15\}_{\gamma}$, $\{5\ 5\ 7\}_{\gamma}$ and $\{2\ 2\ 5\}_{\gamma}$ habit planes were found near parallel (within 3°) to the $\gamma/\alpha'_{\text{BF}}$ interfaces, corresponding to the characteristic habit planes of lenticular, lath and α'_{BF} , respectively.
- During habit plane trace analysis, if two traces are near parallel, their planes are assumed to also be near parallel. This was found to not be necessarily true as plane traces that deviated by only 2° could have planes that are angle at $20,5^{\circ}$, which is not considered to be near parallel.
- The junction plane separating the two butterfly wings do not per definition have to be one continuous plane, the main wings and the tails can have their own individual junction planes which are located at an offset, yet parallel to each other.
- The junction plane is perfectly straight and planar.
- The tail of the α'_{BF} does not need to disappear at it approaches the tip of the grain as previously shown by Umemoto et al. [10] and Gong et al. [6]. The tail can span the entire length of the α'_{BF} grain.
- Both the inner and outer interfaces of, what are called type A or tailless α'_{BF} in literature, are indeed straight and planar as mentioned by Umemoto et al. [10] and Gong et al. [6].
- The two observed α'_{BF} grains contained wing angles of 125° and 140° . This is consistent with literature.

Multiple conclusions can also be drawn regarding the formation mechanisms of α'_{BF} :

- α'_{BF} is observed to be a relatively stable phase within this specific alloy at RT as it forms as it forms prior to other α' morphologies at relatively low cooling rates.
- Austenising the alloy up to 6 hours (resulting in PAGS of $107 \pm 5\ \mu\text{m}$) result in a microstructure that is a mix of only γ and α'_{BF} upon cooling toward RT at a cooling rate of 2 K/s, higher austenisation durations result in the formation of lath α' .
- α'_{BF} was found to have a preferred to formation zone away from the γ grain boundary near the centre of the γ grain.
- When α'_{BF} does form near the γ grain boundary, one wing aligns itself with this boundary whilst the other wing grows into the γ . This is consistent with findings by Hayashi et al. [8]
- Catalytic formation of α'_{BF} is often observed.
- The α'_{BF} both contain slightly different crystal directions.
- The outer γ/α' interface exhibit a predominant G-T OR transitioning towards a combination of both N-W and G-T OR at the inner interface.
- Deformation in the surrounding γ is largest near the inner γ/α' interface, suggesting that the α'_{BF} grows first unidirectional upward upon width growth before growing below the transformation twins. This agrees with the growth mechanism proposed by Gong et al. [6]
- Strain induced α'_{BF} and lenticular α' can be formed upon mechanical polishing at RT.
- One nucleation point can result in the formation of multiple α'_{BF} grain in multiple directions.

6 Recommendations

To gain a better overview and insight on the three dimensional morphology and substructure of α'_{BF} the following recommendations are proposed:

First, to accurately measure the habit planes of α'_{BF} , techniques such as Transmission Kikuchi Diffraction (TKD) or Dark Field X-ray Microscopy should be considered. These techniques are less time consuming and energy demanding compared to 3D-EBSD using FIB milling. By employing these novel characterisation methods, all five degrees of freedom needed to measure the habit planes of α'_{BF} could be obtained. Furthermore, future research should investigate the accuracy of trace analysis as a method for determining the habit planes.

Additionally, more research is required to increase our knowledge about the nucleation and growth of α'_{BF} . In-situ observation of strain-induced α'_{BF} , for instance, would allow real-time observation of the growth mechanics of the α'_{BF} grains. Moreover, more research is required on the α'_{BF} nucleation points and how α'_{BF} originate from this point, as this could offer insight in the formation of the characteristic "V" shape of the α'_{BF} grains. Also, the formation of α'_{BF} near γ grain boundaries requires further investigation. Doing so could allow insight on why these grains are so small and formed at such a high local density compared to α'_{BF} formed in the bulk of the γ grains. It is also still unknown how ORs between α'_{BF} and the parent γ evolve upon growth and what determines the initial OR that form upon α'_{BF} nucleation, more investigation into this topic is thus still needed.

Furthermore, obtaining a three-dimensional reconstruction of a complete α'_{BF} grains is still required. This could offer more insight in the evolution of the characteristic α'_{BF} tails along the longitudinal direction as well as the evolution of all of its various substructures.

These various substructures, namely the twinning and dislocation structures within the α'_{BF} grain, require further investigation. A more thorough examination of these substructures could help explain how the growth and transformation mechanisms affect the morphology of α'_{BF} .

Lastly, the effects of mechanical polishing on the formation of α'_{BF} should be further analysed, as few is known about the effect of surface strain on the formation of this type of strain-induced α'_{BF} .

By addressing these knowledge gaps, the understanding of α'_{BF} could be greatly improved and could provide important insights into its nucleation, growth and sub-structures. This could open the door for the development of novel steels that make use of the unique morphology of α'_{BF} .

References

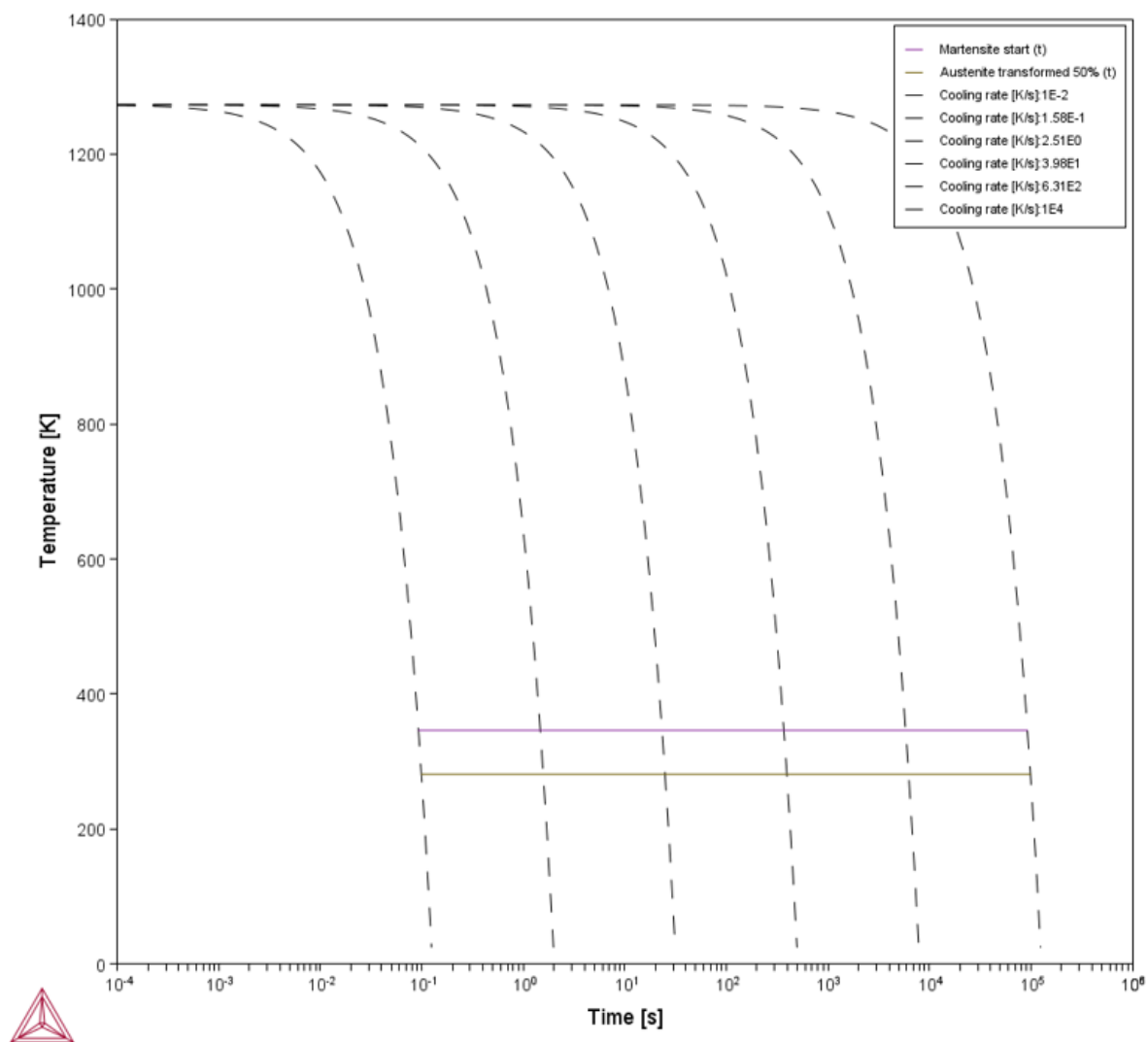
- [1] Hisashi Sato and Stefan Zaeferrer. A study on the formation mechanisms of butterfly-type martensite in fe-30 *Acta Materialia*, 57(6):1931–1937, 2009.
- [2] R.W.K. Honeycombe H.K.D.H. Bhadeshia. *Steels, microstructure and properties*. Elsevier, 3 edition, 2006.
- [3] C. Cayron. One-step theory of fcc-bcc martensitic transformation. 2012.
- [4] J.A. Klostermann. The concept of the habit plane and the phenomenological theories of the martensite transformation. *Journal of the Less Common Metals*, 28(1):75–94, 1972.
- [5] Minoru Umemoto and Eizoh Yoshitake. The morphology of martensite in fe-c, fe-ni-c and fe-cr-c alloys. *Journal of Materials Science*, 18(10):2893–2904, 1983.
- [6] H. Gong and N.J. Gu. The compound formation mechanism of butterfly martensite. *Metallography*, 21(1):1–10, 1988.
- [7] Minoru Umemoto, Tomoaki Hyodo, Tatsuo Maeda, and Imao Tamura. Electron microscopy studies of butterfly martensite. *Acta Metallurgica*, 32(8):1191–1203, 1984.
- [8] Taisuke Hayashi, Shigekazu Morito, and Takuya Ohba. Lath and butterfly composite martensite microstructure of a medium-carbon steel and its quantitative evaluation. *ISIJ International*, 58(8):1524–1531, 2018.
- [9] Wei Liuying Ke Jun Chen Qizhi, Wu Xingfang. Catalytical kinetics of butterfly martensite. *Science in China Series A: Mathematics*, 40:1185–1193, 1997.
- [10] TM. Umemoto and I. Tamura. Butterfly martensite in fe-ni-c alloys. *PROCEEDINGS OF THE INTERNATIONAL CONFERENCE ON MARTENSITIC TRANSFORMATIONS ICOMAT*, pages 53–56, 1979.
- [11] Jilt Sietsma and Kees Kwakernaak. Determination of microstructures ms43801, introduction, 2021.
- [12] Brent L. Adams David P. Field Adam J. Schwartz, Mukul Kumar. *Electron Backscatter Diffraction in Materials Science*. Springer, 2 edition, 2009.
- [13] Jilt Sietsma and Kees Kwakernaak. Determination of microstructures ms43801, textures, 2021.
- [14] Marcelo de Assumpção Pereira-da-Silva and Fabio A. Ferri. 1 - scanning electron microscopy. In Alessandra L. Da Róz, Marystela Ferreira, Fabio de Lima Leite, and Osvaldo N. Oliveira, editors, *Nanocharacterization Techniques*, Micro and Nano Technologies, pages 1–35. William Andrew Publishing, 2017.
- [15] Satyam Suwas and Ranjit Kumar Ray. *Crystallographic texture of materials*. Springer, 2014.
- [16] S. M. C. van Bohemen and J. Sietsma. Effect of composition on kinetics of athermal martensite formation in plain carbon steels. *Materials Science and Technology*, 25(8):1009–1012, 2009.
- [17] David Mercier, Claudio Zambaldi, and Thomas Bieler. Stabix toolbox documentation. 09 2015.
- [18] Gong Hai. Butterfly martensite in industrial steels. *Metallography*, 20(3):263–275, 1987.
- [19] Z. Nishiyama. *Martensitic Transformation*. Elsevier Science, 2012.
- [20] A.L. Roitburd and G.V. Kurdjumov. The nature of martensitic transformations. *Materials Science and Engineering*, 39(2):141–167, 1979.
- [21] J. W. Christian. *The theory of transformations in metals and alloys*. Pergamon, 3 edition, 2002.
- [22] G.V. Kurdjumov. Martensite crystal lattice, mechanism of austenite-martensite transformation and behavior of carbon atoms in martensite. *Metallurgical Transactions*, 7A:999–1011, 1976.
- [23] J.D. Verhoeven. *Fundamentals of physical metallurgy*. John Wiley Sons, 1975.

- [24] C. M. Wayman J. S. Bowles. The bain strain, lattice correspondences, and deformations related to martensitic transformations. *Metallurgical Transactions*, 3:1113–1121, 1972.
- [25] C. M. Wayman. The phenomenological theory of martensite crystallography: Interrelationships. *Metallurgical and materials Transactions*, 25:1787–1795, 1994.
- [26] M. A. Jaswon and J. A. Wheeler. Atomic displacements in the austenite–martensite transformation. *Acta Crystallographica*, 1(4):216–224, Sep 1948.
- [27] J.S Bowles and J.K Mackenzie. The crystallography of martensite transformations i. *Acta Metallurgica*, 2(1):129–137, 1954.
- [28] Luděk Heller and Petr Šittner. On the habit planes between elastically distorted austenite and martensite in niti. *Acta Materialia*, 269:119828, 2024.
- [29] Yuhki Tsukada, Yasuhiro Kojima, Toshiyuki Koyama, and Yoshinori Murata. Phase-field simulation of habit plane formation during martensitic transformation in low-carbon steels. *ISIJ International*, 55(11):2455–2462, 2015.
- [30] TM. Umemoto and I. Tamura. The morphology and substructure of butterfly martensite in ferrous alloys. *J. Phys. Colloques*, 43(C4):523–528, 1982.
- [31] H. Gungunes, E. Yasar, and T. N. Durlu. The effect of austenitizing time on martensite morphologies and magnetic properties of martensite in fe–24.5 *Journal of Materials Science*, 42:6102–6107, 2007.
- [32] J. Kundin, D. Raabe, and H. Emmerich. A phase-field model for incoherent martensitic transformations including plastic accommodation processes in the austenite. *Journal of the Mechanics and Physics of Solids*, 59(10):2082–2102, 2011.
- [33] Takayoshi Niho, Shoichi Nambu, Keisuke Nagato, and Masayuki Nakao. Classification of twin arrangements in butterfly martensite grains and analysis of relationship between twin arrangement and butterfly wing angle in medium-carbon steel. *ISIJ International*, 60(9):2075–2082, 2020.
- [34] Tadashi Maki, Sadamasa Shimooka, Minoru Umemoto, and Imao Tamura. The morphology of strain-induced martensite and thermally transformed martensite in fendash;nindash;c alloys. *Transactions of the Japan Institute of Metals*, 13(6):400–407, 1972.
- [35] S.M.C. Van Bohemen and J. Sietsma. Martensite formation in partially and fully austenitic plain carbon steels. *Metallurgical and Materials Transactions A*, 40:1059–1068, 2009.
- [36] Kim Verbeken, Liesbeth Barbé, and Dierk Raabe. Evaluation of the crystallographic orientation relationships between fcc and bcc phases in trip steels. *ISIJ international*, 49(10):1601–1609, 2009.
- [37] Tian-Wei Liu and Xiao-Lei Wu. Martensitic transformation pathways and crystallographic orientation relationships in steel. *Journal of Materials Science Technology*, 174:74–84, 2024.
- [38] A. Troiano A. Greninger. The mechanism of martensite formation. *JOM*, 1:590–598, 1949.
- [39] W. Pitsch. The martensite transformation in thin foils of iron-nitrogen alloys. *The Philosophical Magazine: A Journal of Theoretical Experimental and Applied Physics*, 4(41):577–584, 1959.
- [40] Hisashi Sato, Stefan Zaefferer, and Yoshimi Watanabe. μ -in-situ μ observation of butterfly-type martensite in fendash;30mass *ISIJ International*, 49(11):1784–1791, 2009.
- [41] Shibata A. Terada D. Jafarian H. R., Borhani E. and N. Tsuji. Martensite/austenite interfaces in ultrafine grained fe–ni–c alloy. *Journal of Materials Science*, 46(12):4216–4220, 2011.
- [42] T. N. Durlu. Effects of high austenitizing temperature and austenite deformation on formation of martensite in fe–ni–c alloys. *Journal of Materials Science*, 36:5665–5671, 2001.
- [43] M. Suezawa and H.E. Cook. On the nucleation of martensite. *Acta Metallurgica*, 28(4):423–432, 1980.
- [44] S. Chatterjee, H.-S. Wang, J. R. Yang, and H. K. D. H. Bhadeshia. Mechanical stabilisation of austenite. *Materials Science and Technology*, 22(6):641–644, 2006.

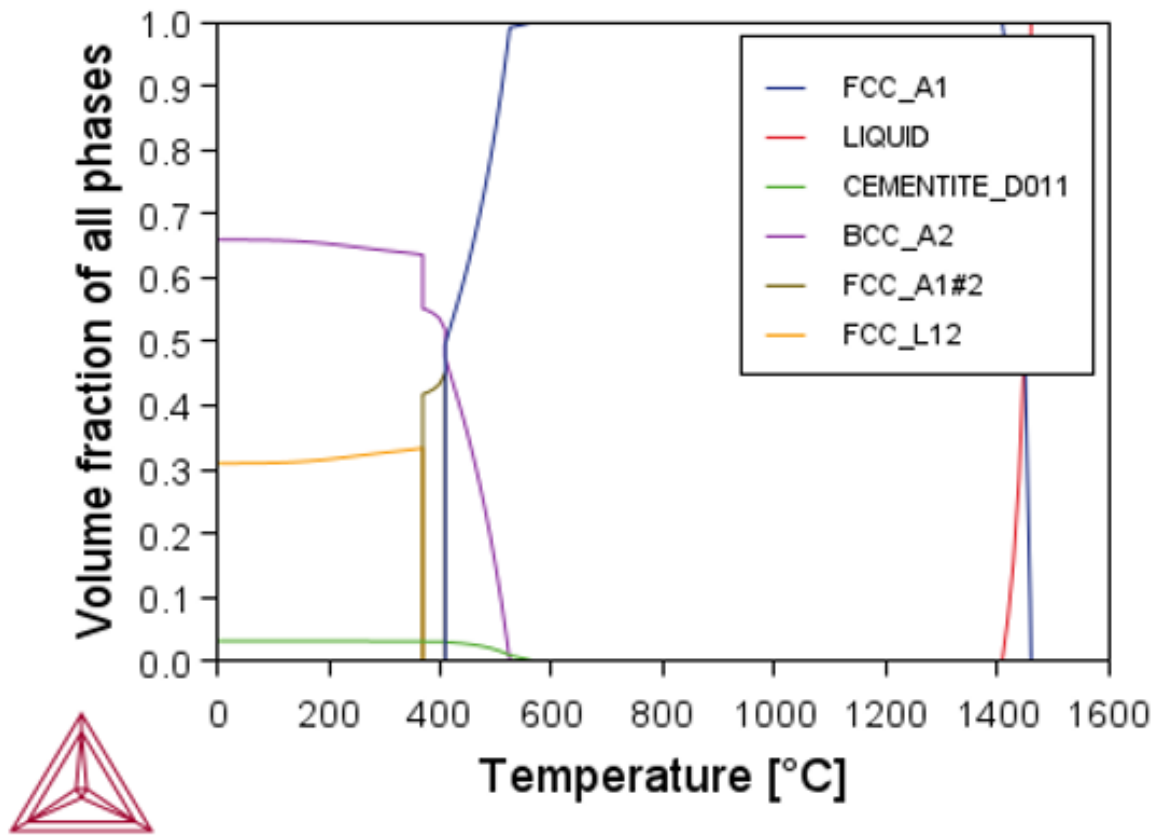
- [45] S. Chatterjee and H. K. D. H. Bhadeshia. Transformation induced plasticity assisted steels: Stress or strain affected martensitic transformation? *Materials Science and Technology*, 23(9):1101–1104, 2007.
- [46] S. Kajiwara. Roles of dislocations and grain boundaries in martensite nucleation. *Metallurgical Transactions A*, 17(10):1693–1702, Oct 1986.
- [47] Qizhi Chen. A growth manner of butterfly martensite. *Science in China Series E: Technological Sciences*, 40(6):631–636, 1997.
- [48] Earle O Snell, John C Shyne, and Alfred Goldberg. Stress-assisted and strain-induced martensite morphologies in an fe-21ni-0.6c alloy. *Metallography*, 10(3):299–314, 1977.
- [49] J Kounický. Morphology and crystallography of martensite in fe-23 *Czechoslovak Journal of Physics B*, pages 528–541, 1973.
- [50] T.N. Durlu. The effect of plastic deformation upon martensite burst transformation in fe-24 *Scripta Metallurgica*, 12(10):865–868, 1978.
- [51] T.Nuri Durlu. The effect of deformation on strain-induced martensite formation in an fe-32.4 *Scripta Metallurgica et Materialia*, 25(12):2839–2841, 1991.
- [52] N.Navruz and T.N.Durlu. Influence of austenite grain size on strain-induced martensite formation in fe-17.1 *Journal of Materials Science Letters*, 12(12):1378–1379, 1993.
- [53] T. N. Durlu. New observations on the formation of strain-induced martensite in an fe-29.6 *Journal of Materials Science*, 31:2585–2589, 1997.
- [54] X.M. Zhang, E. Gautier, and A. Simon. Orientation relationships of deformation-induced martensite in fenic alloys. *Acta Metallurgica*, 37(2):487–497, 1989.
- [55] H.J. Breukelman, M.J. Santofimia, and J. Hidalgo. Hierarchically patterned multiphase steels created by localised laser treatments. *Materials Design*, 221:110984, 2022.
- [56] H.J. Breukelman, M.J.M. Hermans, M.J. Santofimia, and J. Hidalgo. Engineering austenite/martensite mesostructured materials by controlled localised laser treatments in a fe–ni–c alloy. *Materials Design*, 227:111772, 2023.
- [57] Jaromír Kopeček, Jakub Staněk, Stanislav Habr, Filip Seitl, Lukas Petrich, Volker Schmidt, and Viktor Beneš. Analysis of polycrystalline microstructure of almgsc alloy observed by 3d ebsd. *Image Analysis and Stereology*, 39(1):1–11, Apr. 2020.
- [58] Peter Hidnert. Thermal expansion of some nickel alloys. *Journal of research of the National Bureau of Standards*, 58:89, 1957.
- [59] Carola Celada-Casero, Jilt Sietsma, and Maria Jesus Santofimia. The role of the austenite grain size in the martensitic transformation in low carbon steels. *Materials Design*, 167:107625, 2019.
- [60] P. J. Brofman and G. S. Ansell. On the effect of fine grain size on the ms temperature in fe-27ni-0.025c alloys. *Metallurgical Transactions A*, 14(9):1929–1931, Sep 1983.
- [61] Qiuliang Huang, Bruno C. De Cooman, Horst Biermann, and Javad Mola. Influence of martensite fraction on the stabilization of austenite in austenitic–martensitic stainless steels. *Metallurgical and Materials Transactions A*, 47(5):1947–1959, May 2016.
- [62] Fei Huyan, Peter Hedström, Lars Höglund, and Annika Borgenstam. A thermodynamic-based model to predict the fraction of martensite in steels. *Metallurgical and Materials Transactions A*, 47(9):4404–4410, Sep 2016.
- [63] F. Huyan, P. Hedström, and A. Borgenstam. Modelling of the fraction of martensite in low-alloy steels. *Materials Today: Proceedings*, 2:S561–S564, 2015. International Conference on Martensitic Transformations, ICOMAT-2014.
- [64] R. E. Marburger D. P. Koistinen. A general equation prescribing the extent of the austenite-martensite transformation in pure iron-carbon alloys and plain carbon steels. *Acta Metallurgica*, vol. 7(no. 1):pp. 59–60, Jan. 1959.

- [65] Junhak Pak, Dong Woo Suh, and H. K. D. H. Bhadeshia. Displacive phase transformation and surface effects associated with confocal laser scanning microscopy. *Metallurgical and Materials Transactions A*, 43:4520–4524, 2012.
- [66] T. Maki. *Morphology and substructure of martensite in steels*, volume 2 of *Woodhead Publishing Series in Metals and Surface Engineering*. Woodhead Publishing, 2012.
- [67] Tadashi Maki. Microstructure and mechanical behaviour of ferrous martensite. In *Martensitic Transformations*, volume 56 of *Materials Science Forum*, pages 157–168. Trans Tech Publications Ltd, 1 1990.
- [68] S. M. C. van Bohemen and J. Sietsma. Kinetics of martensite formation in plain carbon steels: Critical assessment of possible influence of austenite grain boundaries and autocatalysis. *Materials Science and Technology*, 30(9):1024–1033, 2014.
- [69] P. C. Maxwell, A. Goldberg, and J. C. , Shyne. Stress-assisted and strain-induced martensites in fe-ni-c alloys. *Metallurgical transactions*, 5:1305–1318, 1973.
- [70] G.B. Olson and Morris Cohen. A mechanism for the strain-induced nucleation of martensitic transformations. *Journal of the Less Common Metals*, 28(1):107–118, 1972.
- [71] Q.P. Meng, Yong Hua Rong, and T.Y. Hsu. Control of martensitic morphology in thermal-mechanical processing of ferrous alloys. In *PRICM-5*, volume 475 of *Materials Science Forum*, pages 69–72. Trans Tech Publications Ltd, 1 2005.
- [72] Do-Yeal Ryoo, Namhyun Kang, and Chung-Yun Kang. Effect of ni content on the tensile properties and strain-induced martensite transformation for 304 stainless steel. *Materials Science and Engineering: A*, 528(6):2277–2281, 2011.

A CCT diagram 25Ni



B Phase diagram 25Ni



Phase diagram corresponding to the 25Ni alloy

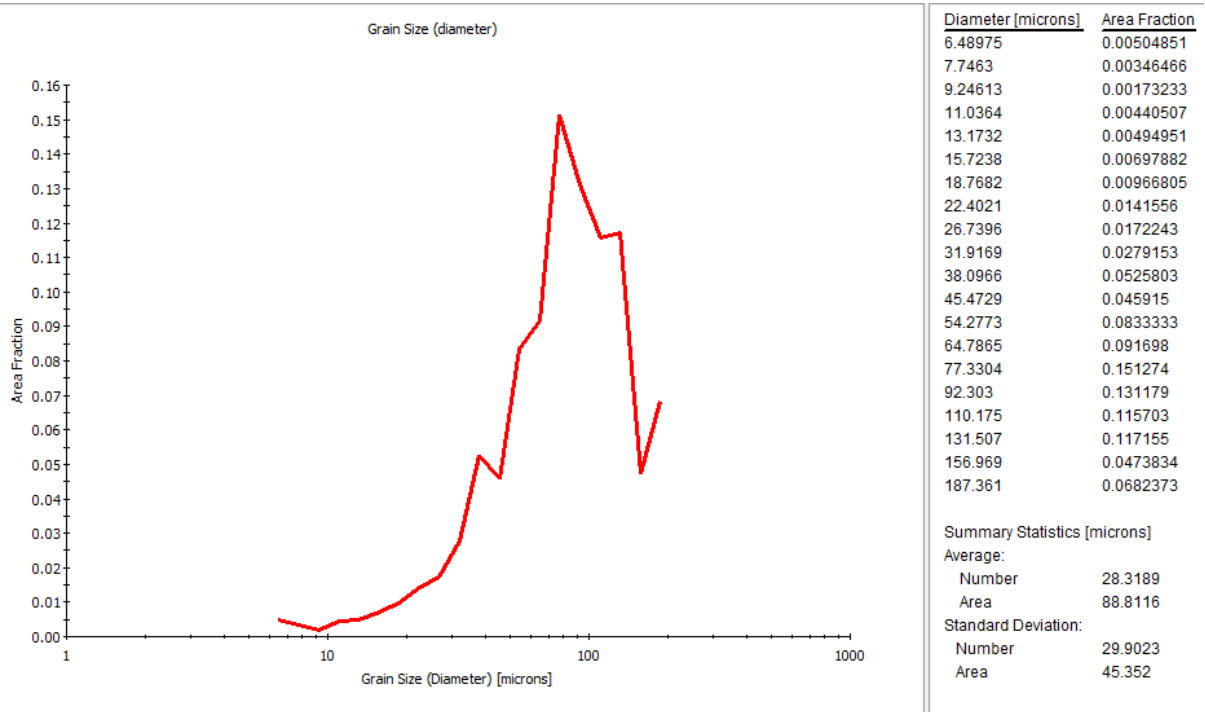
In the phase diagram above, multiple FCC phases (FCC_A1, FCC_A1#2 and FCC_L12) are shown. The differences between these FCC phases are that FCC_A1#2 is another composition set of the disordered FCC_A1 solid solution, whereas FCC_L12 is an ordered FCC structure. The Pearson notations and space groups related to these FCC phases can be observed in the table below:

Pearson notation and space groups FCC phases in 25Ni alloy obtained by ThermoCalc 2024a

Phase	Pearson symbol	Space group
FCC_A1	cF4	Fm-3m
FCC_A1#2	cF4	Fm-3m
FCC_L12	cP4	Pm-3m

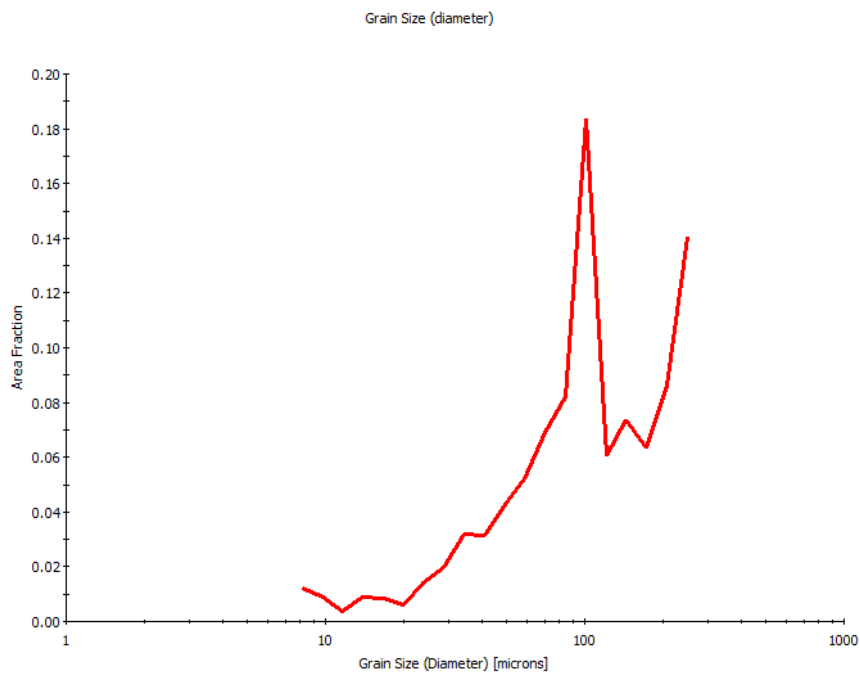
C Austenite grain sizes at various t_A

$t_A = 0h$



γ grain size 0h sample

$$t_A = 1h$$



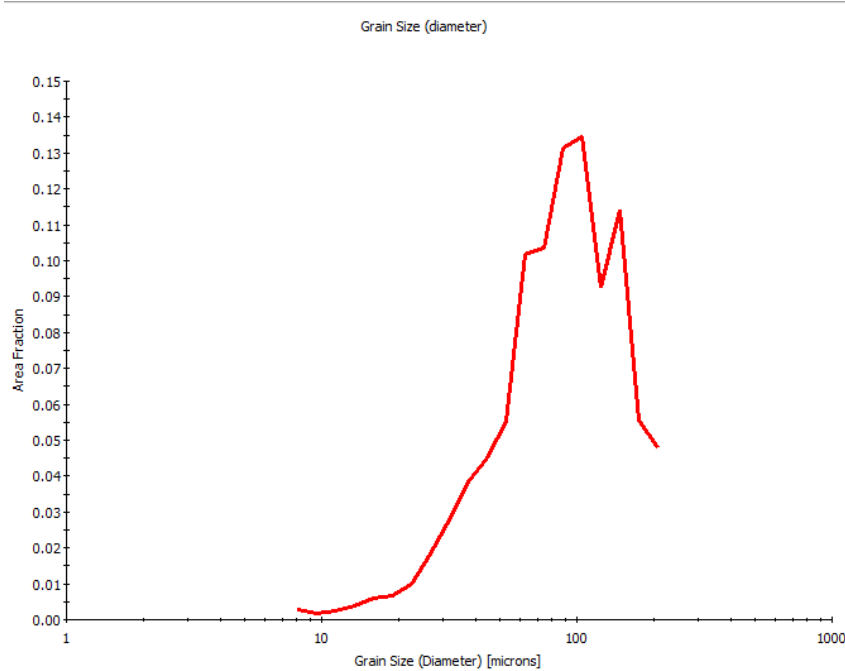
Large grains included in analysis

Diameter [microns]	Area Fraction
8.12411	0.0120773
9.72561	0.00897529
11.6428	0.00372247
13.938	0.00880984
16.6855	0.0086444
19.9747	0.00624548
23.9124	0.0139386
28.6262	0.0198739
34.2693	0.032096
41.0247	0.0313308
49.1119	0.0427464
58.7933	0.0521559
70.3832	0.0692172
84.2578	0.081977
100.868	0.1836
120.751	0.0606142
144.555	0.073891
173.051	0.0632199
207.165	0.0862992
248.003	0.140565

Summary Statistics [microns]

Average:	
Number	24.5843
Area	120.019
Standard Deviation:	
Number	31.7901
Area	72.4754

γ grain size 1h middle of the sample



Large grains included in analysis

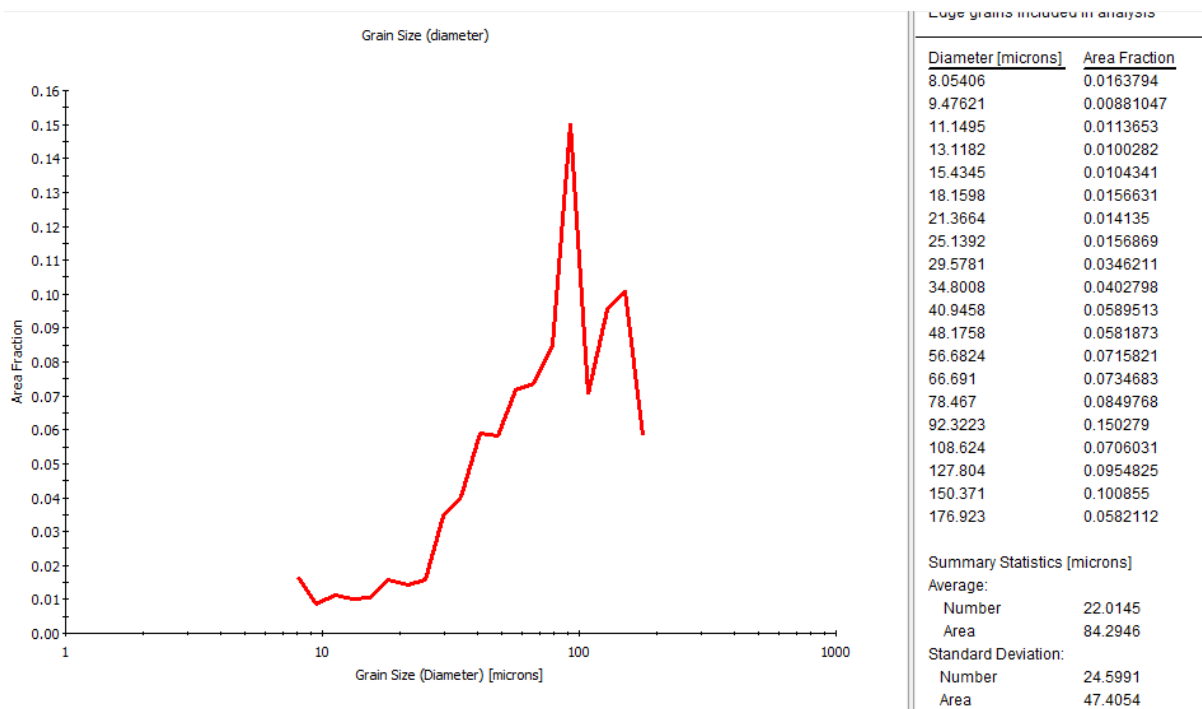
Diameter [microns]	Area Fraction
8.08619	0.00284016
9.59005	0.00184464
11.3736	0.00240096
13.4888	0.00383568
15.9975	0.00598776
18.9727	0.00677832
22.5012	0.00972096
26.6859	0.0184464
31.649	0.0276989
37.535	0.0385178
44.5157	0.0449302
52.7947	0.0551489
62.6134	0.101865
74.2582	0.103476
88.0687	0.131482
104.448	0.134571
123.873	0.0926859
146.91	0.114221
174.233	0.0557052
206.636	0.0478435

Summary Statistics [microns]

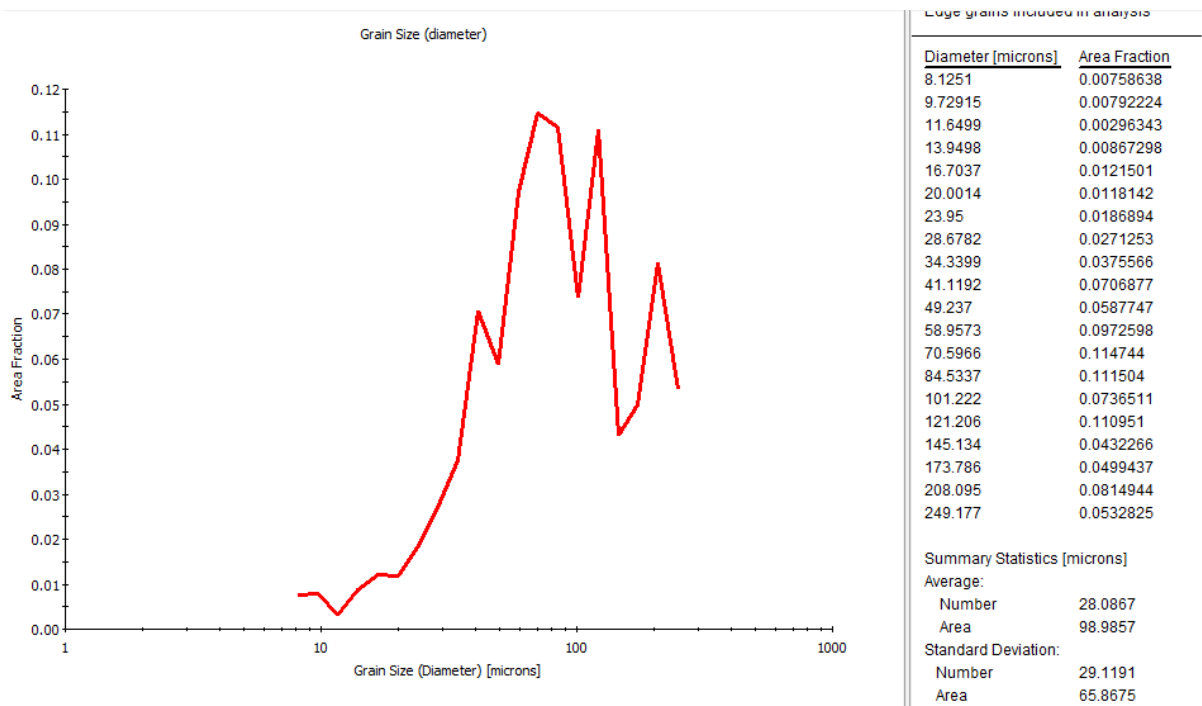
Average:	
Number	38.1212
Area	95.9725
Standard Deviation:	
Number	33.6342
Area	47.6856

γ grain size 1h edge of the sample

$$t_A = 4h$$

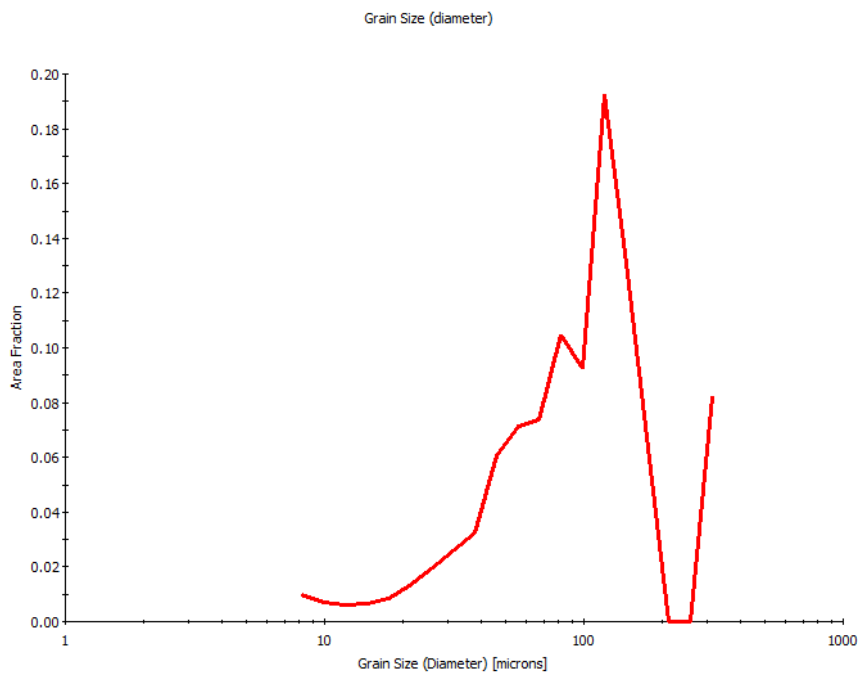


γ grain size 4h middle of the sample



γ grain size 4h edge of the sample

$$t_A = 6h$$



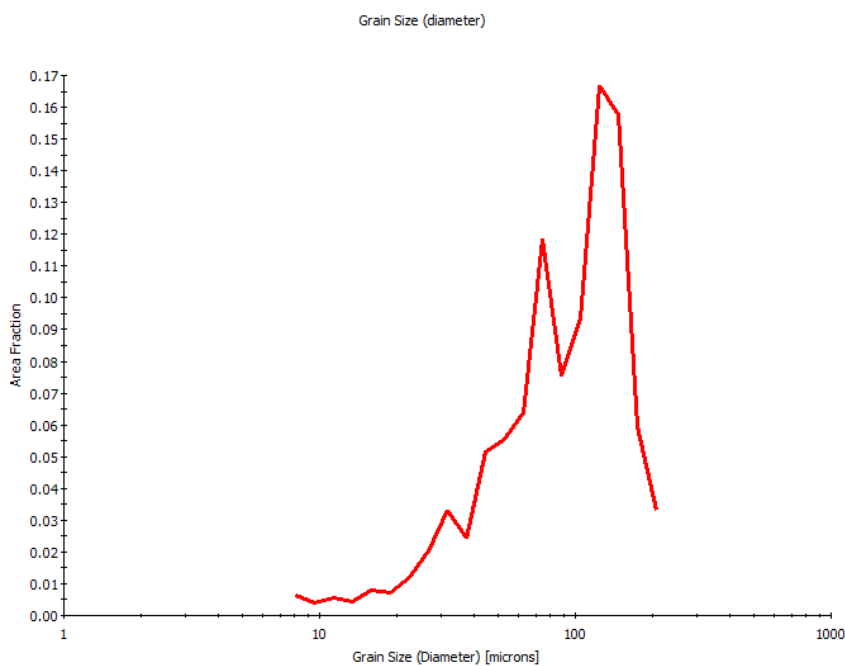
Large grains included in analysis

Diameter [microns]	Area Fraction
8.17275	0.0097835
9.90135	0.00697457
11.9956	0.0059045
14.5327	0.00670705
17.6065	0.00844591
21.3304	0.013051
25.8419	0.0193377
31.3077	0.0256435
37.9295	0.0321785
45.9519	0.0605736
55.6711	0.071389
67.4459	0.0739113
81.7112	0.104657
98.9937	0.0922936
119.932	0.192632
145.298	0.13095
176.03	0.063287
213.261	0
258.368	0
313.014	0.0822808

Summary Statistics [microns]

Average:	
Number	27.1138
Area	114.494
Standard Deviation:	
Number	31.8881
Area	81.7756

γ grain size 6h middle of the sample



Large grains included in analysis

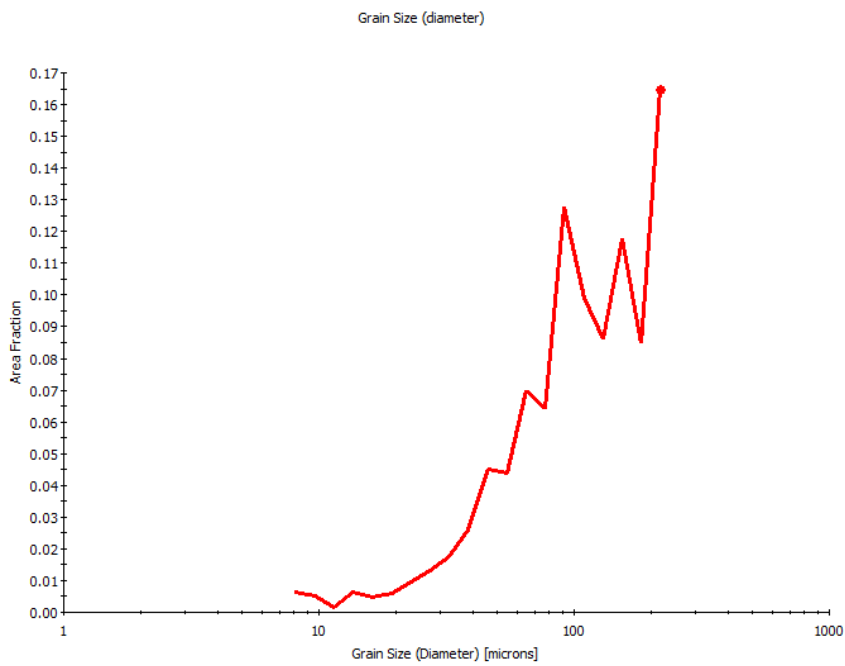
Diameter [microns]	Area Fraction
8.08766	0.00645058
9.5953	0.0040628
11.384	0.00570217
13.5061	0.00429445
16.0238	0.00810777
19.0108	0.00714553
22.5546	0.0120102
26.7591	0.0205456
31.7473	0.0330369
37.6653	0.0241451
44.6866	0.0513017
53.0167	0.055507
62.8996	0.0638465
74.6248	0.118409
88.5357	0.0753221
105.04	0.0932483
124.62	0.166682
147.851	0.157558
175.412	0.0594095
208.111	0.0332151

Summary Statistics [microns]

Average:	
Number	30.1668
Area	100.204
Standard Deviation:	
Number	32.3964
Area	50.6045

γ grain size 6h edge of the sample

$$t_A = 8h$$



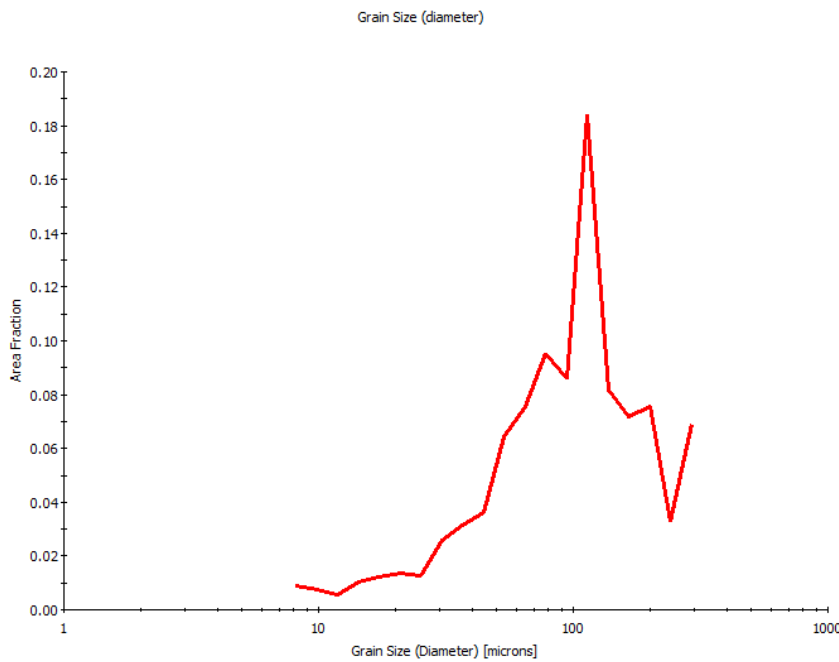
Large grains included in analysis

Diameter [microns]	Area Fraction
8.09743	0.00635571
9.63011	0.00513753
11.4529	0.0016772
13.6207	0.00654991
16.1988	0.00462554
19.2649	0.00603792
22.9114	0.00976307
27.248	0.0130292
32.4055	0.0173899
38.5392	0.0260407
45.8339	0.0452668
54.5093	0.0439073
64.8269	0.0698775
77.0973	0.0642809
91.6902	0.12775
109.045	0.0989372
129.685	0.0860845
154.232	0.117757
183.425	0.0846192
218.144	0.164913

Summary Statistics [microns]

Average:	
Number	31.6495
Area	121.255
Standard Deviation:	
Number	37.1568
Area	64.6176

γ grain size 8h middle of the sample



Large grains included in analysis

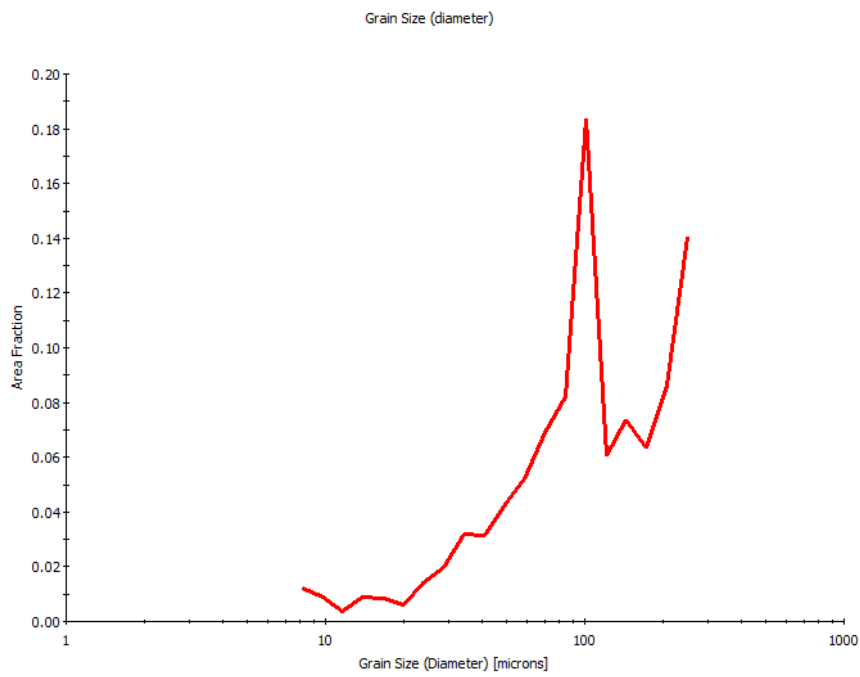
Diameter [microns]	Area Fraction
8.15711	0.00886081
9.84459	0.00766441
11.8812	0.00547725
14.3391	0.0104311
17.3055	0.0120948
20.8855	0.0135529
25.2061	0.0125435
30.4206	0.0257973
36.7138	0.0316484
44.3089	0.0363592
53.4753	0.0641193
64.5379	0.0754477
77.889	0.0952817
94.0022	0.0858227
113.449	0.183834
136.918	0.0815045
165.243	0.0719707
199.427	0.0757655
240.684	0.03277
290.475	0.0690545

Summary Statistics [microns]

Average:	
Number	26.6112
Area	116.685
Standard Deviation:	
Number	31.9341
Area	76.6195

γ grain size 8h edge of the sample

$$t_A = 10h$$



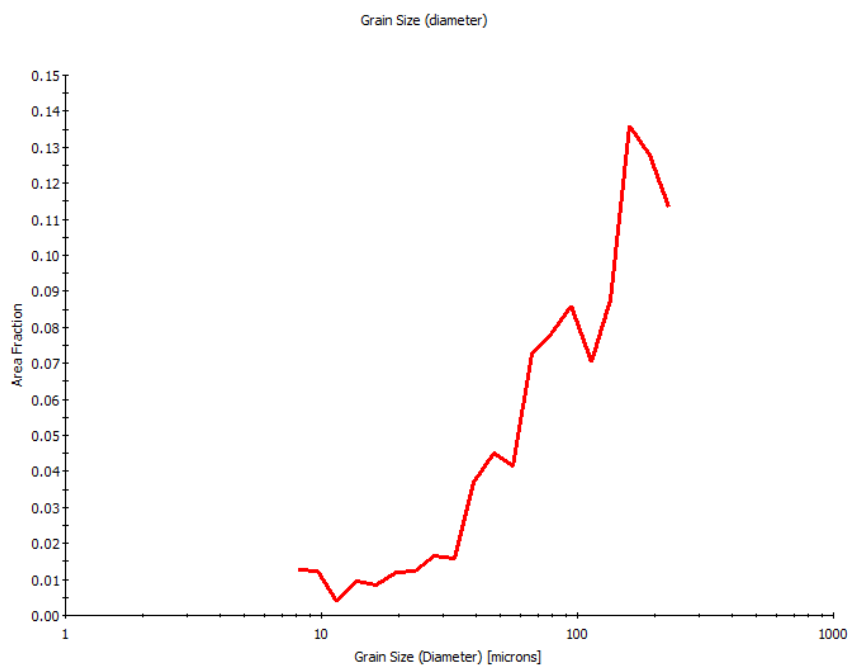
Large grains included in analysis

Diameter [microns]	Area Fraction
8.12411	0.0120773
9.72561	0.00897529
11.6428	0.00372247
13.938	0.00880984
16.6855	0.0086444
19.9747	0.00624548
23.9124	0.0139386
28.6262	0.0198739
34.2693	0.032096
41.0247	0.0313308
49.1119	0.0427464
58.7933	0.0521559
70.3832	0.0692172
84.2578	0.081977
100.868	0.1836
120.751	0.0606142
144.555	0.073891
173.051	0.0632199
207.165	0.0862992
248.003	0.140565

Summary Statistics [microns]

Average:	
Number	24.5843
Area	120.019
Standard Deviation:	
Number	31.7901
Area	72.4754

γ grain size 10h middle of the sample



Large grains included in analysis

Diameter [microns]	Area Fraction
8.10612	0.0126423
9.66116	0.0122497
11.5145	0.00392619
13.7234	0.00967805
16.356	0.00859835
19.4936	0.0118571
23.2332	0.0123675
27.6901	0.0166274
33.002	0.0158225
39.3329	0.0369847
46.8784	0.0451904
55.8712	0.0415194
66.5892	0.0726737
79.3634	0.0784649
94.588	0.0858265
112.733	0.070534
134.359	0.0876521
160.134	0.136082
190.853	0.127935
227.465	0.113369

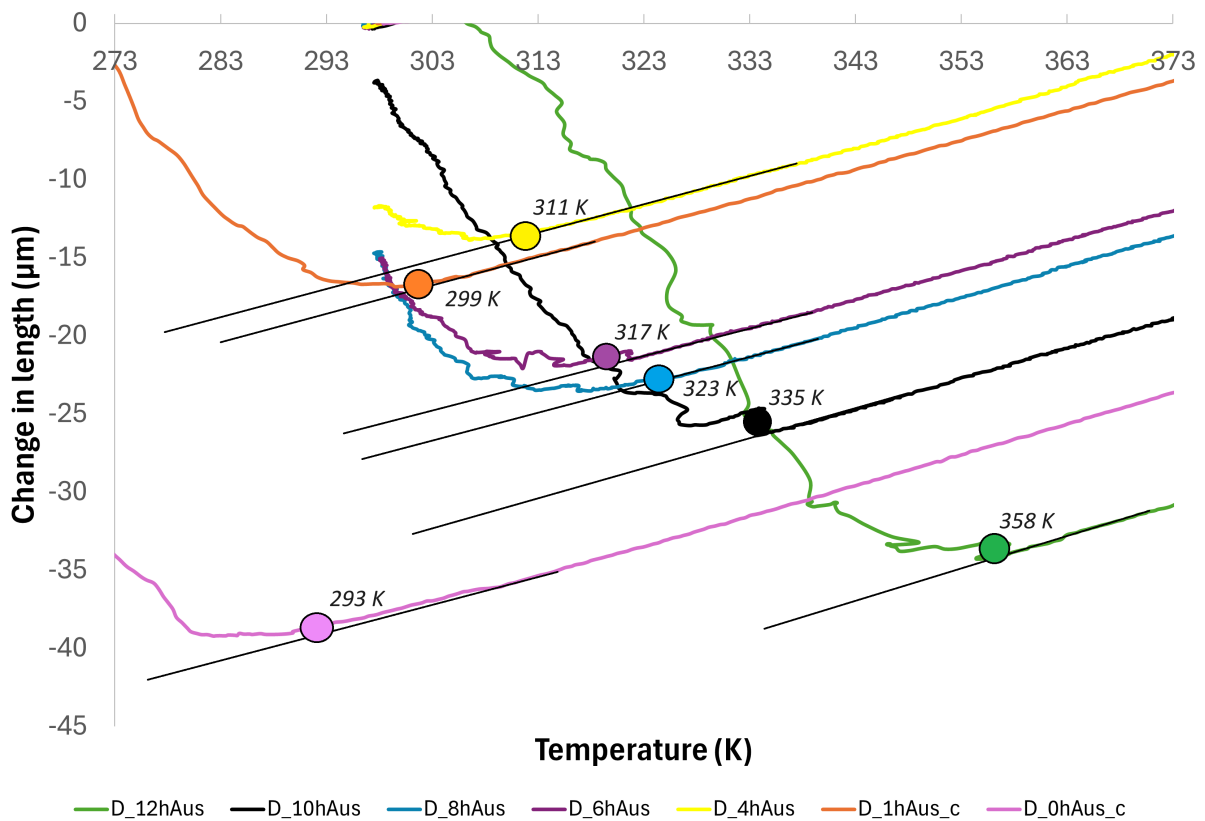
Summary Statistics [microns]

Average:	
Number	23.0143
Area	119.734
Standard Deviation:	
Number	30.6877
Area	67.4964

γ grain size 10h edge of the sample

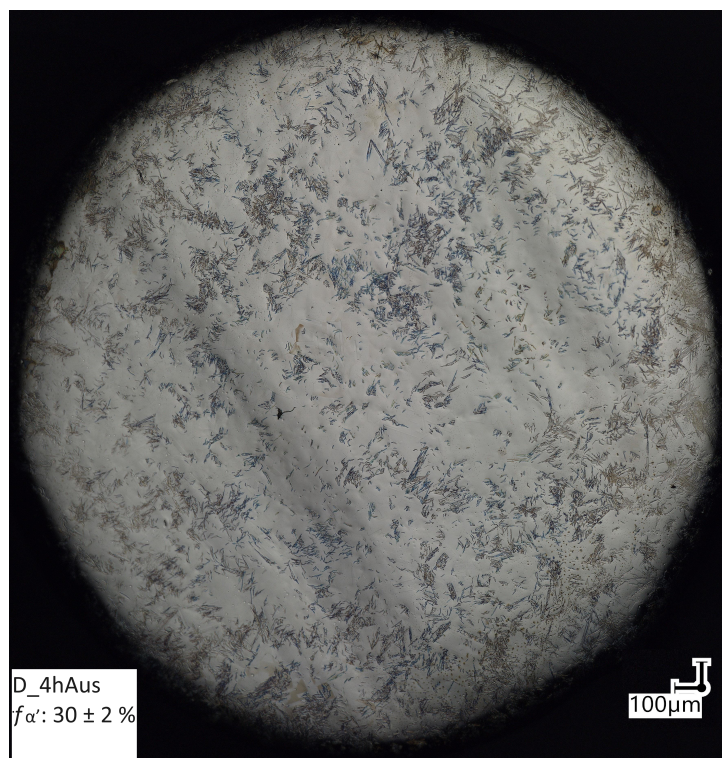
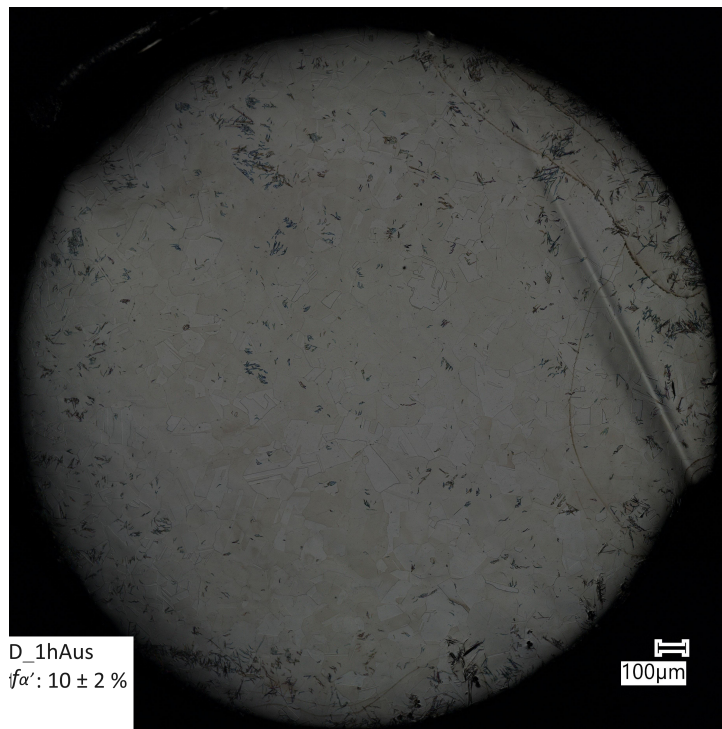
D Observing the martensite start temperature through dilatometry

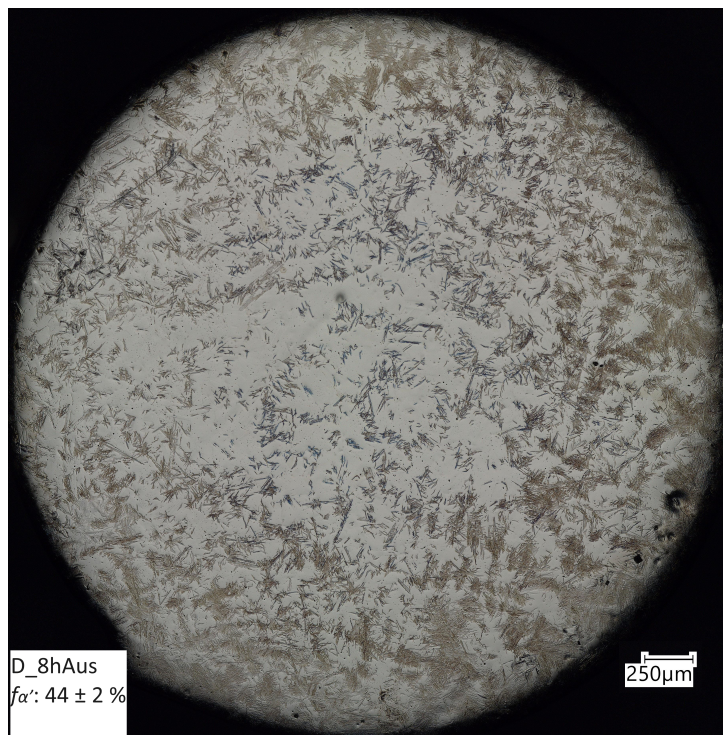
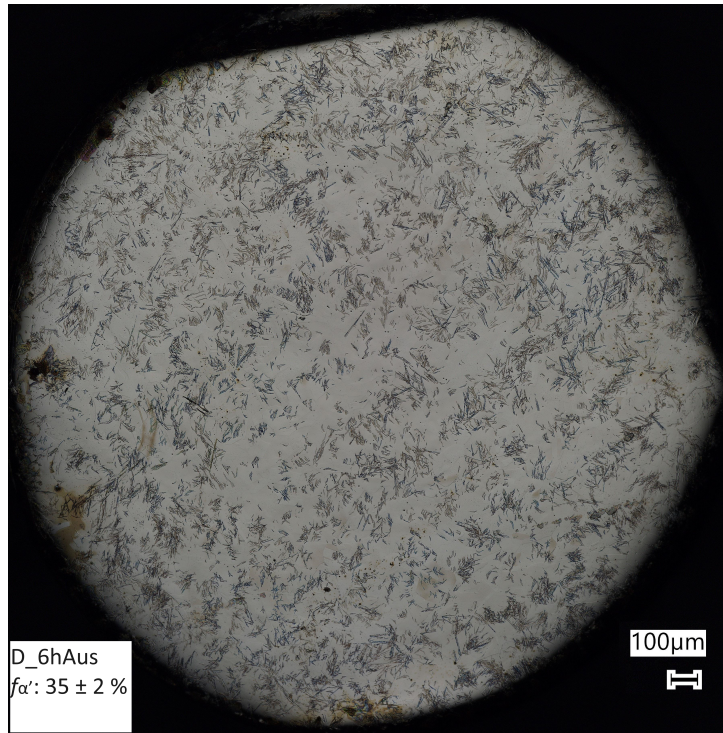
During a phase transformation, in this instance the transformation from $\gamma \rightarrow \alpha'$, the coefficient of thermal expansion (CTE) changes. Throughout the $\gamma \rightarrow \alpha'$ transformation, a increase in length is expected as a result of this change in CTE. This change in length can be measured by means of dilatometry. Upon cooling down from the austenitisation temperature, the change in length (contraction) is linear up until the initiation of the $\gamma \rightarrow \alpha'$ phase transformation after which an expansion is expected. Hence, the point at which this change in length starts changes from linear contraction to an expansion is called the M_s , as this is the point where the α' phase starts to nucleate and grow. The figure below shows the final part of the cooling curve that is obtained during dilatometry. Here the M_s temperatures corresponding to the various dilatometry samples used within this thesis can be observed.

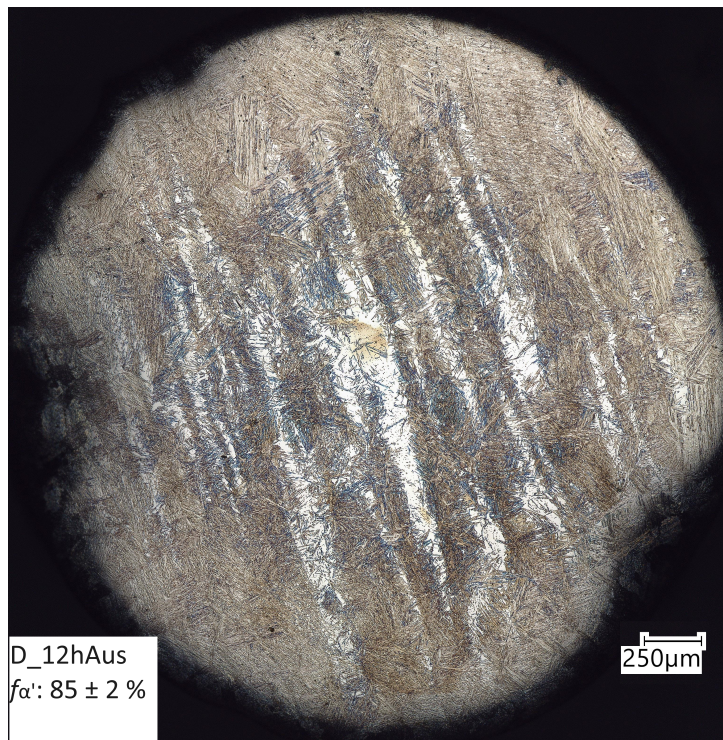
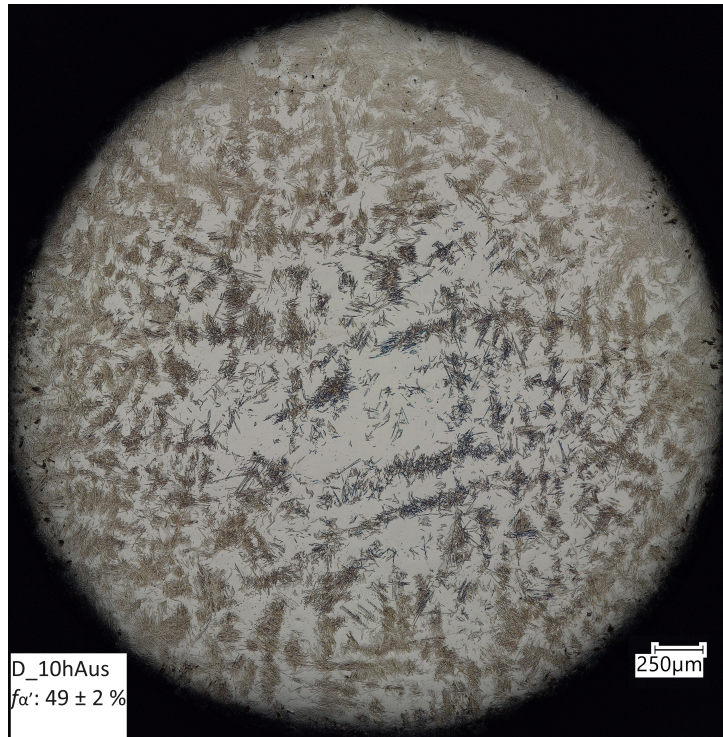


Zoomed in view of the final part of the cooling curve, obtained by dilatometry, showing the onset of the $\gamma \rightarrow \alpha'$ phase transformation

E Martensite fractions







F Python code calculating plane angles by ChatGPT

```
import numpy as np
from itertools import permutations, product

def angle_between_planes(hk11, hk12):
    """
    Compute the angle between two crystallographic planes in an FCC crystal structure.

    Parameters:
    hk11 (tuple): Miller indices (h1, k1, l1) of the first plane
    hk12 (tuple): Miller indices (h2, k2, l2) of the second plane

    Returns:
    float: Angle between the planes in degrees
    """
    h1, k1, l1 = hk11
    h2, k2, l2 = hk12

    dot_product = h1 * h2 + k1 * k2 + l1 * l2
    magnitude1 = np.sqrt(h1 ** 2 + k1 ** 2 + l1 ** 2)
    magnitude2 = np.sqrt(h2 ** 2 + k2 ** 2 + l2 ** 2)

    cos_theta = dot_product / (magnitude1 * magnitude2)
    angle = np.arccos(np.clip(cos_theta, -1.0, 1.0)) * (180.0 / np.pi)

    return angle

def generate_family_of_planes(hkl):
    """
    Generate all variants of a family of planes for given Miller indices.

    Parameters:
    hkl (tuple): Miller indices (h, k, l)

    Returns:
    list: List of all variants of the family of planes
    """
    h, k, l = hkl
    permutations_set = set(permutations([h, k, l]))
    signs = list(product([1, -1], repeat=3))

    family = set()
    for perm in permutations_set:
        for sign in signs:
            family.add(tuple(p * s for p, s in zip(perm, sign)))

    return list(family)
```

Continue on next page.

```

def angles_with_family(hkl, family_hkl):
    """
    Compute angles between a plane and all variants of a family of planes.

    Parameters:
    hkl (tuple): Miller indices of the given plane
    family_hkl (tuple): Miller indices defining the family of planes

    Returns:
    dict: Dictionary with family plane indices as keys and angles as values
    float: The minimal angle found
    list: List of planes that produce the minimal angle
    """

    family_planes = generate_family_of_planes(family_hkl)
    angles = {}
    for plane in family_planes:
        angle = angle_between_planes(hkl, plane)
        angles[plane] = angle
    min_angle = min(angles.values())
    min_angle_planes = [plane for plane, angle in angles.items() if angle == min_angle]
    return angles, min_angle, min_angle_planes

# Example usage:
hkl1 = (-5, 5, -7)
family_hkl = (1, 1, 1)

angles, min_angle, min_angle_planes = angles_with_family(hkl1, family_hkl)
print(f"Angles between plane {hkl1} and family of planes {family_hkl}:")
for plane, angle in angles.items():
    print(f"Plane {plane}: {angle:.2f} degrees")
print(f"The minimal angle is {min_angle:.2f} degrees, produced by the following planes:")
for plane in min_angle_planes:
    print(plane)

```

The python code ³ above is made with the help of ChatGPT.

³**Command to ChatGPT:** "please include in the previous code how to determine the angle between a plane and all variants of a family of planes and prints the minimal angle". The code given computed the angles between two planes hkl1 and hkl2 as follows:

```

h1, k1, l1 = hkl1
h2, k2, l2 = hkl2
dot_product = h1*h2 + k1*k2 + l1*l2
magnitude1 = np.sqrt(h1**2 + k1**2 + l1**2)
magnitude2 = np.sqrt(h2**2 + k2**2 + l2**2)
cos_theta = dot_product / (magnitude1 * magnitude2)
angle = np.arccos(cos_theta) * (180.0 / np.pi)

```

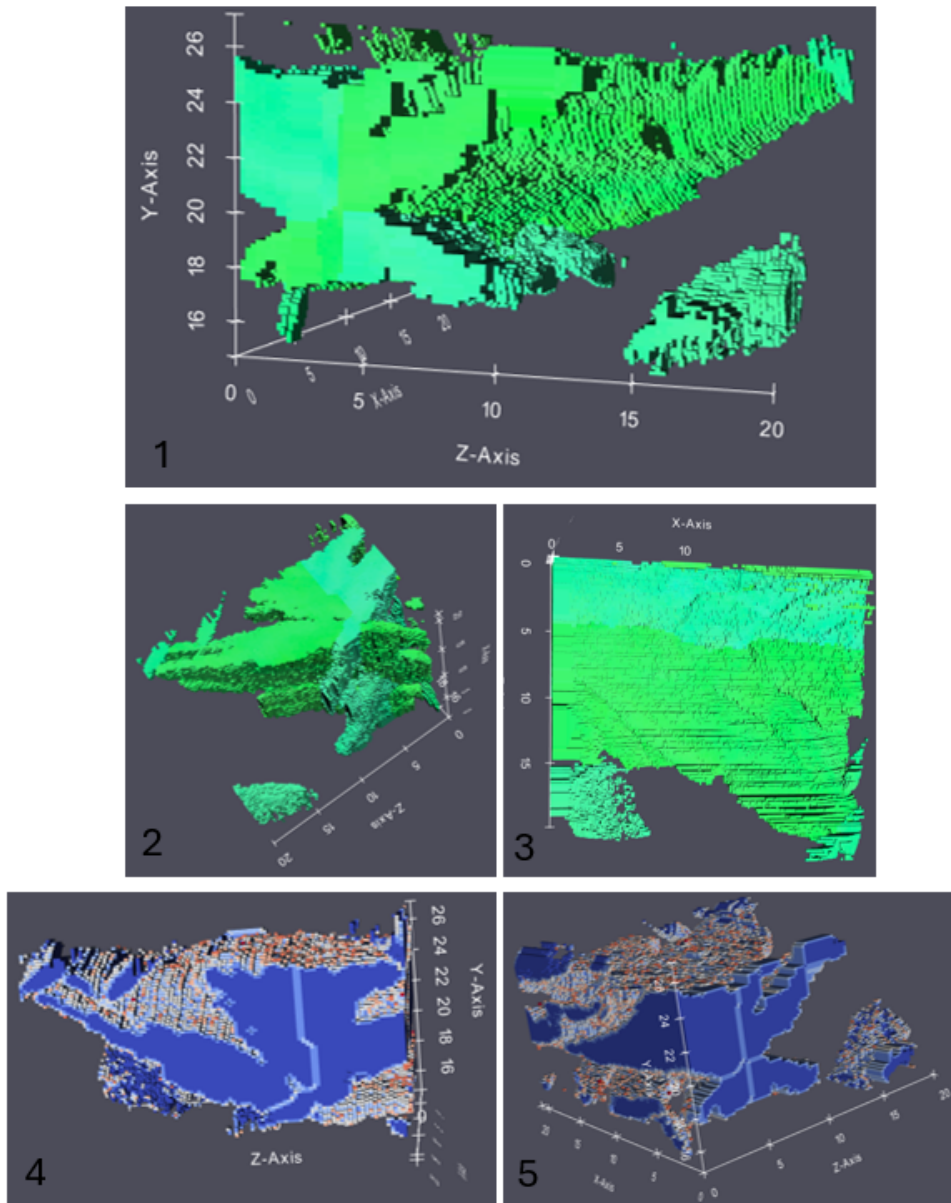
Answer ChatGPT: See Appendix F

Changed: print the planes that make the smallest angle.

Date: June 2024

G 3D butterfly grains

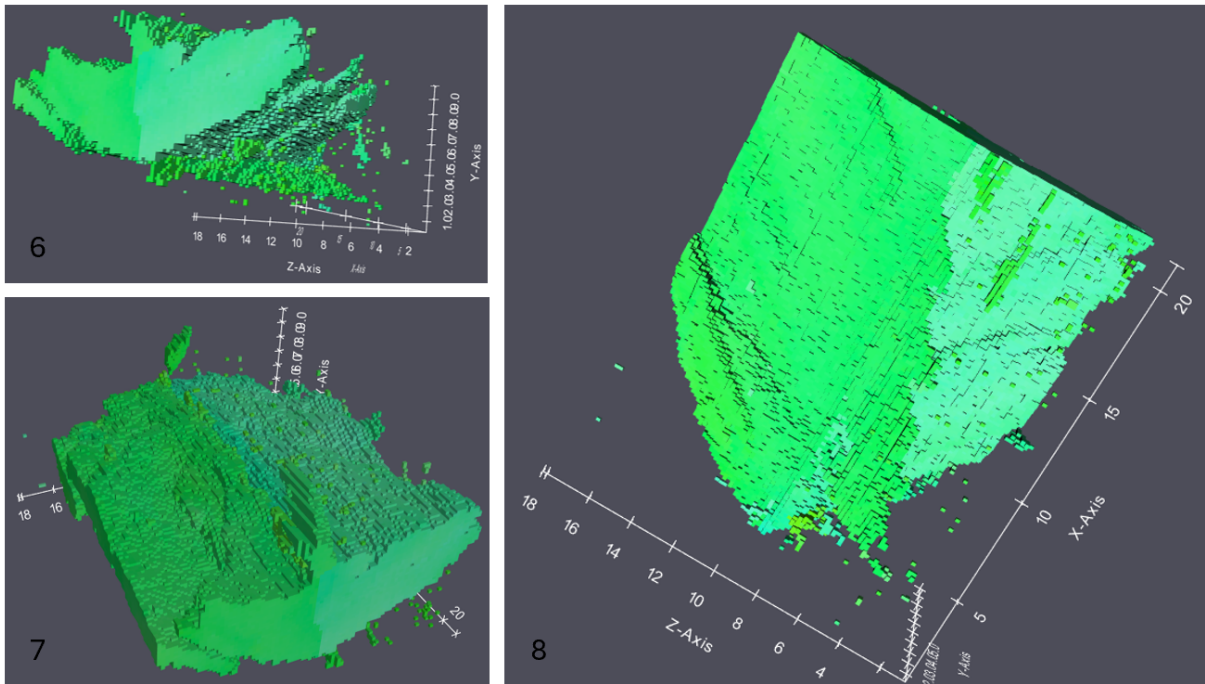
Grain α'_{BF^3}



3D reconstruction of grain α'_{BF^3}

The images above show a three-dimensional reconstruction of grain α'_{BF^3} at various angles showing both IPF (1-3) and boundary cell (4-5) views. As can be seen from the images above, the morphology of grain α'_{BF^3} is very irregular. Both the inner and outer γ/α interfaces of this grain are non-planar and contain holes, as can be clearly observed in images 1, 2, 3 and 5. Along the xy-plane, the butterfly grain has been cut off as one of the wing extends outside of the observed 3D-EBSD volume. Due to both the irregularity of one wing and the other wing only being present partially, no accurate wing measurements were possible. Due to this it was also not possible to determine the wing angle, OR and habit plane of grain α'_{BF^3} . It can however be observed in images 1, 2 and 5 that this grain contains two distinct, yet irregular, tails. Images 4 and 5 show the boundary cells at the two ends of the observed grain. In these images the junction plane, separation both wings, can clearly be observed. The junction plane is found to be irregular in image 4 and straight throughout both the wings and tails in image 5.

Grain α'_{BF^4}



3D reconstruction of grain α'_{BF^4}

Images 6-8, which can be observed above, show the three dimensional reconstruction of grain α'_{BF^4} at various angles. Upon investigation of images 6 and 7, the wings seem very short and stout with many irregularities at the γ/α interfaces. At the top of the grain, a protrusion can be observed which also belongs to the α'_{BF^4} grain, this can be either an outgrowth or a hole in the wing where α' growth was halted. Due to the irregular interfaces it was not possible to determine the OR and habit plane. The left wing is also not completely situated within the observed 3D-EBSD volume as it is cut off along the xy-plane. Hence, it is not possible to determine the wing length. Image 8 shows the bottom side of the α'_{BF^4} grain. Here, as well as in image 6, a clear single tail can be observed. This tail is irregular and seems to increase in length going in longitudinal direction of the grain towards the tip before disappearing.